

**University of Alberta**

Vapour Phase Cracking of Bitumen Derived Heavy Gas Oil

by

Weida Bu

A thesis submitted to the Faculty of Graduate Studies and Research  
in partial fulfillment of the requirements for the degree of

Master of Science in Chemical Engineering

Department of Chemical and Materials Engineering

© Weida Bu

Fall 2012

Edmonton, Alberta

Permission is hereby granted to the University of Alberta Libraries to reproduce single copies of this thesis and to lend or sell such copies for private, scholarly or scientific research purposes only. Where the thesis is converted to, or otherwise made available in digital form, the University of Alberta will advise potential users of the thesis of these terms.

The author reserves all other publication and other rights in association with the copyright in the thesis and, except as herein before provided, neither the thesis nor any substantial portion thereof may be printed or otherwise reproduced in any material form whatsoever without the author's prior written permission.

## **Abstract**

The kinetics of vapor phase cracking of bitumen derived heavy gas oil and the quality of liquid products were investigated at temperatures of 600-700 °C. Fixed and condensed gases were analyzed by gas chromatography. The quality of liquid products was characterized using simulated distillation, elemental analysis and  $^{13}\text{C}$  NMR. Consistent with gas phase cracking behavior, the coke yields were negligible, below 2 %. The yields of  $\text{C}_2\text{-C}_3$  olefins were 2 to 16 wt% compared with the yields of  $\text{C}_2\text{-C}_3$  alkanes from 0.2 to 1.0 wt%. Hydrogen content of liquid products was lost significantly, corresponding to increase of aromatic carbon content with increase of conversion. A two-step kinetic model including fast dehydrogenation and slower cracking was proposed on the basis of chemical structure change of the reactant. The activation energy of the overall cracking reaction on reactive materials was 208 kJ/mol based on full analysis of the reactor.

## **Acknowledgement**

I would like to take the chance to appreciate Dr. Gray for his responsible and meticulous supervision on my project. It is his valuable instructions and suggestions that help me to obtain important breakthroughs in the experiments. I also learned how to think and speak in a more scientific way from each discussion with him. I also want to thank Syncrude Canada and Natural Sciences and Engineering Research Council of Canada for the stable funding support. Besides, I also thank Kourosh Vafi for the systematic training on the apparatus operation and Lisa Brand for her material support on the experiments. Last but not least, I show great gratitude to my parents' concern on my life in the last two years. Their encouragement gives me strong confidence to overcome difficulties and motivation to challenge new objectives.

## Table of Contents

|   |           |
|---|-----------|
| <b>CHAPTER 1 Introduction .....</b>   | <b>1</b>  |
| <b>CHAPTER 2 Literature Review .....</b>                                    | <b>3</b>  |
| 2.1 Industrial Upgrading Processes.....                                     | 3         |
| 2.2 Novel Coking Technologies .....   | 6         |
| 2.2.1 ETX I <sup>Y</sup> Q Cross Flow Coking.....                           | 7         |
| 2.2.2 LR-Process .....  | 8         |
| 2.2.3 Ivanhoe Heavy to Liquid (HTL) Process .....                           | 8         |
| 2.2.4 ART Process.....  | 10        |
| 2.2.5 Summary .....   | 11        |
| 2.3 Improvements on Current Fluid Coking.....                               | 11        |
| 2.4 Industrial Petro-Chemical Processes.....                                | 12        |
| 2.5 Composition and Structure of Bitumen and Its Derived Heavy Gas Oil..... | 14        |
| 2.6 Mechanism for Cracking of n-alkanes.....                                | 21        |
| 2.7 Kinetics of Cracking of n-hexadecane as Model Compound.....             | 23        |
| 2.8 Mechanism of Cracking of Other Components of Gas Oil .....              | 26        |
| 2.8.1 Reactions of Olefins .....  | 26        |
| 2.8.2 Reactions of Aromatics .....  | 27        |
| 2.8.3 Reactions of Naphthenes .....   | 27        |
| 2.8.4 Reactions of Sulfur Compounds.....                                    | 28        |
| 2.9 Kinetics of Cracking of Gas Oil.....                                    | 29        |
| 2.9.1 Empirical Kinetics with No Chemical Information.....                  | 29        |
| 2.9.2 Empirical Lumped Kinetics with No Chemical Information.....           | 32        |
| 2.9.3 Structured Kinetics with Chemical Information.....                    | 34        |
| 2.10 Summary of Key Issues .....  | 37        |
| <b>CHAPTER 3 Experimental Materials and Method .....</b>                    | <b>39</b> |
| 3.1 Materials .....   | 39        |
| 3.2 Reactor Apparatus and Operation .....                                   | 41        |
| 3.2.1 Reactor Apparatus .....   | 41        |
| 3.2.1.1 Feed Introduction .....   | 42        |

|   |           |
|---|-----------|
| 3.2.1.2 Reaction Section .....                            | 43        |
| 3.2.1.3 Product Collection.....                           | 44        |
| 3.2.1.4 Data Acquisition System .....                     | 45        |
| 3.2.1.5 Helium Gas Flow Control.....                      | 45        |
| 3.2.2 Reactor Feed Optimization .....                     | 47        |
| 3.2.3 Reactor Operation.....                              | 50        |
| 3.2.3.1 Reactor Preparation .....                         | 50        |
| 3.2.3.2 Condenser Leak Test .....                         | 50        |
| 3.2.3.3 Operating Condition.....                          | 51        |
| 3.2.3.4 Operating Procedures .....                        | 52        |
| 3.3 Analysis of Reactor Samples .....                     | 55        |
| 3.3.1 Fixed and Condensed Gas Analysis .....              | 55        |
| 3.3.1.1 Gas Chromatography Apparatus.....                 | 55        |
| 3.3.1.2 Gas Chromatography Calibration.....               | 56        |
| 3.3.1.3 Gas Chromatography Analysis Procedure.....        | 57        |
| 3.3.2 Liquid Product Analysis .....                       | 57        |
| 3.3.2.1 Simulated Distillation .....                      | 57        |
| 3.3.2.1.1 Simulated Distillation Apparatus .....          | 57        |
| 3.3.2.1.2 Simulated Distillation Analysis Procedure ..... | 59        |
| 3.3.2.2 Elemental Analysis .....                          | 60        |
| 3.3.2.2.1 Elemental Analyzer .....                        | 60        |
| 3.3.2.2.2 Elemental Analysis Procedure.....               | 61        |
| 3.3.2.3 <sup>13</sup> C NMR Analysis.....                 | 62        |
| 3.3.3 Recovered Solvent Analysis .....                    | 62        |
| <b>CHAPTER 4 Results and Discussion .....</b>             | <b>64</b> |
| 4.1 Performance of the Tubular Reactor .....              | 64        |
| 4.1.1 Temperature Profile.....                            | 64        |
| 4.1.2 Reaction Residence Time .....                       | 70        |
| 4.1.3 Material Balance .....                              | 76        |
| 4.2 Conversion of Heavy Gas Oil .....                     | 79        |
| 4.3 Yield and Distribution of Cracked Products .....      | 83        |

|   |            |
|---|------------|
| 4.3.1 Coke Yield.....   | 83         |
| 4.3.2 Gas Product Yield .....   | 86         |
| 4.3.3 Yield of Olefins Versus Alkanes .....                                   | 87         |
| 4.4 Liquid Product Quality.....   | 91         |
| 4.4.1 Elemental Composition .....   | 91         |
| 4.4.2 Chemical Structure.....   | 94         |
| 4.5 Kinetics of Vapor Phase Cracking of Bitumen Derived Heavy Gas Oil .....   | 99         |
| <b>CHAPTER 5 Implications and Conclusions .....</b>                           | <b>113</b> |
| 5.1 Implications.....   | 113        |
| 5.2 Conclusions .....   | 115        |
| <b>BIBLIOGRAPHY .....</b>   | <b>117</b> |
| <b>APPENDIX A Calculation Details on Conversion of Reactive Species .....</b> | <b>123</b> |
| <b>APPENDIX B GC Calculations and Chromatographs .....</b>                    | <b>126</b> |
| 1. Non-Condensed Gas Products .....   | 126        |
| 2. Condensed Gas Products .....   | 128        |
| <b>APPENDIX C Simulated Distillation Results .....</b>                        | <b>133</b> |
| 1. ASTM D2887 Results .....   | 133        |
| 2. ASTM D6352 Results .....   | 137        |
| <b>APPENDIX D MATLAB Code for the Kinetic Model .....</b>                     | <b>141</b> |
| 1. Residence Time .....   | 141        |
| 2. Mass Flow Rate of Reactive Species .....                                   | 141        |
| 3. Kinetic Parameters .....   | 142        |
| <b>APPENDIX E Piping and Instrumentation Diagram .....</b>                    | <b>144</b> |

## List of Tables

|  |     |
|--|-----|
| Table 2-1. Comparison of feed and HTL product properties in two operation modes<br>(Freel, B. et al. 2002-2005).....     | 10  |
| Table 2-2. Product distribution from VGO and naphtha (Greene, 1969) .....  | 14  |
| Table 2-3. Comparison of light crude and bitumens (Gray, 2010).....  | 15  |
| Table 2-4. Properties of Syncrude coker gas oil produced from Athabasca bitumen<br>(Kanda et al., 2004; Yui, 1995) ..... | 15  |
| Table 2-5. Aromatic contents of different bitumens (Strausz, 2003) .....   | 17  |
| Table 2-6. Effect of feed properties on product distribution at 660 °C and 2.2 s (Meng et<br>al., 2005).....             | 31  |
| Table 2-7. Various studies on empirical kinetics of cracking of gas oils .....   | 32  |
| Table 3-1. Properties of heavy gas oil feed material .....   | 40  |
| Table 3-2. Composition of GC calibration gases .....   | 41  |
| Table 3-3. Allowable operating conditions and nozzle tip position.....   | 49  |
| Table 3-4. Operating conditions of all experiments.....  | 52  |
| Table 3-5. Oven temperature profile during analysis .....  | 56  |
| Table 3-6. Operating conditions for Bruker 450-GC and VARIAN 450-GC .....  | 58  |
| Table 4-1. Axial temperature profile of reactor under various operating conditions .....                                 | 65  |
| Table 4-2. Helium flow temperature at nozzle tip position.....   | 69  |
| Table 4-3. Flow rate distributions at reactor inlet and outlet .....   | 72  |
| Table 4-4. Comparison between actual and estimated reaction residence time in the full<br>reactor section .....          | 75  |
| Table 4-5. Comparison between actual and estimated reaction residence time in the<br>reactor heating entry section.....  | 76  |
| Table 4-6. Measured conversions at different operating conditions .....  | 81  |
| Table 4-7. Conversion of reactive species versus overall species.....  | 106 |
| Table C-1. Summary of ASTM D2887 simulated distillation results.....   | 133 |
| Table C-2. Summary of ASTM D6352 simulated distillation results.....   | 137 |

## List of Figures

|   |    |
|---|----|
| Figure 2-1. Schematic diagram of delayed coking process (Fundamental of Petroleum Refining by Fahim et al. Copyright @ 2010 Elsevier B.V. Reproduced with permission of Elsevier B.V. in the format Thesis via Copyright Clearance Center) .... | 4  |
| Figure 2-2. Schematic diagram of fluid coking process (Fundamental of Petroleum Refining by Fahim et al. Copyright @ 2010 Elsevier B.V. Reproduced with permission of Elsevier B.V. in the format Thesis via Copyright Clearance Center) ....   | 5  |
| Figure 2-3. Schematic diagram of naphtha-based steam cracking process (Fundamentals of Petroleum and Petrochemical Engineering by Chaudhuri) .....  | 13 |
| Figure 2-4. Pendant-core building block model (Wiehe et al., 1994) .....  | 18 |
| Figure 2-5. Proposed models for asphaltene structure .....  | 20 |
| Figure 2-6. Free radical chain reaction mechanism for hydrocarbons (Gray, 2010) .....   | 21 |
| Figure 2-7. Free radical chain reaction mechanism for alkyl sulfur compounds (Gray, 2010) .....   | 28 |
| Figure 3-1. Simplified diagram of reactor apparatus .....   | 42 |
| Figure 3-2. Calibration curves of mass flow controllers .....   | 46 |
| Figure 3-3. Schematic of reactor inlet .....  | 48 |
| Figure 3-4. Slug flow pattern inside of nozzle tube .....   | 49 |
| Figure 4-1. Axial temperature profiles of the flow gas stream at different operating conditions .....   | 68 |
| Figure 4-2. Mass recoveries and product yields on the basis of feed mass for all experiments .....  | 78 |
| Figure 4-3. Change of mass recovery with gas yield .....  | 79 |
| Figure 4-4. Variation of mass recovery as a function of conversion .....  | 82 |
| Figure 4-5. CG analysis of recovered methylene chloride solvent .....   | 83 |
| Figure 4-6. Coke yield versus conversion of heavy gas oil feed .....  | 84 |
| Figure 4-7. Gas yield versus conversion at different residence times and temperatures   | 86 |
| Figure 4-8. Comparison between C <sub>2</sub> -C <sub>3</sub> olefin and alkane yields at different conversions .....   | 87 |
| Figure 4-9. Olefin selectivity as a function of conversion .....  | 89 |
| Figure 4-10. Methane yield as a function of conversion .....  | 90 |

|  |     |
|--|-----|
| Figure 4-11. Relationship between carbon content (a), hydrogen content (b), sulfur and nitrogen content (c) and changing conversion for liquid product. The lines show the linear regression results for the data, except for hydrogen which shows a second order regression curve. .... | 92  |
| Figure 4-12. Aromatic carbon content of heavy liquid product fraction as a function of conversion.....   | 95  |
| Figure 4-13. Correlation between aromaticity and hydrogen content of the liquid product, only data measured directly by <sup>13</sup> C NMR and elemental analyzer are included.....   | 96  |
| Figure 4-14. Change of aromatic carbon content with conversion, only data measured directly by <sup>13</sup> C NMR are included. ....  | 97  |
| Figure 4-15. Two-step mechanism for vapor phase cracking of aromatic-naphthenic heavy gas oil.....   | 98  |
| Figure 4-16. Variation of rate constant with conversion at different temperature .....   | 102 |
| Figure 4-17. Arrhenius plot for conversion of heavy gas oil fraction (343 °C+), reaction was assumed to be isothermal at furnace set point temperatures.....   | 103 |
| Figure 4-18. Arrhenius plot for conversion of reactive species in heavy gas oil.....   | 107 |
| Figure 4-19. Mass flow rate of reactive species versus reactor position at operating condition of 600 °C and 0.682 s .....   | 109 |
| Figure 4-20. Comparison of Arrhenius plot for bitumen-derived heavy gas oil and vacuum residue fractions of bitumens .....   | 111 |
| Figure B-1. GC chromatograph for non-condensed gases.....  | 127 |
| Figure B-2. GC chromatograph for condensed gases collected in gas bag 1 at 600 Run1 .....  | 129 |
| Figure B-3. GC chromatograph for condensed gases collected in gas bag 2 at 600 Run1 .....  | 130 |
| Figure B-4. GC chromatograph for condensed gases collected in gas bag 3 at 600 Run1 .....  | 131 |
| Figure B-5. GC chromatograph for condensed gases collected in gas bag 4 at 600 Run1 .....  | 132 |
| Figure C-1. Boiling curves for bitumen derived heavy gas oil feed and liquid products at 600 °C furnace set point by ASTM D 2886 method .....  | 134 |

|  |     |
|--|-----|
| Figure C-2. Boiling curves for bitumen derived heavy gas oil feed and liquid products at<br>650 °C furnace set point by ASTM D 2886 method ..... | 135 |
| Figure C-3. Boiling curves for bitumen derived heavy gas oil feed and liquid products at<br>700 °C furnace set point by ASTM D 2886 method ..... | 136 |
| Figure C-4. Boiling curves for bitumen derived heavy gas oil feed and liquid products at<br>600 °C furnace set point by ASTM D 6352 method ..... | 138 |
| Figure C-5. Boiling curves for bitumen derived heavy gas oil feed and liquid products at<br>650 °C furnace set point by ASTM D 6352 method ..... | 139 |
| Figure C-6. Boiling curves for bitumen derived heavy gas oil feed and liquid products at<br>700 °C furnace set point by ASTM D 6352 method ..... | 140 |

## Nomenclature

|                               |  |
|-------------------------------|--|
| $q_s''$                       | Local heat flux (W/m <sup>2</sup> )  |
| $q_{conv}$                    | Total heat transfer rate (W)   |
| $h$                           | Local convection coefficient (W/m <sup>2</sup> .K)                           |
| $\bar{h}$                     | Average convection coefficient (W/m <sup>2</sup> .K)                         |
| $k$                           | Thermal conductivity (W/m.K)   |
| $T_s$                         | Tube surface temperature (K)   |
| $T_m$                         | Mean temperature of the internal flow (K)                                    |
| $T_{m,i}$                     | Inlet fluid temperature (K)  |
| $T_{m,o}$                     | Outlet fluid temperature (K)   |
| $T_0$                         | Room temperature (K)   |
| $\dot{m}$                     | Mass flow rate of the internal flow (kg/s)                                   |
| $L$                           | Total reactor tube length (m)  |
| $D$                           | Inner diameter of the tube (m)   |
| $V$                           | Volume of reactor tube (m <sup>3</sup> )                                     |
| $A_R$                         | Cross sectional area of reactor tube (m <sup>2</sup> )                       |
| $x$                           | Reactor tube position (m)  |
| $\tau$                        | Residence time (s)   |
| $v$                           | Volume flow rate of helium (m <sup>3</sup> /s)                               |
| $v_0$                         | Volume flow rate of helium at room temperature (m <sup>3</sup> /s)           |
| $X$                           | Conversion of overall heavy gas oil (343 °C+)                                |
| $X_{NA}$                      | Conversion of non-aromatics in heavy gas oil after dehydrogenation step      |
| $w$                           | Mass fraction of the sample  |
| $m$                           | Mass of the sample (kg)  |
| $W_{HGO}$                     | Mass concentration of heavy gas oil (kg/m <sup>3</sup> )                     |
| $F_{HGO}$                     | Mass concentration of heavy gas oil (kg/m <sup>3</sup> )                     |
| $F_{\text{reactive species}}$ | Mass concentration of reactive species in heavy gas oil (kg/m <sup>3</sup> ) |

|                         |  |
|-------------------------|--|
| $S$                     | Olefin selectivity   |
| $y_{\text{aromatic C}}$ | Yield ratio of aromatic carbon in liquid product over in feed                          |
| $r_{HGO}$               | Reaction rate of heavy gas oil based on mass ( $\text{kg}/\text{m}^3 \cdot \text{s}$ ) |
| $k_{HGO}$               | Reaction rate constant ( $\text{s}^{-1}$ )   |
| $Y$                     | Recovered liquid product yield   |
| $f_i$                   | Response factor of gas component i   |
| $A_i$                   | Peak area of gas component i   |
| $m_i$                   | Mass concentration of gas component i  |
| $M_i$                   | Mass of gas component i  |

# CHAPTER 1

## Introduction

Upgrading of Alberta oil sands bitumen produces large amounts of heavy gas oil (HGO). This product stream is a very important blend component of the synthetic crude oil pool. An important target for bitumen upgrading is to maximize the quantity and quality of the distillate product, which means maximizing the naphtha fraction at the expense of the HGO. Coking processes have a leading role in bitumen upgrading industry due to their low investment and operation costs. Compared with widespread use of delayed coking, fluid coking has some attraction due to its higher yield of liquid product and lower yield of coke. However, there is still a big potential to further improve the operation of fluid cokers by optimizing the vapor and liquid phase cracking. In this process, thermal cracking occurs in both liquid phase and vapor phase prior to escape of products out of reactor. Vapor phase cracking is unfavorable because it tends to reduce the yield and quality of liquid product by over-cracking the evolved distillate components. The resulting heavy aromatic distillate is less attractive for diesel fuel, and the use of this low-quality feed in steam cracking to produce petrochemicals is a big challenge, which requires further investigation. As a result of these factors, study on vapor phase cracking of bitumen derived distillate relates to both current upgrading technologies and future upgrading and petrochemical processes.

In this work, coker HGO derived from Athabasca bitumen was employed as a representative of gas-phase cracking components in fluid cokers and a potential feed for

steam crackers. HGO was fully vaporized and reacted in a tubular flow reactor over the temperature range of 600-700 °C and at atmospheric pressure. Gas, liquid and coke products were collected for yields measurement and liquid products were analyzed by simulated distillation, elemental analysis and <sup>13</sup>C-NMR. The objectives of this research were:

- To obtain kinetic data at high temperature and analyze the quality of the liquid products, to establish the link between reaction kinetics and product quality.
- To investigate the reactivity of bitumen-derived HGO and its impact on reaction kinetics.
- To study distributions of gas products and light olefin yields to test the performance of bitumen derived HGO as steam cracker feed.

This work is the first to examine pure vapor phase cracking of the highly aromatic-naphthenic gas oil from coking of Athabasca bitumen, and to determine the quality of the resulting liquid products.

# CHAPTER 2

## Literature Review

### **2.1 Industrial Upgrading Processes**

Coking and hydro-conversion are the two main processes to upgrade oil sands bitumen. Although the latter process features high volumetric yield of liquid product with no coke formation, it has a high capital and operating cost and the catalysts tend to be deactivated easily by the heavy bitumen feed. In comparison, the low cost and easy operation of cokers make them attractive for the majority of upgrading plants. Coking processes convert the feed into light ends, liquid products and solid coke. Delayed coking and fluid coking are the two basic technologies used in the industry.

Delayed coking is a very common process in refineries as an economical and efficient way to process high carbon and metal content residue. It has also been selected to upgrade oil sands bitumen given its low requirement on feed quality. The process is composed of heater, coke drums and fractionator. A schematic diagram for delayed coking is illustrated in Figure 2-1.

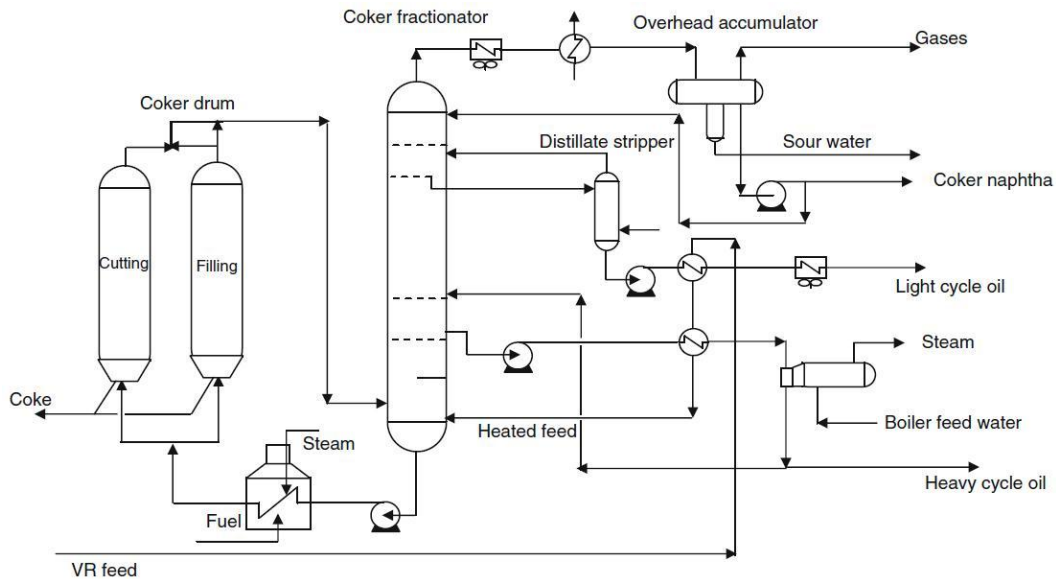


Figure 2-1. Schematic diagram of delayed coking process (Fundamentals of Petroleum Refining by Fahim et al. Copyright @ 2010 Elsevier B.V. Reproduced with permission of Elsevier B.V. in the format Thesis via Copyright Clearance Center)

The furnace heats the feed from 350 °C to 500 °C and passes it to one of the coke drums. Cracking and coking of liquid phase starts at the bottom of drum. The vapor products, which are distillate and gases, evolve and rise up to the top of drum followed by quenching in distillation tower. Different fractions of product are separated there. Coke is accumulated in the first coke drum gradually until it is filled up. The feed is subsequently switched to the second coke drum, while the first one proceeds with a cycle of cooling and hydraulic decoking. Two drums are operated based on a specific alternating cycle to accommodate continuous feeding (Gray, 2010; Gray, 1994).

Delayed coking possesses the advantage of higher quality liquid product due to long residence time in liquid phase cracking at moderate temperature. However, the yield of liquid product is poor given that more materials are trapped in the coke with longer residence times (Gray et al., 2001; Rana et al., 2007). Furthermore, the semi-batch

process is a big challenge for processing high volumes of bitumen feed due to rapid coke accumulation in drums and furnace tubes (Gray, 2010). In order to handle high coke production, the continuous process fluidized-bed coking was developed during the 1950's. The process diagram is show in Figure 2-2.

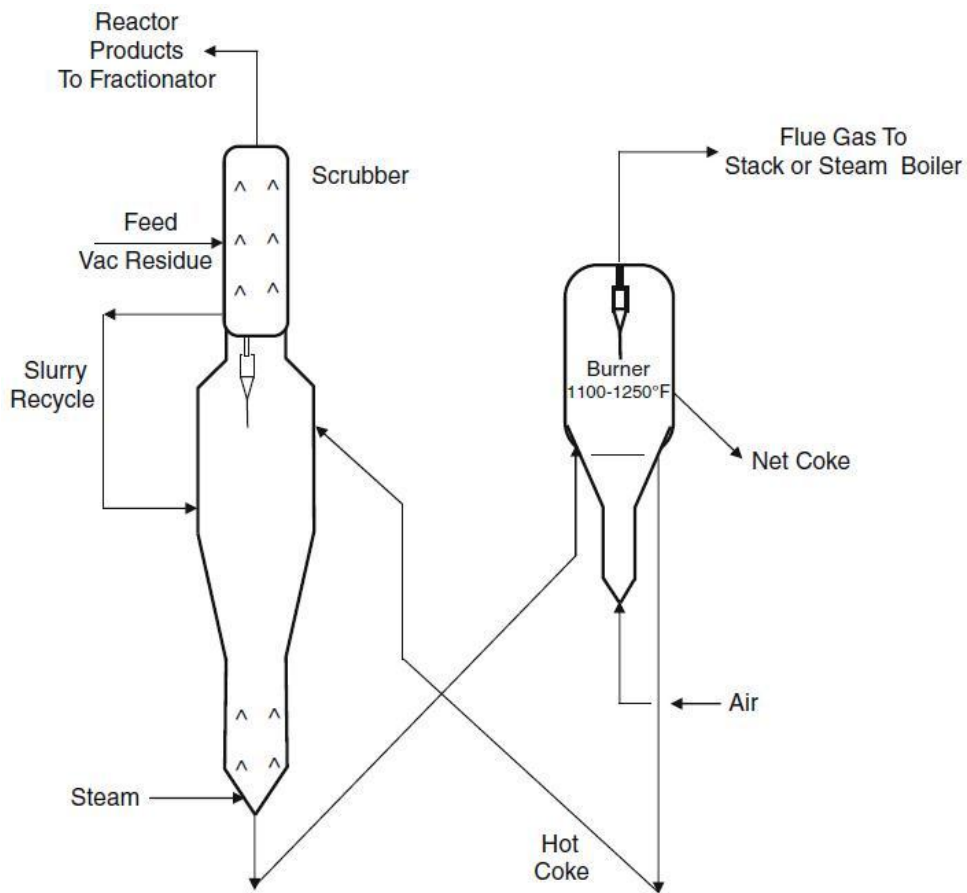


Figure 2-2. Schematic diagram of fluid coking process (Fundamentals of Petroleum Refining by Fahim et al. Copyright @ 2010 Elsevier B.V. Reproduced with permission of Elsevier B.V. in the format Thesis via Copyright Clearance Center)

This process is composed of a fluidized-bed reactor and coke burner. Steam is introduced at the bottom of the reactor to strip coke particles of liquids and fluidize the bed. Bitumen feed is sprayed on the fluidized hot coke particles in the reactor and liquid phase cracking occurs on the surface of the particles at temperature circa 540 °C. The

reacting component is primarily the vacuum residue fraction of the bitumen feed. The cracked products, including the HGO fraction, escape from the liquid phase and crack in the vapor phase until they rise up to the top of the reactor. The product vapors are cleaned of entrained coke particles by cyclones and quenched by the cold feed stream in the scrubber section. The products are subsequently fractionated into gases and distillates (Gray, 2010; Gray, 1994).

The wet coke product at the bottom of the reactor is stripped of liquids and transported into the burner with about 20 % burned at circa 630 °C to provide heat to the reactor. Most of the remaining coke is circulated between reactor and the burner as heat carrier and a small portion of them become net coke product. Coke yield for fluid coking only is 1.2 kg/kg MCR compared with 1.76 kg/kg MCR for delayed coking (Gray, 2010). Rana et al. (2007) pointed out that the short residence time of fluid coking yields higher quantities of liquids and less coke, but the products have lower quality.

The application of fluidized bed operation gives higher liquid yield and lower coke yield compared with delayed coking. However, existing fluid cokers can still be further modified to increase the quantity and quality of its liquid product by optimizing vapor and liquid phase cracking. Vapor phase cracking reduces the yield and quality of desired liquid product due to formation of light ends, which leaves behind highly aromatic and low hydrogen content liquids. Consequently, it needs to be minimized by either optimizing current operating conditions or developing new reactor technologies.

## **2.2 Novel Coking Technologies**

The ultimate goal of coking processes for bitumen upgrading is to maximize the yield and quality of liquid product. This necessitates sufficient time to ensure full reaction of

feed and immediate quench of primary reaction before secondary reactions occur. As a result, most novel coking technologies focus on short residence time in vapor phase to eliminate over-cracking while still keep liquid phase residence time long enough.

### **2.2.1 ETX IQ Cross Flow Coking**

This novel coking process was proposed by Envision Technologies (Brown et al., 2005). In order to optimize both liquid and vapor phase residence times, a cross-flow fluidization concept is applied to decouple both phases, in which the solids flow is perpendicular to the fluidization medium. In the ETX design, the fluidised bed of hot solids flows horizontally through the reactor: fluidising gas is introduced into the bottom of the reactor, perpendicular to the bulk flow of solids. The heavy oil feed is sprayed onto the hot fluidised solids introduced at one end of the unit. The reactions take place along the length of the reactor-evolving product into the gas phase. The solid phase carrying the feed approaches plug flow, which features high mean velocity in the reactor. As a result, the size of reactor can be minimized given the same throughput. With the same reactor length, the height can be very shallow, which helps to reduce vapor phase residence time. This design also allows lower temperature operation to minimize over-cracking of the liquid products that evolve in the gas phase. As a compromise, the liquid phase residence time is longer but does not affect gas phase residence time because the bed height remains unaffected.

This process was demonstrated as a one bbl/day pilot unit in the National Center of Upgrading Technology. The pilot testing proved the significant improvement of liquid yield and quality as compared with conventional delayed and fluid coking. The main challenge is to validate its operability in large scale.

### **2.2.2 LR-Process**

The LR-process was developed by Lurgi. The force required to counter gravity and fluidize the solid particles is provided mechanically through rotation of the augur-like internal of the reactor. Vapor products evaporate in the course of reaction and are directed to fractionation. The circulating solids covered with coke are burned in combustor to provide heat for reaction. The movement of solids approach plug flow and the vapor phase residence time is short, which prevents over-cracking. The vapor and solid residence times achieved are 0.5 to 1.0 s and 5 to 20 s, respectively (Wiehe, 2008).

This process features complex mechanical design, which may cause some severe problems during operation. Coke would build up fast on each surface inside of the reactor and shutdown the unit frequently. As coking proceeds, the viscosity of reacting material tends to be much higher. This brings heavy duty to the motor drive and necessitates frequent replacement.

### **2.2.3 Ivanhoe Heavy to Liquid (HTL) Process**

HTL upgrading technology (Silverman et al., 2011; Kuhach et al., 2009; Veith, 2007) was designed to cost effectively process heavy oil in the field and provide a significantly upgraded synthetic oil product along with by-product energy which can be used to generate steam or electricity. HTL upgrading is a continuous, short contact time thermal conversion process. It uses a circulating transported bed of hot sand in the system to quickly heat the feedstock and converted it to more valuable products. The process is made up of three sections: fractionation, reactor and reheater. The whole heavy oil feed is sent to a series of distillation towers, where light fraction is removed and later

blended with the upgraded liquid product to form synthetic crude oil. The heavy residue fraction is passed into the RTP reactor and mixed with hot circulating silica sand. The sand coated with feed rises up through the reaction zone by transport gas and thermal cracking occurs. Cracked product is vaporized and coke is deposited on the sand. All these components are carried out by transport gas and separated in the cyclone system. The fluids are quenched rapidly and vapors condensed to liquid product. The residence time in the reactor is less than a few seconds, which minimizes secondary cracking reactions in the vapor phase, but which also limits the conversion of the liquid feed to cracked products in the vapor phase. The condensed liquid product can either be routed to product tanks or sent back to fractionators for recycle operation. The coke covered sand is directed to RTP reheater for carbon removal by combustion. Part of the heat is provided for reaction by circulating sand and the rest may be used to generate high pressure steam. This whole process is very similar to fluid catalytic cracker with exception using sand as circulating medium instead of catalyst pellets.

The commercial demonstration facility processed bitumen in both a high yield (once through) and high quality (recycle) modes with 1000 bbl/day capacity. Higher liquid product yield (90 vol%) than delayed coking (82 vol%) and fluid coking (79.2 vol%) was achieved due to short residence time operation. The product quality is also dramatically enhanced given the fact that viscosity, boiling range, total acid number, sulphur and metal content are all reduced. The feed and product properties are compared in Table 2-1 for Athabasca bitumen.

Table 2-1. Comparison of feed and HTL product properties in two operation modes (Freel, B. et al. 2002-2005)

| Property                  | Athabasca Bitumen | Once Through | Recycle |
|---------------------------|-------------------|--------------|---------|
|                           | Feed              | Product      | Product |
| Viscosity, cSt @<br>40 °C | 40,000            | 150          | 60      |
| Residue Content,<br>wt%   | 52                | 30           | 2       |
| TAN, mgKOH/g              | 3.7               | < 0.5        | < 0.5   |
| Sulfur Content, wt%       | 4.9               | 4.0          | 3.6     |
| Metal content             |                   |              |         |
| Ni, wt ppm                | 184               | 110          | 18      |
| V, wt ppm                 | 471               | 270          | 47      |

However, some potential problems exist in this process. The circulating material sand may cause severe abrasion for the equipment. Distillation may contribute more to product yield than actual cracking reaction.

#### 2.2.4 ART Process

This process, developed by Englehart, is based on the fluid catalytic cracking process. An inert solid is applied as the circulating heat carrier. The whole process is nearly the same as foregoing HTL process. A 50,000 bbl/day ART unit was built in Kentucky in 1983. With cold lake bitumen as feed, an ART unit would give a product with about 10 % of 524 °C+ material, which corresponds to over 80 % residue conversion. The short contact time with high temperature operation gives a new approach to produce olefins from oil sands bitumen. Vogiatzis et al. (1989) reported that over 15 % of the feed was converted to ethylene at residence time of 65 ms and temperature of 900 °C. However, fouling is a

major problem due to unconverted feed on the solid particles and polymerization of olefins.

### **2.2.5 Summary**

Some other novel coking technologies such as fluid thermal cracking (FTC) process, Chattanooga process and discriminatory destructive distillation process were also proposed and developed to some extent. Although some differences are clear between the different processes, the heat source for thermal cracking reaction is mainly hot solids: sand or coke particles. The way to heat solids is also similar in all these processes: fluidization or pneumatic transport operation. Almost all these technologies except ART process are under pilot testing or commercial demonstration and not commercialized for large-scale industrial production. The main problem in testing is fouling, which results in shutdown of operation. Many other unpredictable technical and economic issues also need to be analyzed and solved before these processes become dominant in industry.

### **2.3 Improvements on Current Fluid Coking**

Modification on existing fluid coking technology becomes very attractive given the potential to further improve performance within an existing process. Research has been dedicated to understanding the fundamentals of the fluid coking process in order to improve its performance. An analogy was built between bitumen coking process and granulation by Gray (2002) to analyze defluidization, fouling and distribution of liquid feed on particles in fluid cokers. A three-step mechanism for feed distribution on coke particles in fluid coking was proposed. It suggested that agglomeration can be avoided when internal cohesive forces between two particles are smaller than external forces by

collisions with bed particles. Thin film cracking was found to eliminate agglomeration effectively, which avoid defluidization and fouling issue in fluid coking reactor. The role of pressure in coking of thin films of bitumen was studied by Gray et al. (2007). The effects of temperature and pressure on coke yield were insignificant in the case of thin films (20  $\mu\text{m}$ ). In thick film cracking, coke yield increased dramatically with increasing pressure due to suppression of bubbling when the reaction temperature is low. At higher temperature, the effect of pressure was proven to be negligible.

However, almost no research is focused on vapor phase cracking step in fluid coking, in particular its effect on liquid product yield and quality.

#### **2.4 Industrial Petro-Chemical Processes**

Conventional non-catalytic steam cracking process (Chaudhuri ,2011) is widely used to produce petrochemical feed materials such as ethylene and propylene (Figure 2-3). The feedstock is mixed with steam at a specific ratio range and passes through the furnace with temperature above 800 °C. The thermal cracking occurs in pure vapor phase at such a high temperature. The cracked vapor is quenched at different stages and undergoes cryogenic separation to obtain the desired olefins. Among conventional feeds to steam crackers, ethane is most favored owing to its high olefin yields and low coke deposition in the furnace tubes. However, it is only widely used in North America due to the abundant supply of natural gas. Crude oil derived naphtha is introduced as feed in most olefin production plants, but it suffers from supply shortage due to competing purposes to produce gasoline and aromatics.

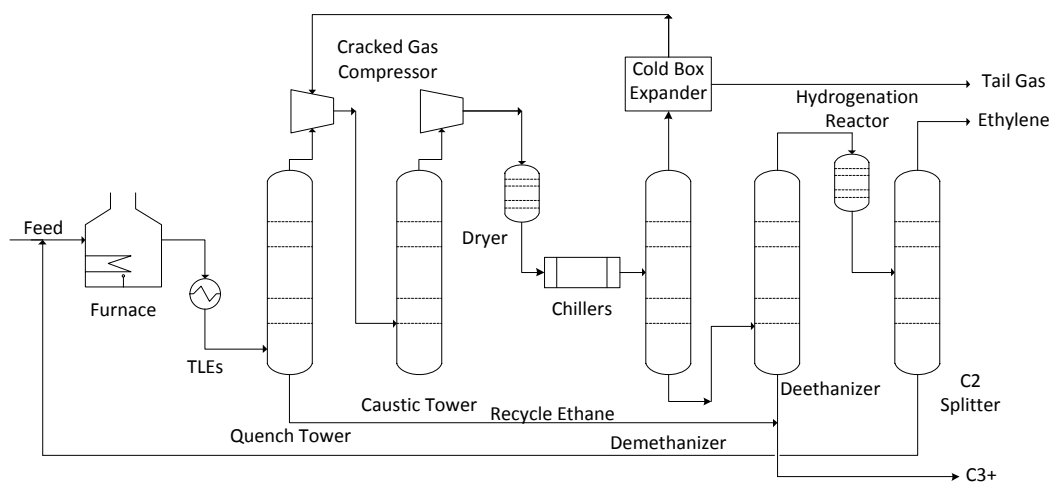


Figure 2-3. Schematic diagram of naphtha-based steam cracking process (Fundamentals of Petroleum and Petrochemical Engineering by Chaudhuri)

With the expansion of the petrochemical industry, exploring alternative feedstocks becomes very important. Vacuum gas oil was introduced as feed to produce ethylene in a steam cracking plant with capacity 250000 tons/year at Port Jerome, France. The whole process follows traditional designs with exceptions in the cracking furnaces, quench, and the primary fractionator. The special feature of the furnace is the use of onstream decoking to remove the higher than normal amounts of coke deposited. When a furnace requires decoking, oil feed is removed from the tubes and replaced with water. Water and dilution steam rates are adjusted for decoking conditions. The principle mechanism of coke removal is through gasification to carbon oxides. Transfer line exchangers are also replaced by two parallel scrubber towers to quench the effluent gases due to high coking tendency. Coke particles are completely scrubbed off from the gases in the tower. The primary fractionator bottoms stream was selected in preference to scrubber tower bottoms for pump-around heat removal to minimize heat exchanger

fouling. The performance of VGO and typical light virgin naphtha (LVN) was compared, which is shown in Table 2-2.

Table 2-2. Product distribution from VGO and naphtha (Greene, 1969)

| <b>Product</b>  | <b>VGO (wt%)</b> | <b>Naphtha (wt%)</b> |
|-----------------|------------------|----------------------|
| Ethylene        | 16.6             | 31.3                 |
| Propylene       | 13.3             | 16.2                 |
| Butadienes      | 4.1              | 4.7                  |
| Liquid products | 44.6             | 19.4                 |

Considering feedstock, co-product and operating cost, the ethylene production cost from VGO was estimated to be \$258/ton compared with \$271/ton from LVN with advantage of \$13/ton based on Port Jerome, France in 1967 (Greene, 1969). Therefore, VGO steam cracking can be quite attractive depending on the cost and availability of VGO and the market for co-products. In Alberta, upgrading of oil sands bitumen provides abundant supply of HGO streams, which can be used as a potential feed. Based on the economic point of view, the price is very competitive especially when integrated with bitumen production, upgrading and refining. Nevertheless, the quality of this feed is much poorer than other conventional petroleum fractions, which may cause low olefin yields and high coke deposition. This brings a big challenge to feed it to an industrial steam cracker. However, high temperature and short residence time operation may offer a great potential.

## **2.5 Composition and Structure of Bitumen and Its Derived Heavy Gas Oil**

Oil sands are composed of 16 wt% bitumen and water as well as 84 wt% sand and clay. Bitumen is generally produced from oil sands by either open pit mining or in situ production. The overall properties of bitumen are not attractive due to low API gravity,

high content of vacuum residue, sulphur, nitrogen, metals and high viscosity. The quality is poor given its low hydrogen content (circa 10 wt%) and H/C ratio (circa 1.5). Comparison of conventional light crude and bitumen is shown in Table 2-3.

Table 2-3. Comparison of light crude and bitumens (Gray, 2010)

| Property  | Light crude | Athabasca bitumen | Cold lake bitumen |
|---|-------------|-------------------|-------------------|
| API gravity   | 40.8        | 10                | 9                 |
| Sulfur, wt%   | 0.3         | 4.4               | 4.9               |
| Nitrogen, wt%   | 0.08        | 0.4               | 0.5               |
| Metals, wppm <sup>2</sup>                               | 3.2         | 220               | 280               |
| Viscosity, m <sup>2</sup> /s × 10 <sup>6</sup> at 40 °C | 4           | 5000              | 7000              |
| Vacuum residue, 524 °C+, vol%                           | 12.9        | 52                | 52                |

Bitumen derived HGO is produced by primary upgrading, mainly via coking processes.

The properties of HGO derived from Athabasca bitumen are tabulated in Table 2-4.

Table 2-4. Properties of Syncrude coker gas oil produced from Athabasca bitumen (Kanda et al., 2004; Yui, 1995)

| Property                | Value  | Property                   | Value |
|-------------------------|--------|----------------------------|-------|
| Density at 20 °C (g/mL) | 1.0017 | Aromatic carbon content, % | 38.12 |
| Elemental analysis      |        | MCR, %                     | 1.98  |
| Carbon, wt%             | 84.21  | Boiling fractions, wt%     |       |
| Hydrogen, wt%           | 10.17  | IBP-177 °C                 | 0     |
| Sulfur, wppm            | 43320  | 177-343 °C                 | 12.11 |
| Nitrogen, wppm          | 3783   | 343 °C +                   | 87.89 |

The chemical species in bitumen have been heavily degraded by bacterial action. Unlike light crude oil which is abundant in n-alkanes, most alkanes in bitumen have been

removed with the lighter boiling fractions. The remaining oil has a low concentration of paraffinic groups, and many of these groups are side chains attached with large molecules mainly polycyclic aromatics. Most heteroatoms (S, N,O) are also left behind in the bitumen (Gray, 2010).

In terms of hydrocarbon groups, aliphatics (paraffins, isoparaffins, olefins and naphthenes) and aromatics are the possible constituents of bitumen and its derived HGO. They can also be classified into saturates which are the valuable portion of bitumen and less favourable aromatic fraction. Straight-chain paraffins are absent in bitumen due to biodegradation. The surviving species are usually branched isoparaffins. However, n-alkanes can be formed in bitumen derived HGO by cracking off side chains from alkyl aromatics. As in conventional crude oil, raw bitumen also lacks olefins, but they are found in coker-derived HGO after thermal cracking. Naphthenes containing one to six fused rings are identified in bitumen residues and gas oils. Some of these naphthenic compounds originate from the bacteria that attacked the original oil. The most abundant biomarkers detected are rearranged and partly degraded cyclic terpenoid, along with some steroid hydrocarbons. The aromatic fraction of gas oils can be divided into monoaromatic, diaromatic, triaromatic and polyaromatic subfractions. Aromatic compounds ranging from alkylbenzenes to large condensed polyaromatic and heteroaromatic molecules are possible in bitumen and its derived HGO (Gray, 2010; Strausz, 2003).The aromatic contents of different bitumens are listed in Table 2-5.

Table 2-5. Aromatic contents of different bitumens (Strausz, 2003)

| <b>Bitumen</b> | <b>Mono-</b> | <b>Di-</b> | <b>Polyaromatic</b> | <b>Total</b> |
|----------------|--------------|------------|---------------------|--------------|
| Athabasca      | 8.3          | 3.8        | 23.8                | 35.9         |
| Cold Lake      | 8.1          | 3.6        | 24.4                | 36.1         |
| Peace River    | 8.6          | 3.3        | 30.2                | 42.1         |

The aromatic rings are substituted with alkyl groups or bridges to other aromatics. The sing-ring aromatics have low heteroatom content, high H/C atomic ratio and low molecular weight, which tend to be biodegraded. Consequently, they are nearly depleted in raw bitumen (Gray, 2010). However, single-ring aromatics are formed during upgrading process. Meanwhile, highly condensed aromatic groups containing more rings than those in raw feed may also be contained in upgraded bitumen. Most aromatic rings are intact during thermal processing and either forms coke or stay in the bitumen derived HGO. Hydroaromatics, partially hydrogenated aromatics, also present in bitumen. They are likely from naphthene rings by dehydrogenation (Gray, 2010).

The other important constituents of bitumen and its derived distillate products are heteroatomic groups. Sulfur is most abundant in raw bitumen (5-6 wt%) and exists in two forms: thiophenic compounds as well as sulfides and sulfoxides. Two-thirds of the sulfur is present primarily as alkylbenzo- and higher condensed thiophenes. Most of the thiophenic compounds are found in the aromatic rings which are resistant to treatment. Sulfides and sulfoxides are chemically reactive and interfacially active molecules. Sulfides are also susceptible to oxidation to sulfoxides. These sulfur species are accumulated in aliphatic groups, which are easy to remove by thermal cracking. As a result, most sulfur survives as thiophenic compounds in bitumen derived HGO. Nitrogen is the least abundant heteroatom in bitumen (0.3-0.7 wt%). It also exhibits in two forms:

the non-basic derivatives of pyrole, and the basic derivative of pyridine. Both types are highly resistant to removal due to strong C-N bond and its highly stable aromatic structure. Some of the nitrogen compounds in bitumen are rejected into coke by thermal processing, leaving HGO with a lower nitrogen content. Oxygen occurs in acids and esters in bitumen, which are easier to remove than nitrogen. Metals such as vanadium and nickel compounds are also contained in bitumen mainly as substituted porphyrins. Vanadium and nickel atoms are coordinated with nitrogen, which show remarkable stability and resistance to processing (Gray, 2010; Strausz, 2003). Bitumen derived HGO is low in metal content which is trapped in the coke.

Wiehe et al. (1994) proposed pendant-core building block model for petroleum residue (Figure 2-4). The small building blocks are volatile and become liquid products when the rest of the residua molecule is cracked off while the core building block remains non-volatile and ends up with coke. These two building blocks are linked by thermally labile bonds. The hydrogen content of the pendants depend on the boiling point range and aromaticity of the residuum while cores have universal hydrogen content value of  $3.8 \pm 0.3$  wt%. This model gives a linear relationship between Conradson carbon residue and hydrogen content for petroleum molecules.

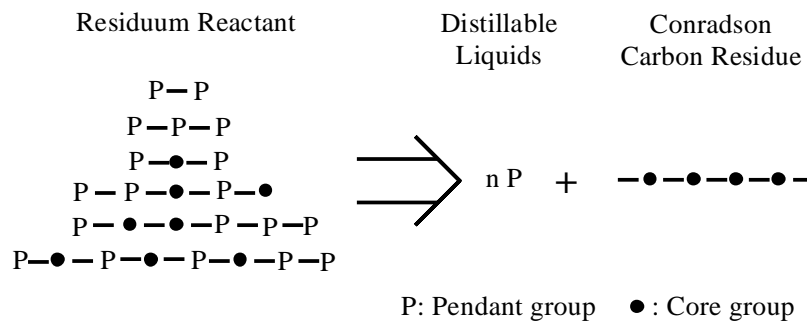
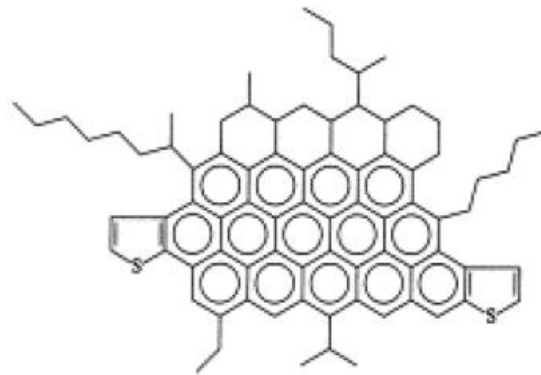
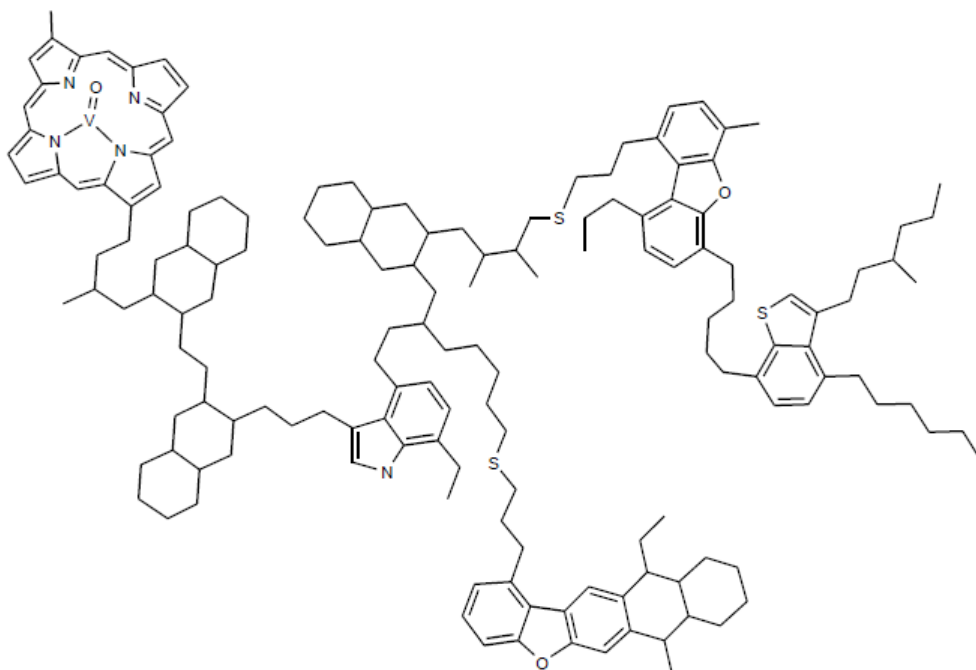


Figure 2-4. Pendant-core building block model (Wiehe et al., 1994)

Bitumen can also be separated into saturates, aromatics, resins and asphaltenes on the basis of solubility plus adsorption characteristics. Asphaltenes are the materials that soluble in toluene and insoluble in n-alkane (n-pentane or n-heptane). They are the highest molecular weight fraction in bitumen and contain C, H, N, Ni, O, S, V and various types of paraffinic, naphthenic, and aromatic groups (Gray, 2010). Some of the bitumen derived HGO is also formed by cracking of asphaltene fraction. Two contradictory views of the asphaltene structure are present: the pericondensed or the archipelago structures (Figure 2-5).



(a) Pericondensed structure (Dickie et al., 1967)



(b) Archipelago model (Sheremata et al., 2004; Gray, 2003)

Figure 2-5. Proposed models for asphaltene structure

The pericondensed model is based on a core aromatic group containing a large number of fused rings with pendant aliphatic. The proposed Yen model by Dickie et al (1967) and modified Yen model by Mullins (2009) are focused on pericondensed models. The archipelago model claims that asphaltenes are composed of two to four small ring aromatic clusters connected by aliphatic and sulfur side chains. Sheremata et al. (2004) used Monte Carlo method to construct the quantitative molecular representation of asphaltenes as archipelago. This molecular model was consistent with various analysis results. Gray (2003) cracked asphaltene under severe conditions and gave wide range of products, which is more consistent with archipelago model than pericondensed model. The largest fraction of the liquid product was found to be in the gas oil range (343-524 °C). Strausz et al. (1992) performed mild pyrolysis on Athabasca asphaltenes and produced some aromatics with only one to three rings. This result also strongly

corroborates archipelago model. Since some asphaltene fractions contribute to HGO during cracking process, the archipelago model also provides important implications on bitumen derived HGO structure. The breakage of bridges between ring groups appears to be the dominant mechanism for the formation of HGO, along with some loss of side chains in the highest fractions of the vacuum residue fraction.

## 2.6 Mechanism for Cracking of n-alkanes

Free radical chain reaction gives an explanation and it is the basic mechanism for thermal cracking of n-alkanes. Rice and Hertzfeld (1934) and Kosikakoff and Rice (1943) proposed RK mechanism for gas phase cracking of n-alkanes. LaMarca et al. (1993) suggested LLKC mechanism for liquid phase cracking of n-alkanes. Both of them are based on free radical chain reaction and are comprised of three steps: initiation, propagation and termination. The mechanism for both liquid and gas phase thermal cracking is summarized in Figure 2-6.

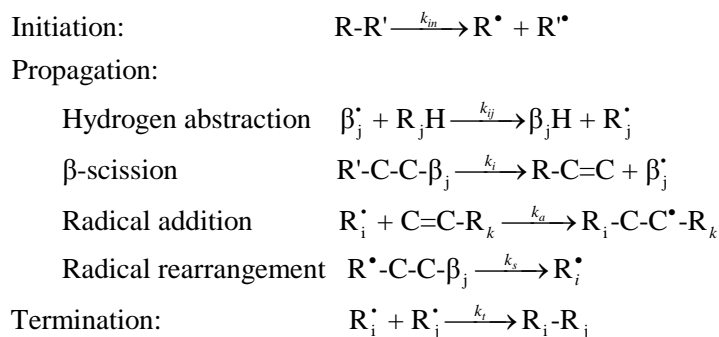
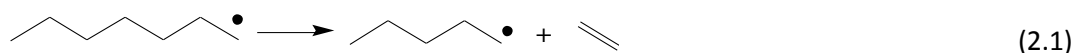


Figure 2-6. Free radical chain reaction mechanism for hydrocarbons (Gray, 2010)

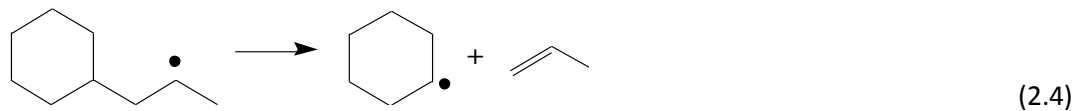
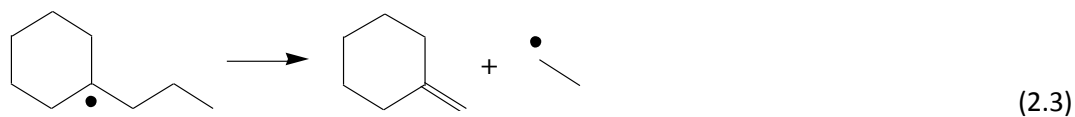
Free radicals are formed in initiation step, which needs high energy to break the bonds. The C-C and C-H bonds in n-alkanes have energies of 344 kJ/mol and 398 kJ/mol, respectively. Nevertheless, the propagation step has much lower energy requirement.

The overall activation energy (< 300 kJ/mol), which is much lower than bond energies, is the combination of all the steps. The highly reactive free radicals exist in very low concentrations and participate in a chain process to give conversion of feed. Hydrogen abstraction and radical addition are favored in high density of reacting species while  $\beta$ -Scission always occurs.  $\beta$ -Scission and radical addition are literally reversible reactions. Among all the propagation steps,  $\beta$ -Scission is the only step involving breakage of chemical bond. Three types of  $\beta$ -Scission on n-alkanes are present.

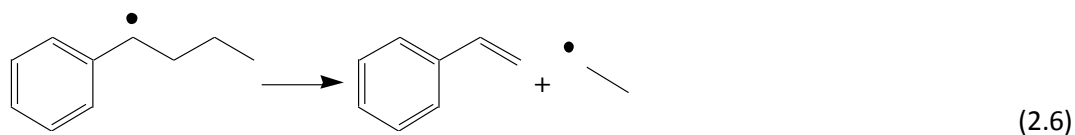
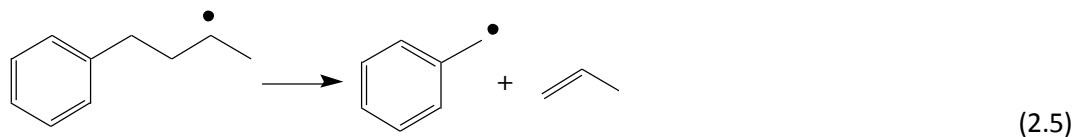
Straight chains:



Side chains and bridges on cycloalkanes:



Side chains and bridges on aromatics



## 2.7 Kinetics of Cracking of n-hexadecane as Model Compound

In order to explore the mechanism for thermal cracking of gas oil, n-hexadecane was widely studied as a model compound by cracking it in both liquid phase and gas phase.

Wu et al. (1996) compared liquid phase and gas phase thermal cracking of n-hexadecane at the same conditions with temperatures of 330-375 °C. The first-order kinetics of cracking in both phases were shown to be similar with activation energies in liquid phase 290 kJ/mol and gas phase 270 kJ/mol. However, liquid phase cracking produced both alkanes and alkenes with preference on alkanes at high conversion while gas phase cracking always favored alkenes. The yield of gas products from vapor phase cracking was also found to be much higher. This was in agreement with Ford (1986) who commented that the kinetics of liquid-phase thermal decomposition were similar to those of gas-phase thermal decomposition with activation energy for both was about 257 kJ/mol. He also pointed out that equal amount of straight-chain alkanes and alkenes were produced from liquid phase cracking at low conversion while additional branched-chain alkanes were formed at high conversion. According to Ford (1986) and Fabuss et al. (1962), the cracking products of n-hexadecane are strongly dependent on reactant concentrations. In the liquid phase, bimolecular reactions like hydrogen abstraction and addition of olefins are favored over  $\beta$ -scission while the opposite is true in the gas phase. This explains the difference of product distribution in liquid phase and gas phase cracking of n-hexadecane.

Watanabe et al. (2000) conducted pyrolysis experiments on n-hexadecane at 400-500 °C with existence of both liquid phase and gas vapor phase. The main products were n-alkanes and 1-alkenes. The 1-alkene/n-alkane ratio was exhibited to decrease with

increasing n-C<sub>16</sub> concentration. The overall activation energy was different given different n-C<sub>16</sub> initial concentrations: 196 kJ/mol at 0.07 mol/L and 263 kJ/mol at 0.22 mol/L. This was due to the change of the amount at  $\beta$ -scission and H abstraction with n-C<sub>16</sub> initial concentrations.

Khorasheh et al. (1993) carried out thermal cracking of n-hexadecane at 13.9 MPa and 380-460 °C in three cases: no solvent, with tetralin or aromatic solvents. Major reaction products were C<sub>1</sub> to C<sub>14</sub> n-alkanes and C<sub>2</sub>-C<sub>15</sub>  $\alpha$ -olefins under such a high pressure. Bimolecular reactions (hydrogen abstraction and radical addition) were found to be significant under high-pressure conditions. In the absence of solvent, the product distributions were highly conversion-dependent. The activation energy was estimated to be approximately 256 kJ/mol. Adding tetralin, 1- and 2-alkyltetralins were also produced and production distribution of n-alkanes was nearly equimolar due to fast rate of hydrogen abstraction from tetralin. The apparent first-order rate constants decreased with conversion of n-hexadecane. Selectivities for n-alkanes were exhibited to increase with increase of conversion. Cracking in aromatic solvents also generate biphenyl and higher alkylbenzenes as products. The apparent first-order rate constants increased with initial concentration of n-hexadecane. High initial concentration was discovered to result in high molar selectivities for n-alkanes. Cracking of n-C<sub>16</sub> in both tetralin and aromatic solvents was shown to be slower than that without solvent. The inhibition of cracking rate with these solvents indicated that interactions exist between aromatics and n-hexadecane. This gave an important implication for cracking of bitumen residue which contains both aliphatic and aromatic compounds. Jackson et al. (1995) cracked n-hexadecane at temperatures ranging from 300 to 370 °C and pressures of 150 to 600 bars to study oil stability. Pressure was found to have a retarding effect on the rate of

reaction. The overall apparent activation energy was determined to be 310 kJ/mol in the high pressure range. They ascribed estimated high activation energy to high pressure at low temperature.

Fairburn et al. (1990) studied the vapor phase ultrapyrolysis kinetics of n-hexadecane at temperatures 576-842 °C in a novel micro-reactor. High temperature and short residence time operation was proven to favor desirable products and eliminate secondary reactions. Peak ethylene production (28 wt%) was realized at 842 °C and 500 ms. The obtained activation energy was circa 165 kJ/mol which was significantly lower than other reported by other researchers. This probably attributes to use of only three data points to evaluate activation energy. Depeyre et al. (1985) investigated pure n-hexadecane thermal steam cracking in tubular flow reactors in the temperature range of 600-850 °C. The overall decomposition of n-hexadecane was assumed to be a first-order reaction with the activation energy of 238 kJ/mol at low conversion. Temperature, steam dilution and residence time all had impacts on light olefins production. They also developed a complementary kinetic model for different temperatures. At low temperature range, basic reactions covering initiation, propagation and termination were included. At high temperature range, secondary reactions turned to be important and were considered. Zhou et al. (1987) studied the vapor-phase thermolysis of several straight-chain alkanes and their mixtures including n-hexadecane at temperatures of 350-620 °C and atmospheric pressure. 1-alkenes were noticed to be major products from thermolysis of straight-chain alkanes. Low system pressure gave high selectivity to 1-alkenes. Thermolysis rate constants of alkanes in a mixture were found to be lower than for pure alkanes and decrease with increasing conversion. Fabuss et al. (1962) studied rapid thermal cracking of n-hexadecane in a flow reactor at temperatures of

600-700 °C and pressures of 200-1000 psig. The first-order rate constants at a specific temperature were found to be independent of pressure. The amount of coke deposit was too low to be detected.

Doue and Guiochon (1969) concluded that the rate of formation of alkanes in the pyrolysis of n-hexadecane was substantially reduced in the presence of an inert gas. H<sub>2</sub>S was found to have catalysis effect in the pyrolysis of n-hexadecane by Rebick (1981). It improved cracking rate but reduce the yield of light gases.

## 2.8 Mechanism of Cracking of Other Components of Gas Oil

In addition to n-alkanes, olefins, aromatics and naphthenes are the other major components of gas oil. Heteroatom components, particularly sulfur compounds, are also rich in gas oil fraction.

### 2.8.1 Reactions of Olefins

Olefins are not found in the virgin oil but exist in the gas oil fraction after undergoing cracking history. In general, the β-Scission cracking step produces one mole of saturated product and one mole of unsaturated olefin product in gas oil. The olefins can undergo addition reactions with radicals, further cracking and rearrangement (Gray, 2010). The addition reactions with radicals create larger molecules, which have potential to build coke material.



Further cracking of olefin radicals tend to form diolefins (Gray, 2010). Diolefins sequential proceed with rapid cyclization and aromatization, resulting in coke precursor.



The aromatic rings in groups R and  $\beta$  may favor rearrangement and end up with more stable and less reactive radicals.

### 2.8.2 Reactions of Aromatics

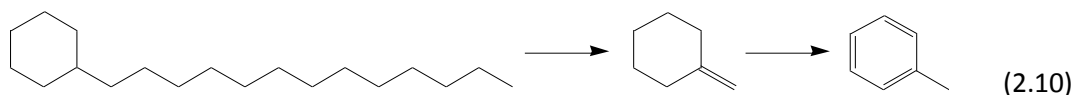
The C-C bonds in aromatic compounds are very strong due to the resonance stabilization (Gray, 2010). For instance, benzene and naphthalene have stabilization energies of 6 kcal/mol and 5.5 kcal/mol of C-C bonds, respectively. Therefore, aromatic structures are very stable under normal thermal cracking conditions and only cracking of side chains and bridges is significant. Some researchers found that aromatics had a retarding effect on thermal cracking. Zhorov and Volokhova (1981) performed pyrolysis on hexadecane, decalin, naphtha and kerosene gas oil with existence of naphthalene or phenanthrene at temperatures from 800-900 °C. The olefin yields decreased significantly with addition of PAHs excluding dilution effect. This was supported by Khorasheh and Gray (1993) who found that cracking of n-hexadecane in toluene and ethylbenzene was slower than cracking of n-hexadecane by itself.

### 2.8.3 Reactions of Naphthenes

Ring opening and dehydrogenation occur in the thermal cracking of naphthenic ring compounds. Ring opening is a variant of  $\beta$ -scission wherein the product of the bond breaking reaction is a single molecule (Gray, 1994). For the reaction of Decalin:



In the absence of hydrogen, the naphthenic groups can dehydrogenate to form aromatics in thermal cracking condition. In addition, partially hydrogenated aromatic compounds may also go through dehydrogenation and transfer hydrogen to other species. For the reaction of tridecylcyclohexane:



#### 2.8.4 Reactions of Sulfur Compounds

Compared with other heteroatom compounds, sulfur compounds play a vital role in thermal cracking. Thiophenic sulfur is unreactive due to its aromatic structure while thermal reaction of sulfides is quite favorable, evolving hydrogen sulfide. C-S bonds have a quite low energy of  $307 \pm 8$  kJ/mol compared with  $344 \pm 4$  kJ/mol for C-C bonds in n-alkanes. The free radical chain reaction mechanism of sulfur compounds is illustrated in Figure 2-7. The cracking of sulfides contributes a lot to the conversion of whole hydrocarbon. Furthermore, alkyl sulfides were found to initiate free radical chain reactions.

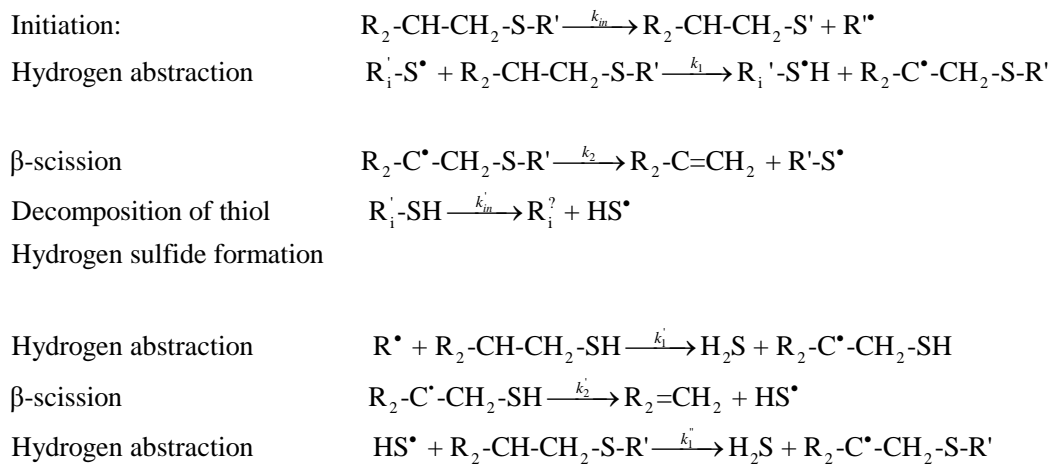


Figure 2-7. Free radical chain reaction mechanism for alkyl sulfur compounds (Gray, 2010)

## 2.9 Kinetics of Cracking of Gas Oil

### 2.9.1 Empirical Kinetics with No Chemical Information

Empirical kinetics of cracking of gas oils has been proposed at different operating conditions. Table 2-7 summarizes all these studies. The feasibility of gas oil as feed to conventional steam crackers remains uncertain in terms of the olefin yield and the amount of cracking fuel oil. Billaud et al. (1986) used a plug flow reactor to study steam cracking of vacuum gas oil (VGO) and hydrotreated gas oil at a temperature of 780 °C. Their results showed that the production of olefins increased while resins and asphaltene were eliminated after hydrotreatment. Consequently, hydrotreatment of VGO before feeding it to conventional steam cracker is a good opportunity. One of the key objectives to study the kinetics of gas oil pyrolysis is to predict product distributions and to determine optimum operating conditions. In order to predict the concentration of products as a function of operating conditions, Depeyre et al. (1989) cracked atmospheric gas oil (AGO) with steam in a tubular reactor at temperatures of 625-800 °C and obtained best yield of ethylene 27 wt%. Olefin and diolefin yields climbed to a maximum at 750 °C and decreased as the temperature increased. The kinetic model was developed based on both radical and molecular reactions and AGO was represented as a few simplified compositions (paraffin, isoparaffin, naphthenes and aromatics). This model gave the gaseous products distribution in agreement with the experimental data. Hirato et al. (1971) also did an experimental study on the effects of various parameters on olefin production by cracking gas oil in a tubular reactor at 800 °C. A kinetic molecular model was proposed and the gas oil was assumed to be mean molecular formula of  $C_{15.46}H_{29.02}$ . Inhibition was found in pyrolysis of gas oils by some studies. Su. et al. (1997) established a kinetic model of pyrolysis for Daqing light gas oil including the

inhibition of products to rate of pyrolysis and the variation of selectivities of primary reaction with temperature and conversion. They claimed that paraffines and naphthenes were the only reactants in the feed and the aromatics did not decompose. The activation energy for decomposition of feed was estimated to be 287 kJ/mol. Although inhibition was considered in their model, the chemical structure information was not included at all. Likewise, Zou et al. (1993) claimed that AGO pyrolysis was retarded by self-inhibition action based on experimental results, in which the rate constant for the primary reaction decreased with increase of conversion. It was noticed particularly at high conversion. They also suggested an expression to obtain modified rate constant  $k_F$  based on measured rate constant  $k_0$ .

$$k_F = \frac{k_0}{1 + \alpha X} \quad (2.11)$$

$$k_0 = A \exp(-E / RT) \quad (2.12)$$

$$\alpha = 3.50 \times 10^5 \exp(-10367 / T) \quad (2.13)$$

where  $\alpha$  is inhibition coefficient and  $X$  is conversion.

The predicted activation energy was 213 kJ/mol, which is reasonable. However, this expression is simply hyperbolic form which is obtained by fitting experimental data. It is purely empirical without any chemistry basis. Catalyst is sometimes used in thermal cracking of gas oil to reduce reaction temperature and adjust product distribution. However, the reaction mechanism and kinetics may differ from pure thermal cracking. Meng et al. (2005) studied catalytic pyrolysis of various sources of gas oil in the temperature range of 600 to 716 °C. Reaction temperature was found to be the most important operating condition. The properties of different feed and their product distributions under optimal conditions are listed in Table 2-6.

Table 2-6. Effect of feed properties on product distribution at 660 °C and 2.2 s (Meng et al., 2005)

|                                     | Daqing VGO | Daqing AR | Huabei AR | Daqing VR |
|-------------------------------------|------------|-----------|-----------|-----------|
| <b>H/C mol ratio</b>                | 1.89       | 1.82      | 1.79      | 1.76      |
| <b>Aromatic carbon, wt%</b>         | 6.84       | 10.90     | 13.00     | 13.76     |
| <b>Feed conversion, %</b>           | 99.01      | 98.18     | 99.12     | 98.44     |
| <b>Yields of light olefins, wt%</b> |            |           |           |           |
| Ethylene                            | 13.53      | 13.75     | 12.21     | 12.14     |
| Propylene                           | 22.60      | 22.58     | 19.27     | 19.93     |
| Butylene                            | 11.94      | 10.65     | 10.43     | 8.41      |
| <b>Total light olefins</b>          | 48.07      | 46.98     | 41.92     | 40.48     |

The yields of olefins go up with the increase of H/C mol ratio and the decrease of aromatic carbon content. As a comparison, thermal pyrolysis of Daqing AR was carried out at different temperatures. The ethylene yield was even higher and total olefin yield was close to that of catalytic pyrolysis at 700 °C. Consequently, thermal pyrolysis at high temperature has almost the same performance as adding catalyst in case of Daqing AR. Wang et al. (2009) did research on the catalytic cracking of coker gas oil (CGO) at lower temperature range from 480 to 530 °C, which aimed at producing liquid products. Various blending levels of CGO and VGO were studied to give limits of ratio. The 300-450 °C cut of CGO was found to exhibit lowest crackability due to high amount of polycyclic aromatics and nitrogen compounds.

Table 2-7. Various studies on empirical kinetics of cracking of gas oils

|                       | <b>Feed</b>                                       | <b>Temperature range</b> | <b>Reactor type</b>            |
|-----------------------|---|--------------------------|--------------------------------|
| Billaud et al. (1986) | Vvacuum gas oil & Hydrotreated vacuum distillates | 780 °C                   | Plug flow reactor              |
| Depeyre et al. (1989) | Atmospheric gas oil                               | 625-800 °C               | Tubular reactor                |
| Hirato et al. (1971)  | Gas oil   | 800 °C                   | Tubular reactor                |
| Su. et al. (1997)     | Daqing light gas oil                              | 670-760 °C               | NA                             |
| Zou et al. (1993)     | Atmospheric gas oil                               | 790-935 °C               | Tubular reactor                |
| Meng et al. (2005)    | Daqing VGO, AR, VR<br>Huabei AR                   | 600-716 °C               | Confined fluidized bed reactor |
| Wang et al. (2009)    | Daqing CGO<br>Dagang CGO<br>Daqing VGO            | 480-530 °C               | Confined fluidized bed reactor |

NA: None-applicable

### 2.9.2 Empirical Lumped Kinetics with No Chemical Information

Gas oil is a very complicated hydrocarbon mixture with thousands of components, which makes it difficult to develop kinetics on each species. For simplicity, some species with similar features can be grouped as a pseudo-component or lump. Different scale of lumped kinetics has been used to describe cracking of gas oil based on specific objectives. Simple lumped kinetic models were proposed to give the key kinetic information with limited experimental data. A 3-lump kinetic model was first developed by Weekman (1968) to describe catalytic cracking of gas oil. The model was comprised

of unconverted feed, gasoline and gas + coke as three lumps. Mohammad et al. (2003) developed a 4-lump model to represent the kinetics of vacuum gas oil (VGO) fluidized catalytic cracking over the temperature range of 550-650 °C. The reaction scheme contained four lumps: VGO feed, gas, gasoline and coke. The cracking was considered as a second-order reaction in the model. With reasonable kinetic parameters, both the 3-lump and 4-lump model was able to predict accurate product yields given the certain range of operating conditions. 5-lump kinetic models have been widely used to describe cracking of gas oil and it is enough to predict kinetics in most cases. Katica et al. (2010) modeled gas oil catalytic cracking in a fixed bed reactor using a five-lump kinetic model. Different from 4-lump kinetic model, the gas was further divided into two lumps: dry gas and LPG. The proposed model gave accurate predictions in the range of variables for the given feed, catalyst and temperature. Jorge et al. (1999) proposed the same five-lump kinetic model to describe catalytic cracking of gas oil in a microactivity reactor at temperatures of 480 °C, 500 °C and 520 °C. Both models had the advantage to predict two important products, dry gas and LPG, independently. Li et al. (2008) investigated catalytic pyrolysis of gas oil derived from oil sands bitumen in a fluidized bed reactor at temperatures of 600-700 °C. In order to predict olefin yields, a five-lump model including feed, gasoline, light olefins, light alkanes and coke was proposed, assuming second-order kinetics of gas oil cracking. The predicted ethylene yield was shown to increase monotonically as increase of reaction temperature and residence time. Consistent with experimental results, the yields of total light olefins reached maximum 38.63 wt% (ethylene: 10.90 wt%, propylene: 18.79 wt%, butylene: 8.94 wt%) under optimal conditions (660 °C and 2 s). Daqing atmospheric residue (AR) was used as feed in the same reactor at temperatures of 650-750 °C by Meng et al. (2003). Based on the

similar five-lump kinetic model, they claimed that the content of aromatics in liquid product was very high and they could not generate light olefins. Short residence time was found to be in favor of producing more olefins and less coke. More complicated lumped kinetic models have been introduced to better describe cracking of gas oil supported by enough experimental data. Meng et al. (2011) developed a seven-lump kinetic model to predict olefin yields in catalytic pyrolysis of HGO derived from Canadian synthetic crude oil at 600-700 °C. Rather than splitting gas products into two lumps: light olefins and light alkanes, the gas components were further divided into four lumps: propene + butane, propane + butane, ethane, hydrogen + methane + ethane. This was due to the difference in the formation mechanism between light gas components and heavy gas components. Their model showed high calculation precision and predicted yields that agreed well with the experimental values.

### **2.9.3 Structured Kinetics with Chemical Information**

The link between kinetics and chemical structure information was developed for cracking of bitumens and heavy oils. Both sulfide content and aromatic content are expected to have impacts on first-order rate of cracking. Rahmani et al. (2003) proposed cracking kinetics of asphaltene as a function of chemical structure. The cracking kinetics of the asphaltenes was consistent with a modified kinetic model for coke formation, phase separation and hydrogen transfer. First-order rate constant of asphaltene cracking and stoichiometric coefficient were found to linearly correlate with sulfide content and aromaticity of feed, respectively. This model incorporating sulfide concentration and aromaticity successfully predicted cracking of other asphaltenes. Nevertheless, asphaltenes are structurally different from gas oils, which may result in discrepancies in kinetics. Instead of asphaltenes, Gray et al. (1991) explored the

relationship between chemical structure and reactivity of bitumens by catalytic hydrocracking of residue feed (424 °C+) in a CSTR at 430 °C. They found the first-order rate constant for residue conversion increased linearly with both fraction of C-C bond broken and concentration of carbon bound to aromatic rings. They also claimed that the residue conversion should be independent of feed molar mass given that the decomposition was dominated by the loss of side chains and groups. The experiments and correlations indicated that hydroconversion of residue goes through preferential loss of aliphatic side groups in feed and produces less aromatic distillate products, leaving behind more aromatic residue oil. This mechanism can also be expected in pure thermal cracking reaction due to its dominant effect in hydro-conversion. The residue used in this study featured the same chemical trend as bitumen derived HGO, with only difference in cutpoint. As a consequence, their cracking kinetics with chemical structure is expected to be also similar. Nagaishi et al. (1997) cracked bitumen in a continuous-flow stirred reactor with and without catalyst by multiple-pass operation. They discovered that the apparent first-order rate constants for cracking of residue decreased with increasing conversion both with and without catalyst. It indicated loss of feed reactivity with increasing conversion. This was attributed to the removal of easily reacted structures, such as sulfides, in the course of reaction, leaving unreactive aromatics. They also successfully correlated the decreasing rate constants with the fraction of aromatic carbon in the feed. Although bitumen was used as feed in this study, the feed at final pass were very close to HGOs. Therefore, similar structured kinetics with chemical information is expected to exist in cracking of bitumen derived HGOs. This was verified by Dupain et al. (2003) who cracked aromatic gas oil (aromatic content: 33.3 wt%) under realistic fluid catalytic cracking conditions. They remarked that

conversion of an aromatic feed by cracking reactions was limited to the paraffinic fraction and the alkyl groups associated to the benzene ring in aromatic compounds. The uncrackable polycyclic aromatics would stay in the feed fraction or end up in lighter fractions. Some portion of them was converted to coke. A first-order kinetic model was proposed to describe the crackability of the feed, using a correction parameter to compensate for the refractory aromatics. Long side chains were also claimed to be more reactive than short ones in this research. Some studies developed the second-order kinetics on the basis of chemical structure. Danial-Fortain et al. (2010) studied the reactivity of Athabasca vacuum residue in hydroconversion and pointed out that the conversion followed apparent second-order kinetics as several parallel first-order reactions occurred. Ho and Aris (1987) suggested that apparent second-order reactions could arise if the reacting lump contained unreactive species. Gauthier et al. (2007) studied hydroconversion of residue in two serial ebullated-bed reactors. Conversion was noted to be lower in the second reactor than the first one and the first-order rate constant was confirmed to decrease with increasing conversion as depletion of reactive species. They concluded that hydroconversion of residue could be represented by a second-order kinetics in order to describe the complete conversion range with the same rate constant. These arguments are based on fitting experimental data and lack in theoretical evidence. According to free-radical mechanism, most thermal reactions of interest exhibit apparent overall first-order kinetics, even though the steps are a mixture of first and second-order reactions. The actual conversion of reactive materials still follows first-order kinetics with unreactive species behaves as inert. The analytical chemical information was incorporated in lumped kinetic models by grouping similar types of molecules together. Weekman (1979) distinguished feedstock components as

aromatic rings, paraffinic chains and alkyl chains of aromatics. Isabelle et al. (1994) cracked different sources of vacuum gas oil in a plug flow reactor with catalyst at 530 °C and proposed a kinetic model based on molecular description. The lumps were defined by boiling range first and each cut was divided into paraffinic, naphthenic, olefinic and aromatic lumps by quantitative analysis. This model predicted the experimental results well and showed the importance of the condensation and hydrogen transfer reactions for coke formation and gasoline quality. Gross et al. (1976) invented a kinetic model to simulate catalytic cracking on heavy fuel oil (HFO, 343 °C+). The reactant and product species were lumped into paraffins, naphthenes as well as separate aromatic rings and aromatic substituent groups. The cracking rates of paraffins and naphthenes were found to increase with increasing molecular weight. The comparison of model predicted product yields with observed results suggests that the side chains on aromatic rings cracked very easily while aromatic rings were extremely resistant to cracking reactions. The HFO was determined to be almost solely composed of polynuclear aromatic rings at conversion of 60-70 wt%.

## **2.10 Summary of Key Issues**

There are a limited number of previous researches focused on the high temperature thermal cracking of HGO in vapor phase. Most of the researches were focused on introducing gas oil as an alternative feed for steam crackers and fluid catalytic crackers. The effect of operating conditions on product (especially gases) distribution and yield was investigated and both simple and lumped kinetic models were developed to predict product yields. However, none of these studies have attempted to correlate kinetics and chemical information for thermal cracking of HGO.

Bitumen-derived HGO has totally different chemical structure and processing pathway from conventional gas oil. It features much higher aromatic carbon content and lower hydrogen content. As a consequence, the kinetics of thermal cracking might also differ. However, no studies have been found to examine thermal cracking of highly aromatic-naphthenic gas oil from coking of bitumen, nor did they study the quality of the liquid products, The link between reaction kinetics and liquid product quality was also not established before.

# CHAPTER 3

## Experimental Materials and Method

### 3.1 Materials

The feed material was bitumen derived HGO from fluid coking, supplied by Syncrude Canada Ltd. The properties of the feed are listed in Table 3-1. This sample was the bottom stream from the coker fractionator. The origin of the feed suggests that its quality was poor compared with conventional HGO, which was validated by its density and elemental compositions. The processing history of the feed also implies that some possible variations of chemical structure might occur. Compared with its precursor bitumen, the density of our HGO did not shift a lot, while the hydrogen content (9.6 wt%) was even lower and aromatic carbon content (0.405) was even higher. For instance, Athabasca bitumen has hydrogen content of 10.6 and aromatic carbon content of 0.316 (Gray, 2010). However, the boiling range shifted down from over 50 % fractions above 524 °C for unprocessed bitumen to about 80 % material in 343-524 °C for derived HGO.

Table 3-1. Properties of heavy gas oil feed material

| <b>Property</b>                      | <b>Value</b> |
|--------------------------------------|--------------|
| Density, kg/m <sup>3</sup> @ 15.6 °C | 1.013        |
| Viscosity, mPa.s @ 15.6 °C           | 14681        |
| Elemental analysis                   |              |
| Carbon, wt%                          | 85.2         |
| Hydrogen, wt%                        | 9.6          |
| Sulfur, wt%                          | 4.3          |
| Nitrogen, wppm                       | 7270         |
| H/C atomic ratio                     | 1.36         |
| Aromatic carbon content              | 0.405        |
| Boiling fractions, wt%               |              |
| 343 °C-                              | 4            |
| 343-524 °C                           | 79           |
| 524 °C+                              | 17           |

Methylene chloride (99.9 %) and toluene (99.9%) were purchased from Fisher Scientific, Ottawa and used as received. Compressed gas helium (Ultra high purity 5.0), air (extra dry) and liquid nitrogen was provided by PRAXAIR, Edmonton. GC calibration gases C<sub>1</sub>-C<sub>2</sub> and C<sub>1</sub>-C<sub>6</sub> were synthesized by PRAXAIR, Edmonton. Methane calibration gas was customized by MESA, Santa Ana. The composition of calibration gases is exhibited in Table 3-2. Glass wool was supplied by Fisher Scientific, Ottawa.

Table 3-2. Composition of GC calibration gases

| Composition                                    | Concentration | Composition             | Concentration |
|--|---------------|-------------------------|---------------|
| C <sub>1</sub> -C <sub>2</sub> calibration gas | ppm           | Methane calibration gas | ppm           |
| C <sub>2</sub> H <sub>6</sub>                  | 10.4          | Methane                 | 100           |
| C <sub>2</sub> H <sub>4</sub>                  | 9.95          | Nitrogen                | Balance       |
| CH <sub>4</sub>                                | 10.3          |                         |               |
| Helium   | Balance       |                         |               |
| C <sub>1</sub> -C <sub>6</sub> calibration gas | Molar %       |                         | Molar %       |
| Pentene  | 0.100         | Hexane                  | 0.100         |
| Isohexene                                      | 0.100         | Isobutane               | 2.02          |
| Acetylene                                      | 0.999         | Isopentane              | 0.500         |
| Argon  | 1.00          | Methane                 | 15.0          |
| Butane   | 2.51          | Nitrogen                | 4.00          |
| Carbon dioxide                                 | 3.00          | n-pentane               | 0.503         |
| Carbon monoxide                                | 2.00          | Propane                 | 8.01          |
| cis-2-Butene                                   | 0.998         | Propylene               | 3.01          |
| cis-2-Pentene                                  | 0.0988        | trans-2-Pentene         | 0.100         |
| Ethane   | 6.97          | Hydrogen                | Balance       |
| Ethylene                                       | 7.47          |                         |               |

## 3.2 Reactor Apparatus and Operation

### 3.2.1 Reactor Apparatus

A simplified diagram of the reactor apparatus is illustrated in Figure 3-1. The basic design of the reactor followed Vafi (2012) except for the nozzle and feed preparation. The reactor apparatus was comprised of three primary parts: feed introduction, reaction and product collection and two auxiliary sections: data acquisition and helium gas flow control.

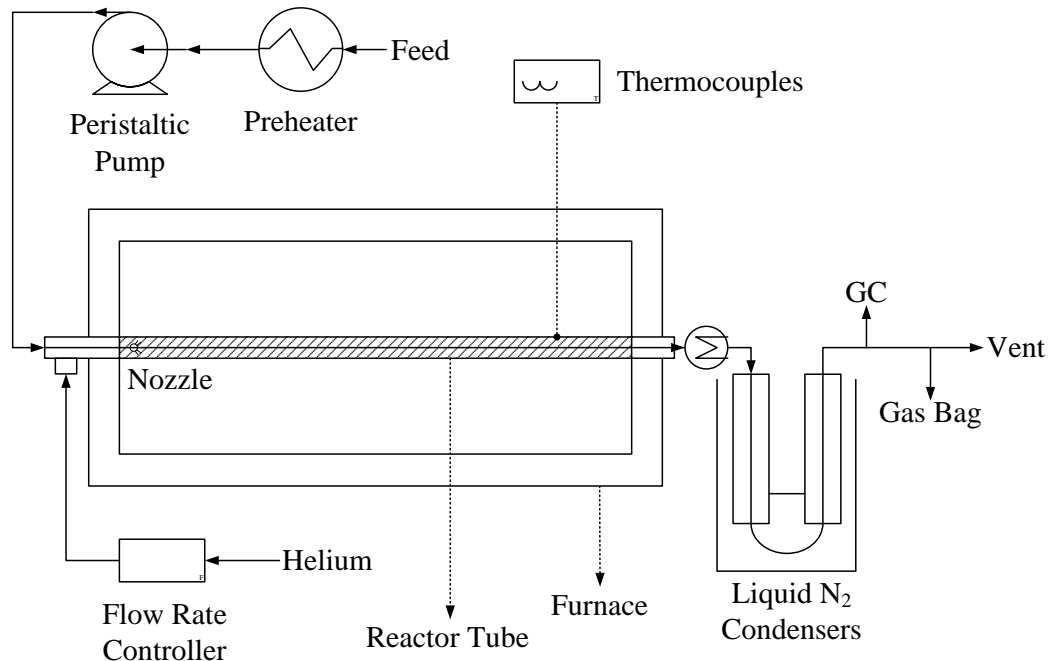


Figure 3-1. Simplified diagram of reactor apparatus

### 3.2.1.1 Feed Introduction

The feed HGO was added to a 50mL graduated cylinder which was immersed in a beaker filled with water, to serve as a water bath. They were placed on the heating plate to preheat the feed to the desired temperature, circa 80 °C. The inlet tube from a peristaltic pump (MasterFlex L/S 07523-80, Cole-Parmer, Montreal) directed into the graduated cylinder and submerged in the feed. The outlet of the pump was connected to a nozzle tube. The peristaltic pump provided precise and repeatable flow control with flow rate capacities from 0.001 mL/min to 3400 mL/min. The fluid only contacted the tubing, avoiding contamination to feed. The pump tubing (0.762 mm inner diameter and length from 70-91 cm FDA Viton Tubing HV-96412-13, Cole-Parmer, Montreal) were replaceable. Another two heating plates were set up along the pump tubing line to maintain the temperature above 40 °C. In this situation, the viscosity of feed was

reduced significantly, which ensured good fluidity until it was vaporized. One thermocouple (K-type stainless steel sheath with 1.59 mm outer diameter, Omega, Laval) was used to measure the water bath temperature; the other two were attached to measure temperatures at different positions along the pump tubing.

The nozzle was fabricated from two Swagelok 316/316L seamless tubes (1.59 mm outer diameter and 0.508 mm nominal wall thickness) joined by Swagelok fittings with total length of 35.6 cm. It was inserted into the reactor tube with tip position 2.7-3.4 cm distance from the inner wall of the furnace.

### **3.2.1.2 Reaction Section**

The tubular reactor consisted of a piece of Swagelok 316/316 L seamless tube (12.7 mm outer diameter and 1.24 mm nominal wall thickness) with effective reaction length of 0.915 m. The reactor tube was laid on the central axis of a split horizontal furnace (DT-22-HTOS-3Z-36 (12)-W6401, DelTech, Denver). Insulation materials were used to fill the gap between reactor tube and furnace at each end to minimize heat loss. The furnace was well insulated and provided an isothermal environment. The three heating elements of furnace could be controlled separately by a controller with maximum temperature of 1200 °C. Three temperature set points, 600 °C, 650 °C and 700 °C, were used for experiments. The feed stream was sprayed at the nozzle tip inside of reactor tube and completely vaporized. The helium stream was passed into the reactor at the inlet to carry the feed vapor through the reactor tube. The reaction occurred in a highly diluted condition given that the feed stream accounted for less than 3 vol% of the whole stream. The furnace rapidly heated up the mixture of helium gas and reactant and maintained the temperature along the reactor tube. As a result, there is a non-

isothermal part at the beginning of reactor, and its length varied with different helium flow rates. Six thermocouples were fixed on the body of reactor tube at different positions to measure the temperature profile. The first one was at the location of the nozzle tip. The reactor tube exposed outside of furnace at downstream end of the furnace was wrapped with heating tape to avoid condensation of product vapor.

### **3.2.1.3 Product Collection**

The downstream section of the apparatus consisted of two groups of U tube condensers in parallel, with two in series for each group. They were constructed with several Swagelok 316/316 L seamless tubes (25.4 mm outer diameter and 2.11 mm nominal wall thickness) and Swagelok fittings, which were connected by Swagelok hoses. Liquid products were collected in these tubes and hoses by submersing the condensers in liquid nitrogen. A thermocouple was inserted into one of the condensers to measure the cryogenic temperature. The outlets of two last condensers were filled with glass wool to capture any coke particles and liquid aerosol. A pressure transmitter (S-10, WIKA, Edmonton) was connected at the downstream to measure pressure inside of condensers. There were three outlets at the downstream. Condensable gases (helium diluted) were collected in gas sample bags (3 Liters, SKC, Pittsburgh) connected to one of the outlets by opening a Swagelok ball valve. Non-condensable gases (helium diluted) were directed to a gas chromatograph (5890A Series II, HEWLETT PACKARD, Wilmington) for analysis. The remaining gases passed through volumetric flow meter (DTM-200A, American Meter Company, Nebraska City) to a vent.

#### **3.2.1.4 Data Acquisition System**

A computer installed with LabVIEW software was set up to control and detect the operating conditions of reactor system. Two mass flow controllers (UFC-1200 A, UNIT, Yorba Linda) could be adjusted by the software to change helium flow rate. The temperatures measured by thermocouples and pressures measured by pressure transmitter were also recorded.

#### **3.2.1.5 Helium Gas Flow Control**

The helium sweep gas was supplied from two groups of helium gas cylinders. Each group contained two cylinders in case one of them was consumed. Two mass flow controllers (MFC-5 and MFC-2) were applied to measure and control the flow of each stream. The voltage signals of both MFC-5 and MFC-2 controllers ranged from 0 to 5 V and the calibration curves are given in Figure 3-2. Both streams were purified by two rechargeable gas purifiers (RGP-250-500B, OXICLEAR, Oakland) to remove residual traces of oxygen.

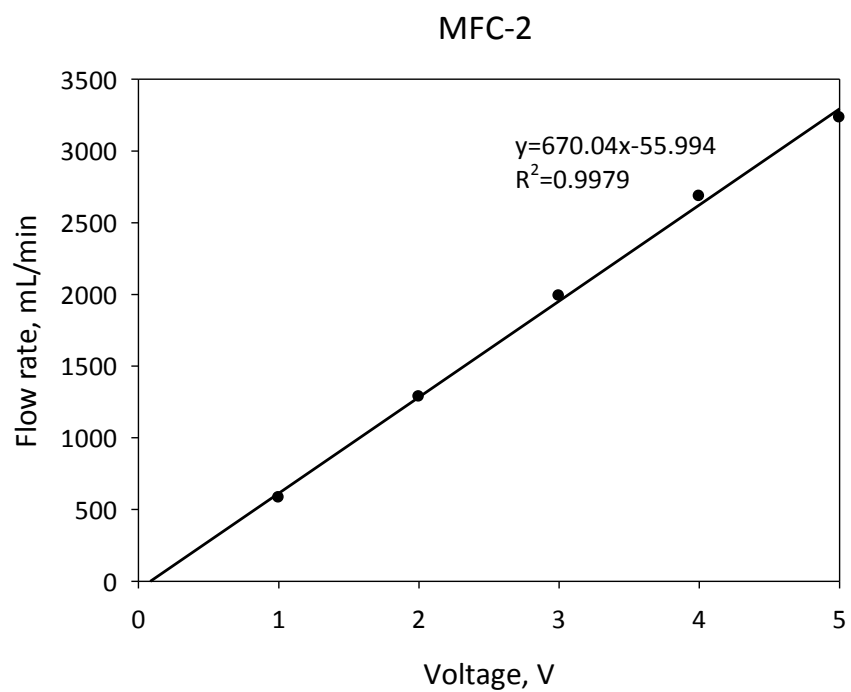
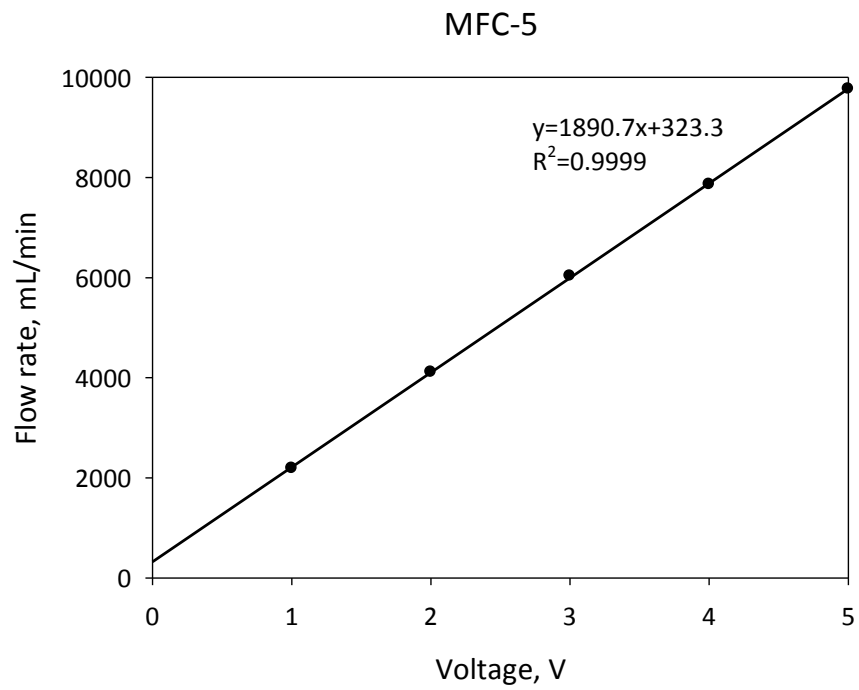


Figure 3-2. Calibration curves of mass flow controllers

### 3.2.2 Reactor Feed Optimization

In vapor phase cracking, the key performance of the reactor system was the complete vaporization of feed at the end of the nozzle tube. The internal configuration of reactor inlet is shown in Figure 3-3. Four steps of heat transfer occurred in the reactor system.

1. Furnace heated the reactor tube outer wall by radiation
2. Heat transferred through tube by conduction
3. Reactor tube inner wall heated helium sweep gas by convection
4. Helium sweep gas provided heat capacity and heat of vaporization to feed by convection

In all the steps, heat transfer between tube inner wall and helium sweep gas was the controlling step due to the high heat capacity of helium. The nozzle tube position and helium flow rate were the two main factors that determined the mean flow temperature at nozzle tip. In general, long feed tube inside of the reactor and low helium flow rate favor vaporization of feed at the tip. However, significant reactions may occur prior to the nozzle tip if the feed tube is too long in the high temperature environment.

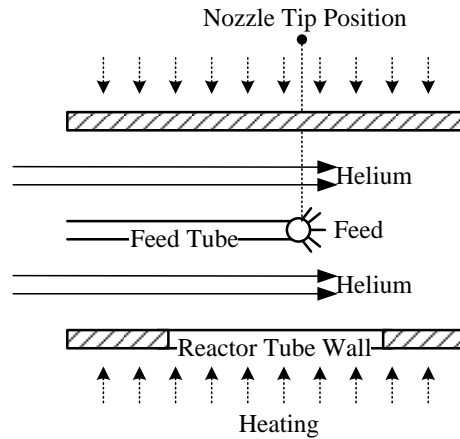


Figure 3-3. Schematic of reactor inlet

In order to determine feasible operating range, vaporization tests were carried out to find the appropriate positions for the nozzle tube and flow rates of helium carrier gas. A thermocouple was also inserted into the reactor tube to directly measure the flow temperature at specific position and flow rate. During the vaporization test, the feed was injected and reacted for 30 minutes at a specific nozzle tip position with different helium flow rates and temperatures. Products were stored in the condensers without recovery. At the end of each run, the nozzle was disconnected from the reactor tube to observe if there was any feed or coke deposition at the inlet. At a nozzle tip position 2.7-3.4 cm from furnace inner wall, nearly full vaporization of feed was achieved within specific ranges of helium flow rates that give reasonable conversions (10-90 %) at temperatures of 600 °C, 650 °C and 700 °C. Meanwhile, no coke deposition was found inside of feed tube. The feed would flow through the tube as a gas-liquid mixture, prior to complete vaporized. The size of bubbles would be very similar in dimension to the feed tube given its small diameter (0.572 mm ID). Therefore, the most likely flow

pattern inside the feed tube was slug flow where the bubbles were separated from one another by slugs of liquids (Figure 3-4).

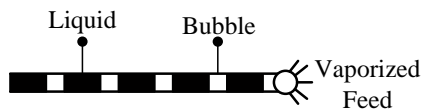


Figure 3-4. Slug flow pattern inside of nozzle tube

In this case, the feed flow rate was very high on a volumetric basis and the residence time was accordingly quite low. Consequently, thermal reactions inside of feed tube were considered to be negligible. The operating boundaries are tabulated in Table 3-3.

Table 3-3. Allowable operating conditions and nozzle tip position

| Temperature, °C | Helium flow rate range, mL/min | Nozzle tip position, cm |
|-----------------|--------------------------------|-------------------------|
| 600             | 1284-2684                      | 2.7                     |
| 650             | 1284-4114                      | 2.7-3.4                 |
| 700             | 1284-6035                      | 2.7                     |

Over this temperature range, there was a minimum helium flow rate. Below this limit, too much coke deposited at the end of reactor tube. At 600 °C, the maximum helium flow rate was given by conversion limit. Above this point, conversion would be less than 10 %. At 650 °C and 700 °C, the maximum helium flow rates were determined by the complete vaporization limit. At a temperature of 650 °C, the nozzle tip position was extended to 3.4 cm in order to obtain enough helium flow rate range.

### **3.2.3 Reactor Operation**

#### **3.2.3.1 Reactor Preparation**

Glass wool was used to fill up the outlets of two downstream U-tube condensers. All four condensers were connected together and with reactor tube by metal hoses. A thermocouple was inserted and fixed into one of the upstream condensers and then connected with data acquisition system. Two helium purge gas lines were also connected with condensers. All condensers were placed into two liquid nitrogen traps. The reactor tube was adjusted to be at the desired position relative to the furnace wall. Heating tapes from two variable transformers were wrapped around the end of reactor tube and another thermal couple was fixed to measure the temperature. A feed nozzle tube was inserted and connected with reactor tube by a Tee fitting. Helium sweep gas lines were connected to the other port of the fitting. The peristaltic pump was placed on the horizontal surface near the head of reactor. Clean pump tubing was loaded into pump head which was mounted on the pump drive. The pump tubing outlet was connected with nozzle tube inlet. A heating plate was also mounted on the surface with a beaker filled with water placed on. A thermal couple was immersed in the water to measure its temperature. Another two heating plates and thermocouples were also set up along the pump tubing line.

#### **3.2.3.2 Condenser Leak Test**

A leak test was carried out to inspect any installation problems of the condensers. Two valves at the upstream of the condensers and outlet valves at the downstream were closed to isolate the four condensers. The data acquisition system was turned on to record the internal pressure. Two helium purge gas valves were opened to fill all the

condensers until the pressure reached about 40 psig. The system was held for 1 hour and the final pressure was read. Soap bubble was also used to inspect any leakage during the test. If the overall pressure loss was more than 1 %, the connections of system needed to be tighten and another leak test had to be conducted until pressure loss was acceptable. After leak test, all valves were released to vent out helium in the condensers.

### **3.2.3.3 Operating Condition**

The elements of furnace were switched on and desired temperature and ramp rate were set by the controller. It took a few hours to heat up the furnace to the final temperature depending on the setpoint. The temperature profile of the reactor tube was recorded when the desired furnace temperature reached. Due to the thermal expansion, the reactor tube was readjusted to its original position. Mass flow controllers were turned on to set the flow rate of helium sweep gas throughout the reactor tube. The temperatures of reactor inlet dropped significantly at the beginning and then turned out to be stable. The new temperature profile was subsequently recorded. The valves at downstream to gas chromatography and gas sample bags were closed so that all helium flowed to the vent of system. Using volumetric flow meter at the vent and stop watch, the flow rates of helium sweep gas were measured for several times to get the average value. As a result, the operating temperature and residence time were defined. The operating conditions of 10 groups of experiments are listed in Table 3-4. The autotransformers controlling heating tapes were also switched on to keep the temperature at reactor tube outlet circa 300 °C.

Table 3-4. Operating conditions of all experiments

| Temperature, °C | Residence time, s | Nozzle tip position, cm |
|-----------------|-------------------|-------------------------|
| 600             | 0.682             | 2.7                     |
|                 | 0.752             | 2.7                     |
|                 | 1.166             | 2.7                     |
| 650             | 0.343             | 3.4                     |
|                 | 0.529             | 2.7                     |
|                 | 0.652             | 2.7                     |
|                 | 0.717             | 2.7                     |
| 700             | 0.326             | 2.7                     |
|                 | 0.612             | 2.7                     |
|                 | 0.663             | 2.7                     |

### 3.2.3.4 Operating Procedures

The bitumen derived HGO feed was weighted and loaded in the graduated cylinder which was inserted with a pump tube. Three heating plates were switched on to preheat the feed. The time dispense mode was selected to run the peristaltic pump. The spinning speed of pump head was set as 5 RPM which corresponded to 0.23 mL/min. The pump dispense time was fixed at 30 minutes. Two traps holding all U-tube condensers were filled up with liquid nitrogen. The temperature was reduced dramatically to -170 °C. The valve at downstream to GC was tuned to the point that the flow rate of helium sweep gas to GC was about 20 mL/min. After final inspection on the system, the pump drive was started and feed injection began. The temperature at the first measuring point was reduced by the introduction of feed and became constant in about 5 minutes. The temperature profile of reactor tube and helium flow rate were monitored during the operation. More liquid nitrogen was supplied if the level in traps

were too low. When operation time reached 30 minutes, the pump drive stopped automatically. Furnace, autotransformers and heating plates were switched off. Mass flow controller was also set to be zero voltage, which shut down helium sweep gas. The valves at both upstream and downstream of condensers were closed immediately followed by transferring U-tube condensers out of liquid nitrogen traps. The products inside were soon warmed up and condensed gases evolved, which increased the pressure inside. The final temperature and pressure of condensers were recorded after complete warm-up. When the furnace cooled down, the nozzle was disconnected and the pump tube was also disassembled from the drive. The approximate amount of feed remaining in the nozzle and pump tubing was estimated by direct measurement and calculation. The feed graduated cylinder was displaced out of water beaker and dried before weighing again. The actual amount of feed reacted was:

$$m_{\text{reacted}} = m_{\text{initial feed}} - m_{\text{final feed}} - m_{\text{nozzle}} - m_{\text{pump tubing}} \quad (3.1)$$

Where  $m_{\text{initial feed}}$  and  $m_{\text{final feed}}$  were mass of initial and final feed in the graduated cylinder, respectively.  $m_{\text{nozzle}}$  was the mass of feed staying in the nozzle tube and  $m_{\text{pump tubing}}$  was the mass of feed left in the pump tubing.

After weighing, the nozzle and pump tubing were cleaned up by toluene for further use. The reactor tube was also checked by endoscope (TITAN, Plymouth) to observe if there was any feed or coke deposition at the inlet.

A 3-liter gas sample bag was used to collect the condensed gas products that evolved in the condensers by opening gas collection valve. The condenser pressure was reduced to atmospheric pressure while the temperature remained constant. The condensed gases

continue to evolve from liquids when the condensers were exhausted. Thereby, the condensers were purged with helium to the initial pressure and the gases were collected again in a new gas sample bag. This was repeated for at least three times until the evolved gases were highly diluted in helium that could not be detected by GC.

U-tube condensers as well as connecting metal hoses were disassembled from the reactor tube. The inside of the reactor tube at the outlet was observed by using an endoscope and the settled coke particles were collected. Methylene chloride was used to wash the condensers and hoses several times to collect all the liquid products and solid coke. The collected liquids were filtered under vacuum by filter paper with 0.22  $\mu\text{m}$  pore size to separate coke particles. The coke product was dried overnight for measuring weight. BUCHI Rotavapor R-215 together with V-700 vacuum pump and V-850 vacuum controller was used to separate solvent with liquid products. BUCHI B-491 heating bath was filled with deionized water to heat evaporating flask with volume of 500 mL. Cooling water circulated through the condenser at flow rate between 40 and 50 L/h. The receiving flask had a volume of 1000 mL where all the solvent was collected. In separating the methylene chloride, the maximum rotation speed of evaporating flask was 120 RPM. The water bath temperature was constant at 65 °C and vacuum pressure was reduced gradually from 1 atm to 300 mbar. The whole separation process was held for at least 2 hours. During the separation, all the light liquid escaped with the solvent, leaving behind condensed heavy liquid. The collected solvent with light liquid was stored for GC analysis. The mass of heavy liquid product was measured until no solvent was trapped.

### **3.3 Analysis of Reactor Samples**

#### **3.3.1 Fixed and Condensed Gas Analysis**

##### **3.3.1.1 Gas Chromatography Apparatus**

A HEWLETT PACKARD 5890A Series II GC with ChemStation software was employed to analyze fixed and condensed gas products qualitatively and quantitatively. Four PRAXAIR gas cylinders: extra dry compressed air, helium, hydrogen and make-up helium of ultrahigh purity 5.0 were delivered at pressures of 40 psig, 40 psig, 40 psig and 60 psig to GC, respectively. The instrument had two sample injection systems: split injection port and six-port switching valve. The inlet temperature was 250 °C. Condensed gas products were collected in gas sample bags and were injected by an Agilent syringe with volume of 50  $\mu$ L through split injection into column. Fixed gases were collected in a 1 mL sample loop and carried into column upon switching the valve. The GC was installed an Agilent GC capillary column with length of 30 meters and inner diameter of 0.530 mm. It featured alumina stationary phase, which was excellent for light hydrocarbon (C1-C8) analysis. Helium was used as carrier gas throughout the column. Flame ionization detector (FID) was used for sample analysis. It is very effective to detect hydrocarbon components, while not sensitive to the molecular structure. The FID was operated at 220 °C with hydrogen as fuel, compressed air as oxidant and helium as make-up gas. The temperature program of oven is shown in Table 3-5. The total analysis time was 16 minutes.

Table 3-5. Oven temperature profile during analysis

|                | Temperature change        | Hold time |
|----------------|---------------------------|-----------|
| <b>Initial</b> | 75 °C                     | 1.00 min  |
| <b>Ramp 1</b>  | 75 – 95 °C @ 5.0 °C/min   | 0 min     |
| <b>Ramp 2</b>  | 95 – 200 °C @ 30.0 °C/min | 11.00 min |

### 3.3.1.2 Gas Chromatography Calibration

The gas chromatography was powered on and ChemStation was started up. Hydrogen, air and helium gases were used to feed GC. Another stream of auxiliary helium gas was also introduced. The flame-ionization detector was then ignited with hydrogen fuel. The method in ChemStation was loaded to ramp the oven, column and detector temperatures to set points. When the GC was ready, the C<sub>1</sub>-C<sub>2</sub> and pure methane external standards were passed through GC, respectively. The soap bubble flow meter was used to check the flow rates of standard gases. Six-port switching valve was turned to introduce 1 mL calibration gas samples for analysis. Calibration peaks for C<sub>1</sub>-C<sub>2</sub> and methane were obtained after several repeated analysis. The switching valve was then turned back. A 1-liter gas sample bag was used to collect C<sub>1</sub>-C<sub>6</sub> calibration gas in the cylinder and then was injected by 50 µL Agilent syringe through split injection port into GC for analysis. All calibration peaks for C<sub>1</sub>-C<sub>6</sub> were subsequently obtained in about 16 minutes. The peaks were then designated in accordance with the sequence showing in column library and the response factor of each component was calculated by its integrated peak area and known concentration.

### **3.3.1.3 Gas Chromatography Analysis Procedure**

Fixed gas products were formed during the operation of the reactor lasing for 30 minutes. The manual notch on GC was turned to analyze the fixed gas products every 5 minutes in the course of reaction. The concentration of each component in the fixed gases was averaged to calculate the total amount.

Condensed gas products evolved after the operation and were collected in gas sample bags. A 50  $\mu\text{L}$  Agilent syringe was used to inject collected gases through split injection port into GC for analysis. The total amount of condensed gas products could be quantified by interpreting the corresponding peaks.

### **3.3.2 Liquid Product Analysis**

#### **3.3.2.1 Simulated Distillation**

##### **3.3.2.1.1 Simulated Distillation Apparatus**

Two GCs combined with Galaxie software were employed to determine boiling point distribution of samples: Bruker 450-GC based on ASTM D2887 and VARIAN 450-GC based on ASTM D6352. The boiling distribution results were then compared. The first one was operated at low temperature mode while the latter ran at high temperature. All supply gases helium, hydrogen, air and coolant carbon dioxide were provided by PRAXAIR. The sample injection method for both instruments was by autosampler. Bruker 450-GC had a RESTEK MXT-1HT SimDist column with length of 10.00 m, inner diameter of 0.53 mm and film thickness of 1.00  $\mu\text{m}$ . VARIAN 450-GC was equipped with a VARIAN CP-SimDist capillary column having length of 5.00 m, inner diameter of 0.53mm and film thickness of 0.09  $\mu\text{m}$ . Helium (PRAXAIR ultrahigh purity 5.0) was used as carrier gas in the column. Both GCs used FID as detectors supplied by combustion

hydrogen, compressed air and make-up helium. Carbon dioxide (PRAXAIR Bone air 3.0) was used to cool down columns for both instruments. The operating conditions are listed in Table 3-6.

Table 3-6. Operating conditions for Bruker 450-GC and VARIAN 450-GC

| <b>Conditions</b>                              | <b>Bruker 450-GC</b>  | <b>VARIAN 450-GC</b>   |
|--|---|--|
| Sample inject volume, $\mu\text{L}$            | 5.0   | 3.5  |
| Helium carrier gas pressure, psig              | 65  | 80   |
| Hydrogen combustion gas pressure, psig         | 80  | 40   |
| Compressed air pressure, psig                  | 85  | 80   |
| Helium carrier gas flow rate, mL/min           | 10.0  | 19.0   |
| Combustion hydrogen flow rate, mL/min          | 30  | 30   |
| Combustion air flow rate, mL/min               | 300   | 300  |
| Make-up helium flow rate, mL/min               | 30  | 0  |
| Detector temperature, $^{\circ}\text{C}$       | 380   | 430  |
| Inject temperature profile                     |   |  |
| Initial inject temperature, $^{\circ}\text{C}$ | 35  | 100  |
| Inject temperature ramp                        | 35-380 $^{\circ}\text{C}$ @<br>40.0 $^{\circ}\text{C}/\text{min}$ | 100-430 $^{\circ}\text{C}$ @<br>15.0 $^{\circ}\text{C}/\text{min}$ |
| Hold time, min                                 | 10  | 22   |
| Total time, min                                | 18.63   | 44.00  |
| Oven temperature profile                       |   |  |
| Initial oven temperature, $^{\circ}\text{C}$   | 10  | 40   |
| Hold time, min                                 | 1.50  | 0  |
| Oven temperature ramp                          | 10-380 $^{\circ}\text{C}$ @<br>15.0 $^{\circ}\text{C}/\text{min}$ | 40-430 $^{\circ}\text{C}$ @<br>10.0 $^{\circ}\text{C}/\text{min}$  |
| Hold time, min                                 | 23.83   | 5.00   |
| Total time, min                                | 50.00   | 44.00  |

### 3.3.2.1.2 Simulated Distillation Analysis Procedure

For ASTM D2887 method, a baseline blank GC analysis was performed by injection of pure carbon disulfide (Fisher Scientific, Ottawa). Due to the chromatographic baseline ramp in analysis, the area slice should be corrected for baseline offset, by subtracting the corresponding area slice in a recorded blank analysis. A calibration mixture (SUPELCO Analytical ASTM D2887 Quantitative Calibration Solution) from n-C<sub>5</sub> to n-C<sub>44</sub> was injected to obtain retention time versus boiling point calibration curve. The calibration table was prepared by designating each peak of standard mixture with known boiling point. The Reference Gas Oil No.1 Sample (SUPELCO Analytical) was then injected and analyzed to verify the method. The boiling point distribution results were subsequently compared with standard values. If the difference was in allowable range, unknown samples would be run; otherwise, the method had to be corrected. Unknown samples for analysis were prepared by dissolving analyte in carbon disulfide solution with mass ratio about 1:10. This was accomplished by adding 0.15-0.20 g analyte with carbon disulfide to make a 1.5-2.0 g solution in vials. All sealed vials were then placed in the autosampler for analysis following specific sequence protocol. The boiling point distributions of samples were determined by integrating peaks in Galaxie software.

For ASTM D6352 method, a baseline blank test was conducted by injection of circa 2.0 g pure carbon disulfide (Fisher Scientific). Calibration mixture was prepared by adding 4 µL C<sub>5</sub>-C<sub>20</sub> n-alkane mixture with 20 mg C<sub>20</sub>-C<sub>120</sub> polywax 655 (SUPELCO Analytical) into a vial. The vial was capped and put on the heating plate at temperature of 110 °C for about 1 hour to make a homogenous mixture. The customized calibration mixture was then injected and analyzed to obtain calibration curve. The reference oil sample was prepared by dissolving ASTM D6352/D7169 reference material (SUPELCO Analytical) in

carbon disulfide solution with mass ratio about 1:100. Approximately 20-25 mg reference material was diluted by carbon disulfide to make a 2.0 g solution in a vial. Unknown samples for analysis were prepared using the same method. All sealed vials were then placed in the autosampler for analysis following specific sequence protocol. The boiling point distributions of samples were determined by integrating peaks in Galaxie software.

### **3.3.2.2 Elemental Analysis**

#### **3.3.2.2.1 Elemental Analyzer**

Elemental analysis on HGO feed and liquid products was performed on CHNS vario MICRO CUBE elemental. The analysis instrument consisted of four functional units: mechanical sample insertion and O<sub>2</sub> dosing system, furnace area and reaction zone, separator and detector. Two supply gases helium (PRAXAIR ultra-high purity 5.0) and oxygen (PRAXAIR ultra-high purity 4.3) were fed to the analyzer and the gauge pressures were 20 psig and 40 psig, respectively. The flow rate of helium was 200 mL/min and of oxygen was 14 mL/min. The pressure in the instrument ranged from 1200 to 1250 mbar. A balance was used to transmit sample weight to computer operating software. In the mechanical sample insertion and O<sub>2</sub> dosing unit, all samples were held in series in the carousel on the top which had 120 positions. Each sample was transferred into a ball valve in sequence where the outside air was displaced. A furnace was employed to hold the combustion tube and reduction tube at a constant temperature, 1150 °C and 850 °C, respectively. In the combustion tube, the sample was burned with oxygen to form N<sub>2</sub>, NO<sub>x</sub>, CO<sub>2</sub>, H<sub>2</sub>O, SO<sub>2</sub> and SO<sub>3</sub> gases. Among them, NO<sub>x</sub> and SO<sub>3</sub> were reduced to N<sub>2</sub> and SO<sub>2</sub> in the reduction tube. The separator consisted of an adsorption column and a possible additional adsorption tube. The adsorption column physically adsorbed the

measuring components in the gas mixture and allowed a defined desorption of individual components by means of temperature level. An additional adsorption tube is inserted between the adsorption column and the thermal conductivity detector (TCD) in order to bind the remaining traces of H<sub>2</sub>O. The measuring components except N<sub>2</sub> was adsorbed in the adsorption column first and then desorbed with increasing temperature. The sequence of components entering the detector was: N<sub>2</sub>, CO<sub>2</sub>, H<sub>2</sub>O and SO<sub>2</sub>. The components were transported by the helium carrier gas into the TCD which consisted of measuring cell and reference cell. The measuring gas flow rate was 200 mL/min which was measured by MFC-TCD flow meter. The electrical measuring signal was digitized and integrated. The absolute element content of the sample was computed from the integral of the individual measuring peak and the calibration factor of this element.

#### **3.3.2.2 Elemental Analysis Procedure**

Elemental composition (carbon, hydrogen, nitrogen and sulfur) of HGO feed and liquid products were measured by elemental analyzer. The elemental operating software was started and new task was established. The carousel position was set to zero and all previous samples were removed. Five empty boat containers were folded and then placed in the first 5 spots in the carousel, which were analyzed as blanks. Approximately 2 mg sulfanilic acid was weighed and sealed in each boat container. Five such samples were prepared and loaded in the next 5 spots in the carousel. Two of them were analyzed as conditioning samples; the rest three were analyzed as daily factor samples. Same weights of liquid oil samples were prepared in capsule containers which were pressed to seal under oxygen purging at low flow rate. All these unknown liquid samples were loaded in the following spots in the carousel. Each liquid sample was analyzed for repeating five times. The best three results with least standard deviations were selected

and averaged. The weights of all samples were recorded automatically in the software. The corresponding names and methods were input manually. The method for blank runs was Blank without O<sub>2</sub> and for all other runs was 2mgChem80s. During operation, the nitrogen and carbon value should be lower than 100 and sulfur/hydrogen value smaller than 200; otherwise, more blanks have to be run. Elemental compositions of sulfanilic acid must have the same value in the daily factor sample runs.

### **3.3.2.3 <sup>13</sup>C NMR Analysis**

<sup>13</sup>C NMR quantitative analysis was performed by Varian INOVA 400 MHz NMR spectrometer in the Chemistry department to obtain aromatic carbon content of HGO feed and liquid products. Cr(AcAc)<sub>3</sub> solution with concentration of 0.2 ml/L was used as the relaxation reagent. Equal amount of analyte and solution were prepared to make total volume of 0.7 mL in the NMR sample tube.

### **3.3.3 Recovered Solvent Analysis**

Recovered methylene chloride solvent from rotary evaporator receiving flask was analyzed qualitatively by Agilent 7890A GC system to detect any trapped light liquid component. The injection was carried out by autosampler with injection volume of 1 µL and injection temperature of 200 °C. Helium, hydrogen and compressed air from PRAXAIR were fed to the instrument with delivering pressure at 85 psig, 85 psig and 40 psig, respectively. The GC was equipped with an Agilent HEWLETT PACKARD-PONA column having length of 50 m, inner diameter of 0.200 mm and film thickness of 0.50 µm. The flow rate of helium carrier gas in the column was 1.1 mL/min. FID was used as the detector running at 250 °C and the flow rates of combustion hydrogen, combustion air and make-up helium were 30 mL/min, 250 mL/min and 30 mL/min, respectively. The

GC oven was maintained at 35 °C during the sampling process, after which the oven temperature was programmed from 35 to 150 °C at a rate of 10 °C/min and held for 3.5 minutes. The total run time was 15 minutes. About 1.5 mL solvent was prepared in a vial and placed on the autosampler for injection. A series of peaks presenting solvent and trapped light liquid were given by ChemStation during analysis.

# CHAPTER 4

## Results and Discussion

### 4.1 Performance of the Tubular Reactor

#### 4.1.1 Temperature Profile

The axial temperature profile of the flowing gas stream is an important attribute of the tubular reactor. The axial temperature distribution of reactor tube was measured by thermocouples at different positions. The results for ten experiments are presented in Table 4-1.

The data shows that temperature was lower than the furnace set point only at the inlet of the reactor, followed by sharp increase and then holding constant to the end. In order to calculate the axial temperature of the flowing gas stream, the axial temperature of reactor tube was assumed to be constant and equal to the average value of temperatures measured from the second point to the last one. Due to the axial temperature profile at the inlet, the first thermocouple measuring point was not included. There was no significant heat transfer resistance in the reactor tube wall given its high thermal conductivity. As a consequence, the heat conduction was very rapid, which was ignored in the calculation. In comparison, convection heat transfer between reactor surface and fluid inside was the controlling step and the fluid temperatures must continue to change with reactor length until they reached ultimate value.

Table 4-1. Axial temperature profile of reactor under various operating conditions

| Operation | Reactor position, cm |       |       |       |       |       | Furnace set point |
|-----------|----------------------|-------|-------|-------|-------|-------|-------------------|
|           | 2.7                  | 14.7  | 29.1  | 45.3  | 59.2  | 74.9  |                   |
| 600 Run1  | 523.2                | 607.0 | 609.1 | 609.2 | 608.1 | 610.5 | 600 °C            |
| 600 Run2  | 529.2                | 606.0 | 609.0 | 609.3 | 608.3 | 610.5 |                   |
| 600 Run3  | 550.4                | 606.5 | 609.2 | 608.5 | 606.5 | 608.2 |                   |
| 650 Run1  | 552.1                | 652.4 | 657.8 | 658.2 | 657.0 | 659.2 | 650 °C            |
| 650 Run2  | 575.8                | 653.5 | 657.2 | 657.7 | 656.9 | 659.2 |                   |
| 650 Run3  | 585.9                | 655.0 | 657.8 | 657.7 | 656.0 | 657.8 |                   |
| 650 Run4  | 589.7                | 655.0 | 657.7 | 657.7 | 656.4 | 658.5 |                   |
| 700 Run1  | 607.5                | 707.7 | 706.6 | 707.4 | 706.4 | 709.2 | 700 °C            |
| 700 Run2  | 640.9                | 703.2 | 706.7 | 707.2 | 706.4 | 708.7 |                   |
| 700 Run3  | 647.1                | 704.4 | 707.5 | 707.5 | 705.9 | 708.1 |                   |

Given Newton's law of cooling

$$q_s'' = h(T_s - T_m) \quad (4.1)$$

For a differential element of the tubular reactor in the axial direction  $x$

$$dq_{conv} = q_s'' \pi D dx = h(T_s - T_m) \pi D dx \quad (4.2)$$

And given an energy balance

$$dq_{conv} = \dot{m} C_p dT_m \quad (4.3)$$

These equations reduce to

$$\frac{dT_m}{dx} = \frac{\pi D}{\dot{m} C_p} h(T_s - T_m) \quad (4.4)$$

Boundary conditions

$$T_m(0) = T_{m,i} \quad (4.5)$$

$$T_m(L) = T_{m,o} \quad (4.6)$$

Integrating from the reactor inlet to the specific position

$$T_m(x) = T_s - (T_s - T_{m,i}) \exp\left(-\frac{\pi D \bar{h}}{\dot{m} C_p} x\right) \quad (4.7)$$

Where  $T_m(x)$  is the mean fluid temperature,  $T_s$  is the average axial surface temperature,  $T_{m,i}$  is the inlet fluid temperature,  $T_{m,o}$  is the outlet fluid temperature,  $x$  is the position of the reactor tube and  $D$  is the inner diameter,  $\bar{h}$  is the average heat transfer coefficient,  $\dot{m}$  is the mass flow rate of fluid and  $C_p$  is the heat capacity.

The fluid was entirely in the laminar region with calculated maximum Reynolds number of 43. Fully developed flow was assumed to encompass most of the tube, given the low values of  $Re_D$  and  $Pr$  value as well as the high  $L/D$  ratio in all operating conditions.

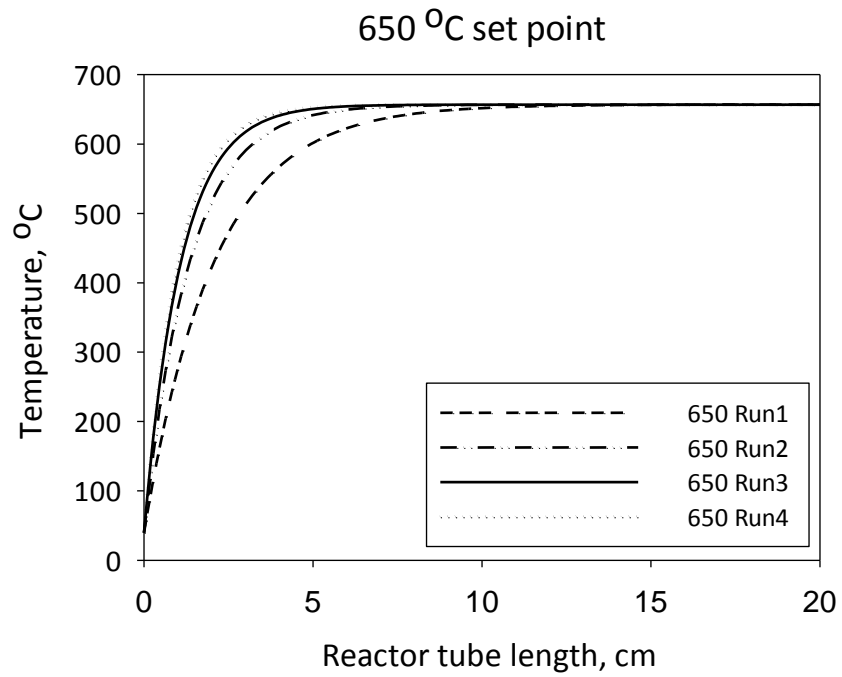
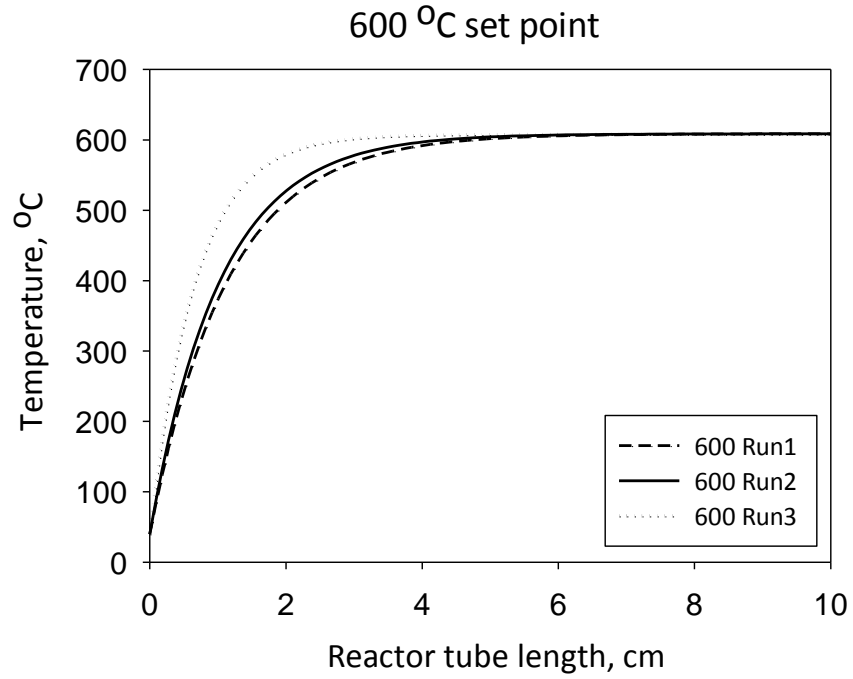
The fluid inlet temperature was estimated to be 40 °C and the outlet temperature was assumed to be equivalent to average axial surface temperature.

For constant surface temperature  $T_s$

$$Nu_D = \frac{\bar{h}D}{k} = 3.66 \quad (4.8)$$

Where  $k$  is the thermal conductivity of the flowing gas stream

Figure 4-1 shows the mean fluid temperature  $T_m(x)$  as a function of reactor tube length  $x$  at different operating conditions.



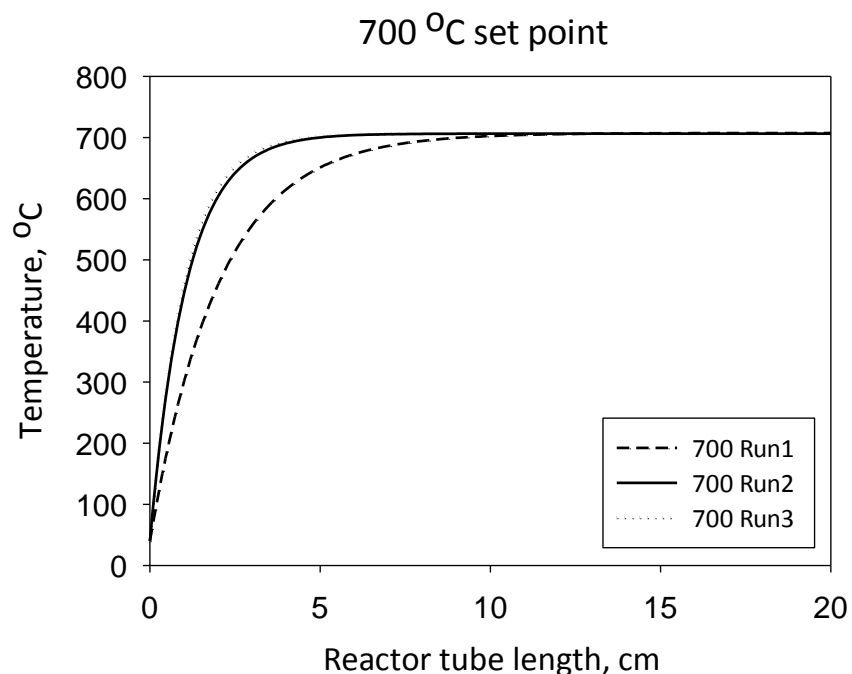


Figure 4-1. Axial temperature profiles of the flow gas stream at different operating conditions

The plotted results indicated that the lag in temperature between the fluid and the tube surface was small. For the maximum possible temperature difference, the fluid and the reactor tube reached the same temperature within 5 cm, except in the extreme flow cases of 650 Run1 and 700 Run1. Over the entire operating range, the reactor contents became isothermal at the set point within approximately 20 cm of entering the furnace. The heating entry length was defined as the distance required for the feed vapor with helium to reach within 5 °C of the average axial surface temperature of the reactor. The predicted heating entry length ranged from 0.4 to 7.2 cm at applied operating conditions, which accounted for maximum 8 % of total effective reactor length (defined as the length from nozzle tip to the outlet). This calculation is approximate in that the actual tube wall temperature changes due to the presence of the cold helium, as indicated by the data of Table 4-1. These results suggest that the temperature gradients

are comparable to Figure 4-1, but with a somewhat shallower slope so that a small temperature difference of 1-3 °C is detected at the 14 cm position. Given these measurements and the axial temperature estimates for the flowing gas phase, most of the reactor can be considered isothermal except a steep heating section at the inlet.

The calculated fluid temperatures at nozzle tip inside of reactor at different operating conditions are exhibited in Table 4-2. Vaporization of feed at nozzle tip was predicted by VMGSim v6.0 using the advanced Peng-Robinson equation of state. Boiling range and density were employed to characterize the feed. Under atmospheric pressure, 100 % of HGO was expected to be in the vapor phase within the nozzle tip temperature range. This prediction was consistent with our observation that the coke deposition was negligible at the reactor inlet after each run.

Table 4-2. Helium flow temperature at nozzle tip position

| <b>Operation</b> | <b>Temperature at nozzle tip, °C</b> | <b>Axial position of the nozzle, cm</b> |
|------------------|--------------------------------------|---|
| 600 Run1         | 556                                  | 2.7                                     |
| 600 Run2         | 568                                  | 2.7                                     |
| 600 Run3         | 598                                  | 2.7                                     |
| 650 Run1         | 538                                  | 3.4                                     |
| 650 Run2         | 574                                  | 2.7                                     |
| 650 Run3         | 605                                  | 2.7                                     |
| 650 Run4         | 617                                  | 2.7                                     |
| 700 Run1         | 532                                  | 2.7                                     |
| 700 Run2         | 653                                  | 2.7                                     |
| 700 Run3         | 663                                  | 2.7                                     |

#### 4.1.2 Reaction Residence Time

Another key operating condition of the flow reactor is the mean residence time of reactants. The feed was completely vaporized and carried throughout reactor tube by helium sweep gas. The residence times were determined by the volume flow rates of helium as well as reactant and product vapor. The mass flow rate of helium sweep gas was held constant by mass flow controllers in each run. However, according to the ideal gas law, the corresponding volume flow rate of helium increased with rising axial temperature in the reactor. Since temperatures increased very fast to the desired set points and held constant in the reactor, volume flow rates of helium were expected to be steady after passing the inlet portion of the reactor tube. The vaporized feed at the inlet may also impact the volume flow rate of the mixed helium and reactant flow. Furthermore, reactant and product usually do not have equal number of moles in gas-phase reactions. With regard to cracking, product is formed to give a larger number of moles. When this happened in our flow reactor, the volume flow rate increased gradually as the reaction proceeded. In order to investigate the influence of reactant and product vapor, flow rate distributions at nozzle tip position and reactor exit were predicted by VMGSim V-6.0. At the nozzle tip temperature, volume flow rate ratios of reactant and total flow were calculated based on known mass flow rates of helium and feed as well as density and boiling range of the feed. The reactant was finally reacted into liquid product, fixed and liquefied gases as well as coke. With exception to coke, the product stayed in the vapor phase through the reactor. Coke was not considered due to its extremely low yield. At the outlet temperature, the volume flow rates of helium, liquid product vapor, fixed and liquefied gases were calculated based on mass of recovered liquid and gases. The density and boiling range of liquid product were also

used as input for VMGSim. As a result, the volume flow rate ratios of product vapor and total flow were obtained at different conditions. The calculated results at both nozzle tip position and reactor exit are listed in Table 4-3.

Within operating helium flow range, the volume flow rates of reactant only accounted for 0.38-1.24 % of entire flow at inlet, which was negligible. This result was due to the operation of the pump at low displacement flow rate mode (0.230 mL/min). The volume flow rate percentages of product vapor out of total flow at outlet ranged from 0.76 % to 2.96 %. Due to significant loss of volatile liquid product in the process of recovery, the actual volume flow rates of liquid product vapor were expected to be 0-20 % higher, given mass recoveries from 80-100 %. Even considering this factor, the maximum possible volume flow rate of product vapor was only about 3 % of the total flow. Moreover, the average volume flow rate ratios of reactant/product and total flow should be intermediate between the inlet values and outlet values, which were much lower than 0.03. Consequently, the overall reaction occurred in a highly helium-diluted atmosphere.

Table 4-3. Flow rate distributions at reactor inlet and outlet

| <b>Operation</b>                        | 600  | 600  | 600  | 650   | 650  | 650  | 650  | 700   | 700  | 700  |
|---|------|------|------|-------|------|------|------|-------|------|------|
|   | Run1 | Run2 | Run3 | Run1  | Run2 | Run3 | Run4 | Run1  | Run2 | Run3 |
| <b>Inlet</b>                            |      |      |      |       |      |      |      |       |      |      |
| <b>Helium flow rate, mL/min</b>         | 6581 | 6110 | 4083 | 12038 | 8180 | 6901 | 6363 | 12134 | 7370 | 6939 |
| <b>Feed flow rate, mL/min</b>           | 50   | 49   | 51   | 47    | 49   | 51   | 52   | 47    | 54   | 56   |
| <b>Feed flow, vol %</b>                 | 0.75 | 0.80 | 1.24 | 0.39  | 0.59 | 0.74 | 0.81 | 0.38  | 0.73 | 0.79 |
| <b>Outlet</b>                           |      |      |      |       |      |      |      |       |      |      |
| <b>Helium flow rate, mL/min</b>         | 6994 | 6405 | 4128 | 13789 | 8976 | 7305 | 6651 | 14747 | 7793 | 7257 |
| <b>Product vapor, flow rate, mL/min</b> |      |      |      |       |      |      |      |       |      |      |
| <b>Heavy liquid</b>                     | 61   | 54   | 53   | 56    | 62   | 50   | 52   | 58    | 50   | 47   |
| <b>Fixed gas</b>                        | 5    | 6    | 7    | 13    | 20   | 23   | 21   | 43    | 58   | 52   |
| <b>Liquefied gas</b>                    | 15   | 14   | 19   | 37    | 56   | 49   | 54   | 101   | 129  | 123  |
| <b>Product flow, vol %</b>              | 1.14 | 1.14 | 1.89 | 0.76  | 1.52 | 1.65 | 1.88 | 1.35  | 2.94 | 2.96 |

Vapor volumes at the inlet and outlet were calculated based on axial flow temperatures at the nozzle tip position and reactor exist, respectively.

The residence time can be determined based on flow rate of helium sweep gas alone, as the residence time of helium flowing from the nozzle tip position to the exit of the reactor. Due to the temperature gradient along the reactor, the volume flow rate was different at each position in the entry length.

For a differential element

$$d\tau = \frac{dV}{v} \quad (4.9)$$

Using ideal gas law and assuming room temperature  $T_0$  constant at 24 °C

$$\frac{v}{v_0} = \frac{T_m}{T_0} \quad (4.10)$$

Integrated from 0 to  $\tau$

$$\tau = \frac{AT_0}{v_0} \int_{x_1}^{x_2} \frac{1}{T_m} dx \quad (4.11)$$

Where  $\tau$  is the residence time of reaction,  $A$  is the cross sectional area,  $v_0$  is the volume flow rate of helium at room temperature,  $T_m$  is the mean fluid temperature, and  $x$  is the reactor tube position.

Boundary conditions:

$x_1$ : Nozzle tip position (0.027 or 0.034 m)

$x_2$ : Reactor exit position (0.915 m)

The link between  $T_m$  and  $x$  is

$$T_m = T_s - (T_s - T_{m,i}) \exp\left(-\frac{\pi D \bar{h}}{m C_p} x\right) \quad (4.12)$$

The residence times of all ten groups of experiments were solved by MATLAB by Simpson integration method. The results were listed and compared with those estimated under isothermal assumption. In this case, the furnace set temperature and average axial surface temperature of reactor tube was used to predict residence time, respectively.

$$\tau = \frac{V}{v} = \frac{VT_0}{v_0 T_m} \quad (4.13)$$

As compared in the Table 4-4, the difference between actual and predicted values was very small with relative differences of less than 1 %. This result implies that the temperature ramp at the beginning of the reactor was narrow, which can be ignored when determining residence time. The residence times within heating entry length were also calculated and compared based on actual temperature profile versus constant wall temperature assumption (Table 4-5). The bias reflects the deviation of the actual residence times from the estimated values. The result shows that actual and estimated values are very close and the biases are below 5 % in most cases with only exception at 700 Run1. As discussed in section 4.1.1, the heating entry length was maximum 8 % of the entire reactor length. Therefore, heating time was also around 8 % of overall reaction time in the worst case given the small bias. Furthermore, temperature gradient in the heating entry length was large and the rate of reaction below 350 °C was negligible. The actual effect of the non-isothermal part on reaction was expected to be much less than 8 %. As a result, the reactor can be approximately treated as isothermal to investigate reaction kinetics.

Table 4-4. Comparison between actual and estimated reaction residence time in the full reactor section

| <b>Operation</b>              | 600 Run1 | 600 Run2 | 600 Run3 | 650 Run1 | 650 Run2 | 650 Run3 | 650 Run4 | 700 Run1 | 700 Run2 | 700 Run3 |
|-------------------------------|----------|----------|----------|----------|----------|----------|----------|----------|----------|----------|
| <b>Actual</b>                 |          |          |          |          |          |          |          |          |          |          |
| <b>residence time, s</b>      | 0.682    | 0.752    | 1.166    | 0.343    | 0.529    | 0.652    | 0.717    | 0.326    | 0.612    | 0.663    |
| <b><sup>a</sup>Estimated</b>  |          |          |          |          |          |          |          |          |          |          |
| <b>residence time, s</b>      | 0.689    | 0.759    | 1.176    | 0.344    | 0.532    | 0.657    | 0.722    | 0.327    | 0.616    | 0.667    |
| <b>Relative difference, %</b> | 1.03     | 0.93     | 0.86     | 0.29     | 0.57     | 0.77     | 0.70     | 0.31     | 0.65     | 0.60     |
| <b><sup>b</sup>Estimated</b>  |          |          |          |          |          |          |          |          |          |          |
| <b>residence time, s</b>      | 0.682    | 0.752    | 1.165    | 0.342    | 0.528    | 0.652    | 0.716    | 0.325    | 0.612    | 0.663    |
| <b>Relative difference, %</b> | 0        | 0        | 0.09     | 0.29     | 0.19     | 0        | 0.14     | 0.31     | 0        | 0        |

<sup>a</sup>Helium flow rate calculated at furnace set temperature <sup>b</sup>Helium flow rate calculated at average axial surface temperature of reactor tube

Table 4-5. Comparison between actual and estimated reaction residence time in the reactor heating entry section

| <b>Operation</b> | <b>Estimated residence time, s</b> | <b>Actual residence time, s</b> | <b>Bias, %</b> |
|------------------|------------------------------------|---------------------------------|----------------|
| 600 Run1         | 0.0205                             | 0.0210                          | 2.56           |
| 600 Run2         | 0.0183                             | 0.0187                          | 2.04           |
| 600 Run3         | 0.0057                             | 0.0058                          | 1.61           |
| 650 Run1         | 0.0255                             | 0.0265                          | 4.05           |
| 650 Run2         | 0.0225                             | 0.0232                          | 3.06           |
| 650 Run3         | 0.0187                             | 0.0191                          | 2.06           |
| 650 Run4         | 0.0167                             | 0.0170                          | 1.64           |
| 700 Run1         | 0.0263                             | 0.0277                          | 5.44           |
| 700 Run2         | 0.0175                             | 0.0178                          | 1.88           |
| 700 Run3         | 0.0159                             | 0.0162                          | 1.96           |

#### 4.1.3 Material Balance

The performance of the reactor was further verified by calculating the overall material balance, based on inflow and outflow. The inflow was HGO feed injected into the reactor and the outflow was gas, heavy liquid and coke. The amount of HGO into the reactor was the difference between total amount displaced by the pump and the amount staying in the tubing line. There were some errors in estimating the mass of feed in the pump and nozzle tube. Gas product consisted of fixed and liquefied gases, of which the amount was quantified by GC. Since H<sub>2</sub> and H<sub>2</sub>S cannot be detected by FID on GC and identification of peaks representing C<sub>4</sub>+ gases was ambiguous, negative errors existed in the amount of gases recovered. Heavy liquid was the portion of liquid product that still survived under vacuum filtration and rotary evaporation conditions. Light liquid with carbon number below 10 tended to be lost with solvent evaporation during the recovery process. The amount of heavy liquid collected was expected to be less if more

light liquid was produced. Coke was the solids in the liquid, glass wool and reactor outlet. The yield of coke was very low in all experiments, from 0.2 to 1.8 wt%, which can be considered negligible.

Figure 4-2 summarizes the mass recoveries and product yields for 10 groups of experiments. Mass balances were above 95 % at 600 °C and dropped to 80 % at 700 °C. Lower mass recovery was observed in proportion with higher gas yield, which is exhibited in Figure 4-3. The data points presented this trend except for two deviated points due to the error in product recovery.

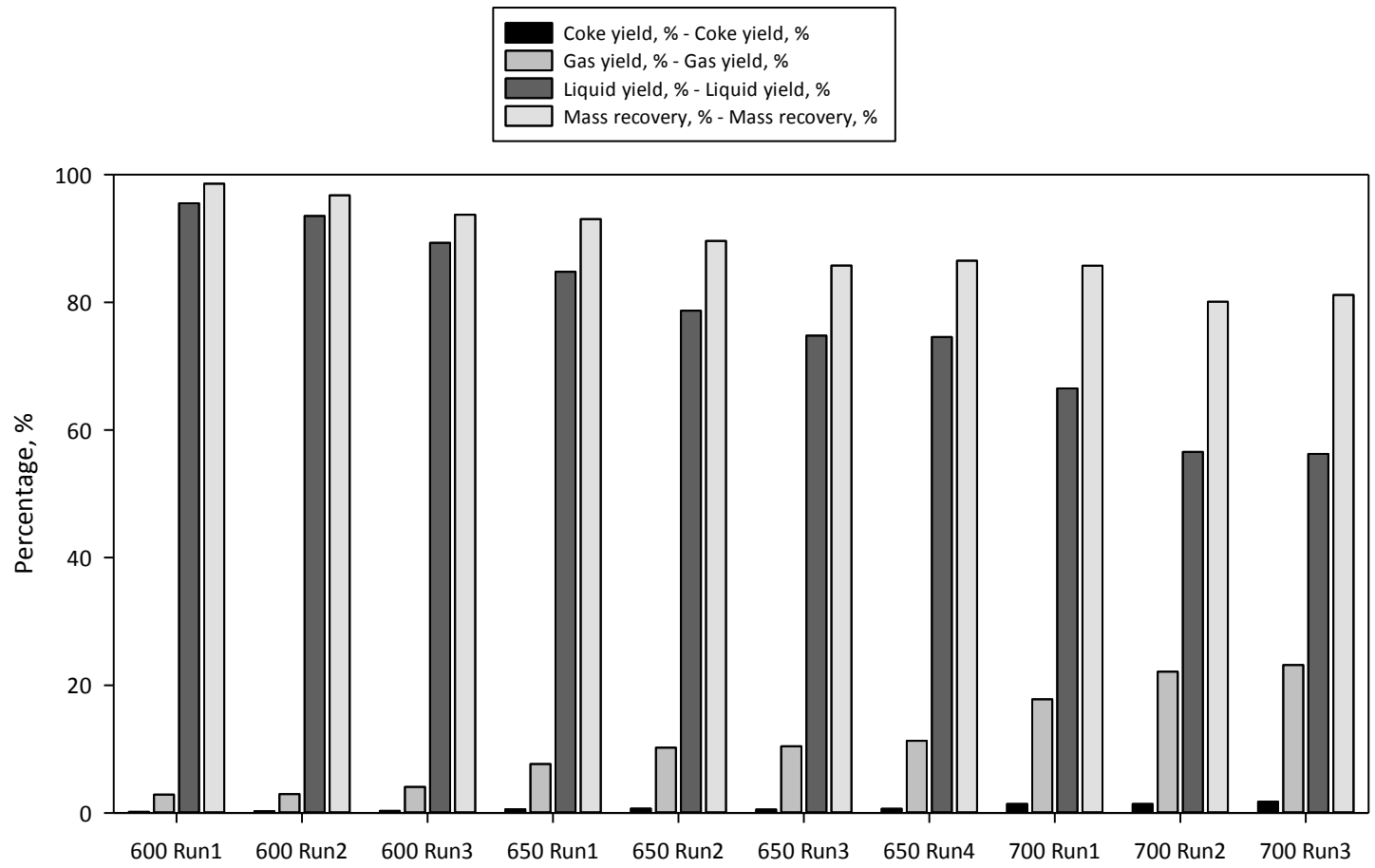


Figure 4-2. Mass recoveries and product yields on the basis of feed mass for all experiments

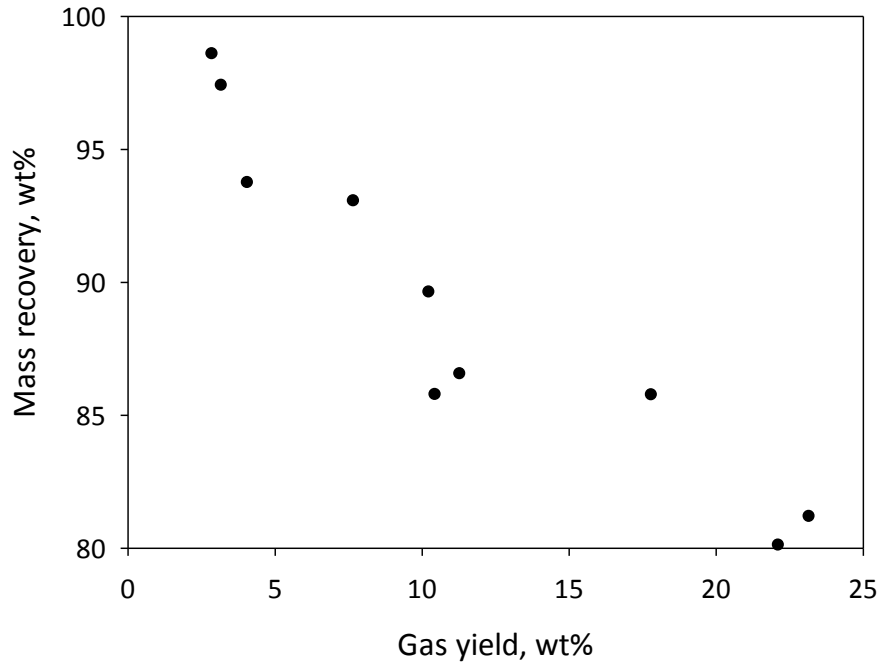


Figure 4-3. Change of mass recovery with gas yield

## 4.2 Conversion of Heavy Gas Oil

HGO was defined as the fraction with boiling point above 343 °C, which accounted for 96 wt% of the total feed. The conversions were defined based on the inlet and outlet flow rates of HGO fraction for a tubular reactor. The absolute amount of 343 °C+ fractions in the feed and liquid product was feasible by simulated distillation. The conversion was calculated from the total mass of feed, the total mass of heavy liquid product, and the simulated distillation results as follows.

$$X = \frac{w_{343\text{ }^{\circ}\text{C}+ \text{ feed sample}} m_{\text{feed}} - w_{343\text{ }^{\circ}\text{C}+ \text{ liquid product sample}} m_{\text{heavy liquid product}}}{w_{343\text{ }^{\circ}\text{C}+ \text{ feed sample}} m_{\text{feed}}} \quad (4.14)$$

Where  $m_{\text{feed}}$  is the mass of feed and  $m_{\text{heavy liquid product}}$  is the mass of recovered heavy liquid product;  $w_{343\text{ }^{\circ}\text{C}+ \text{ feed sample}}$  and  $w_{343\text{ }^{\circ}\text{C}+ \text{ liquid product sample}}$  are the fractions of 343 °C+

material in the injected feed and liquid product samples measured by simulated distillation.

The conversions measured by both ASTM 2886 and ASTM 6352 for 10 groups of experiments are listed and compared in Table 4-6. ASTM 2886 method is applicable to samples having an initial boiling point greater than 55.5 °C and a final boiling point of 538 °C or lower at atmospheric pressure. The calibration mixture covered the boiling range from n-C<sub>5</sub> to n-C<sub>44</sub>. ASTM 6352 method is feasible to samples with boiling range from 174 to 700 °C. The prepared calibration mixture in our experiment included C<sub>5</sub>-C<sub>20</sub> mixture and C<sub>20</sub>-C<sub>120</sub> polywax, which extended the measurable boiling range. The major fraction of the feed and liquid product samples had boiling range from 174 to 538 °C, making both methods acceptable. The two simulated distillation methods gave very close conversion data ranging from 10 to 60 %. This range was neither too low (<10 %) that may cause difficulty in analysis nor too high (>90 %) that was hard to maintain isothermal condition. The variation of conversion was reasonable and consistent with the operating temperatures and residence times. At a given temperature, conversions for any two runs at similar residence times were also very close, which suggests high repeatability in different experiments.

Table 4-6. Measured conversions at different operating conditions

|             | Furnace set<br>point<br>temperature, °C | Residence<br>time, s | Conversion, %<br>(ASTM 2887) | Conversion, %<br>(ASTM 6352) | Average<br>conversion, % |
|-------------|---|----------------------|------------------------------|------------------------------|--------------------------|
| 600<br>Run1 |   | 0.682                | 11                           | 11                           | 11                       |
| 600<br>Run2 | 600                                     | 0.752                | 12                           | 13                           | 13                       |
| 600<br>Run3 |   | 1.166                | 19                           | 17                           | 18                       |
| 650<br>Run1 |   | 0.343                | 26                           | 25                           | 26                       |
| 650<br>Run2 | 650                                     | 0.529                | 34                           | 32                           | 33                       |
| 650<br>Run3 |   | 0.652                | 37                           | 37                           | 37                       |
| 650<br>Run4 |   | 0.717                | 39                           | 38                           | 39                       |
| 700<br>Run1 |   | 0.326                | 49                           | 47                           | 48                       |
| 700<br>Run2 | 700                                     | 0.612                | 56                           | 54                           | 55                       |
| 700<br>Run3 |   | 0.663                | 58                           | 56                           | 57                       |

The correlation between mass recovery and conversion is plotted in Figure 4-4. Mass balances ranged from 80-99 % and dropped significantly with increase of conversion. At low conversion range, more than 95 % mass recovery was obtained, validating the satisfying performance of the apparatus. Lower recovery at high conversion range was

consistent with more light liquids produced. Loss of volatile light fractions was inevitable, but could be verified by analyzing collected solvent.

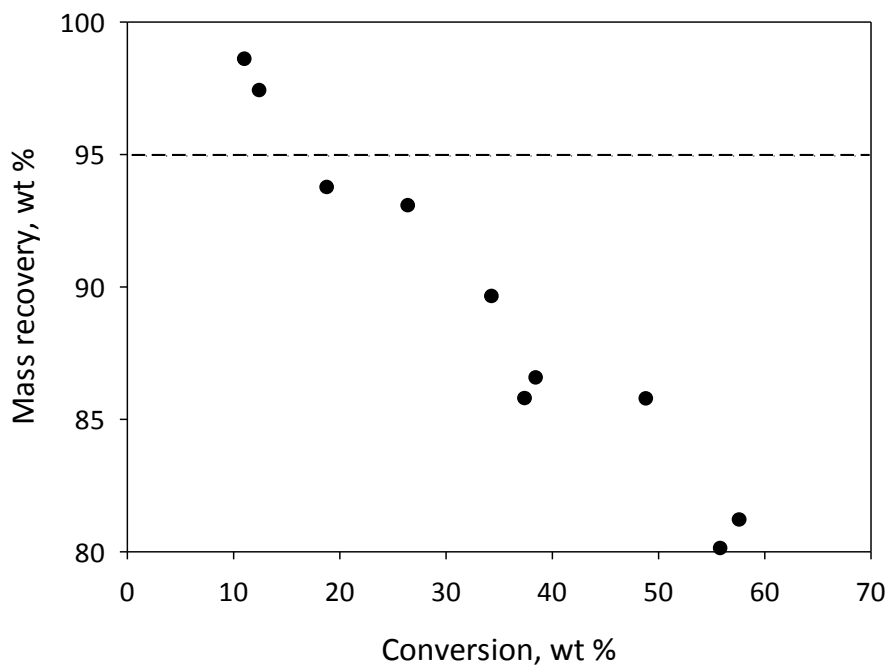


Figure 4-4. Variation of mass recovery as a function of conversion

Figure 4-5 shows the results of GC analysis of the methylene chloride used for liquid product recovery. Some peaks after the solvent peak indicated that significant amounts of light product components were removed with the solvent. This point was further proved by observing that some light liquids vaporized in the receiving flask and condensed inside of the vacuum hose during filtration.

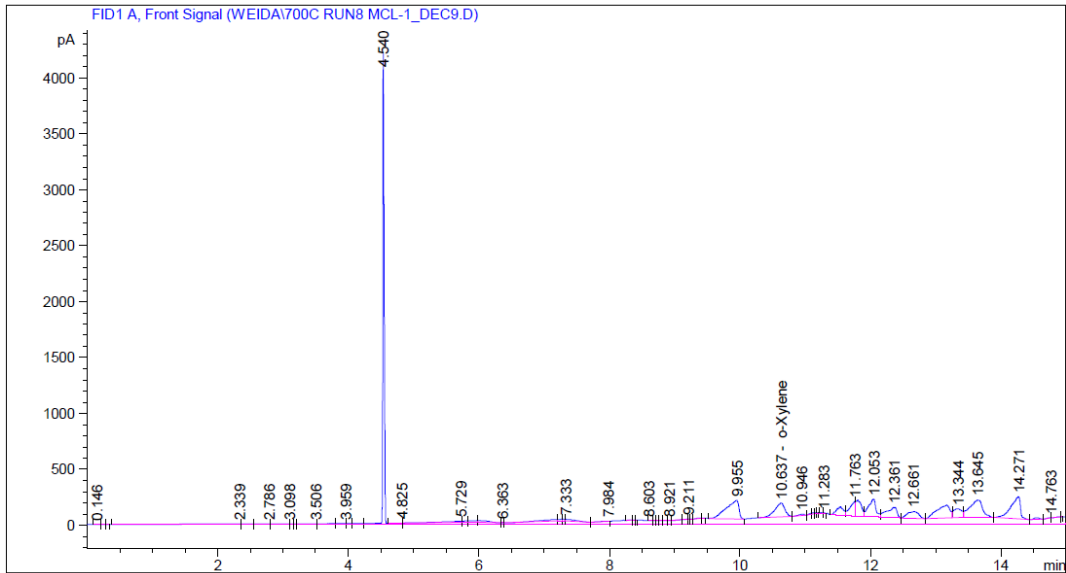


Figure 4-5. CG analysis of recovered methylene chloride solvent

### 4.3 Yield and Distribution of Cracked Products

#### 4.3.1 Coke Yield

One of the targets of the research was to verify the low coke yield in vapor phase cracking of HGO over the operating temperature range. Figure 4-6 presents the coke yield as the conversion was varied from 10 to 60 %. Different residence times were applied at each temperature. Coke yield slightly increased with the increase of conversion and it was below 2 % for all operations.

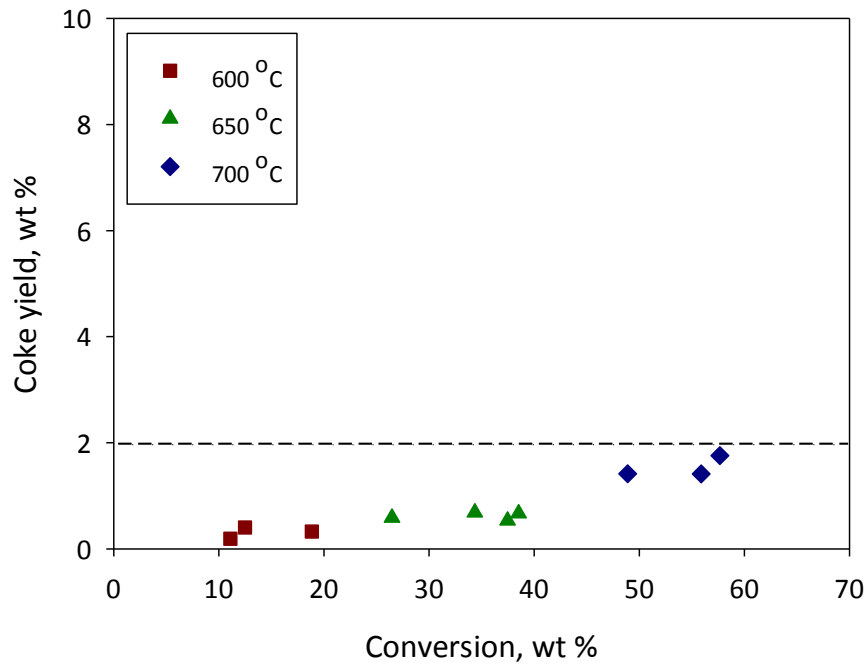


Figure 4-6. Coke yield versus conversion of heavy gas oil feed

The data show that coke yield was nearly constant with change of conversion at the same temperature. This suggests that coke yield was not sensitive to residence time but notably affected by reaction temperature. Low coke yield at all conversions was consistent with feed property and pure gas phase cracking scenario. The aromatic carbon content (MCR) of HGO fraction was expected to be very low given the fact that most MCR content is mainly in the residue fraction. Consequently, the coke forming tendency of our feed was also low. In terms of coking formation in gas phase, there are three mechanisms proposed in the literature (Reyniers et al., 1994; Albright et al., 1988). The first one is heterogeneous catalytic mechanism in which coke formation is catalyzed by metal surface of tube inner wall, particularly by nickel alloys. The nickel composition of the reactor material was from 12.5 to 14.0 wt%. The second mechanism is heterogeneous noncatalytic reaction, claiming that unsaturated light components in gas

phase react with the free radicals on the coke surface via addition. The third mechanism is homogeneous noncatalytic reaction, stating that small aromatics grow into polynuclear aromatics followed by condensation and dehydrogenation to produce tar droplets and coke particles. Coke formation by the first two mechanisms is generally very slow and the yield is quite low. These types of coke generally precipitated on the inner surface of the reactor and formed a layer, which is in agreement with that some carbonaceous materials were observed on the reactor internal surface. Most of these coke materials were not collected by washing the reactor tube and so as accumulated gradually. According to the third mechanism, aromatics tend to form coke in vapour phase cracking of HGO. Most of these coke particles stayed in the gas phase and were carried out by sweep gas. They were collected by filtering the colored particles from the reactor product in the cryogenic condensers. Therefore, the determined coke yield is literally based on the third mechanism. However, it is only important when the temperature is higher than 700 °C that aromatic compounds can undergo further dehydrogenations. This probably explains why the coke yield was relatively sensitive to temperature in vapour phase cracking. Our reactions occur in a helium-diluted gas phase with low reactant concentration and the operating temperature was from 600 to 700 °C. Bimolecular reactions such as addition and H-abstraction are important in coke formation but are not favoured in our reaction conditions. The operating temperature range was also below the point that significant aromatics produce coke. Consequently, the coke yield was very low in our operations though given high aromatic content in the feed. Most aromatic compounds were expected to not react at all and stay unchanged in the liquid product.

### 4.3.2 Gas Product Yield

Gas product was comprised of both fixed and liquefied gases with carbon number of one to six. Analysis of total gas yield at different operating conditions was of interest. The trend of gas yield with conversion is exhibited in Figure 4-7.

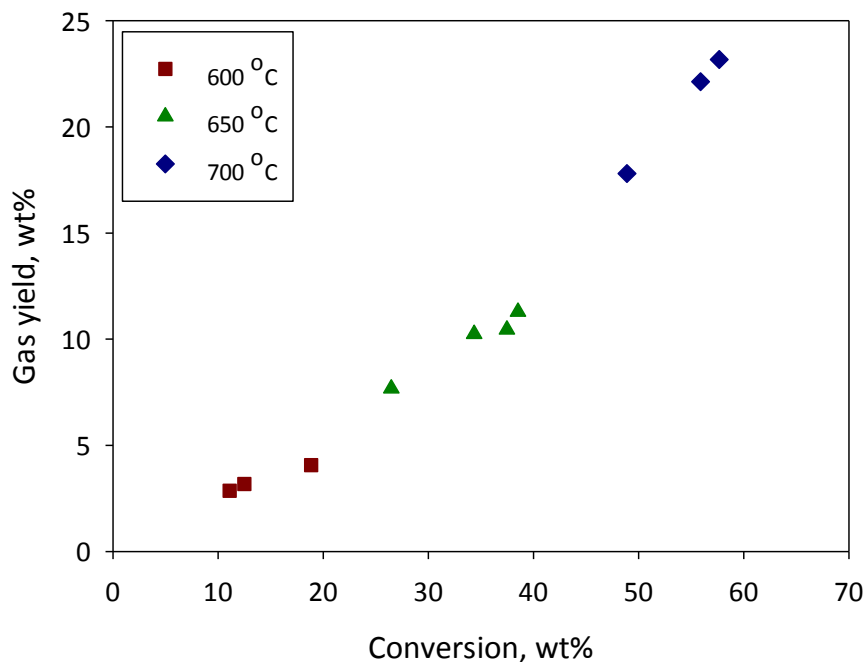


Figure 4-7. Gas yield versus conversion at different residence times and temperatures

Although some errors existed in measuring the gas yield, the results show good consistency. The gas yield increased monotonically with increase of conversion even between two adjacent values, which was in agreement with the reduction in heavy liquid yield. The stoichiometric yield ratio is defined as  $\Delta \text{gas yield} / \Delta \text{conversion}$  from the origin. The data points at both 600 °C and 650 °C show constant proportionality through the origin, which implies the fixed stoichiometric yield ratio at each temperature. The ratios at these two temperatures were very similar with the value at 650 °C slightly higher. This suggests that vapor phase cracking of HGO produced

gas yield proportional to conversion at 600 °C and 650 °C. Within this temperature range, cracking mainly occurred on the feed material with boiling point above 343 °C. In contrast, the data points at 700 °C were fundamentally different, featuring variable stoichiometric yield ratio. This is due to significant cracking of product material with boiling point below 343 °C at such a high temperature. The conclusion can be reached that temperature had a strong effect on the stoichiometric yield ratio. More feed conversion contributed to gas yield at higher temperature.

#### 4.3.3 Yield of Olefins Versus Alkanes

Olefins, especially ethylene and propylene, are of importance among gas products due to their high value. The yields of ethylene + propylene and ethane + propane were measured and their relationship with conversion is illustrated in Figure 4-8.

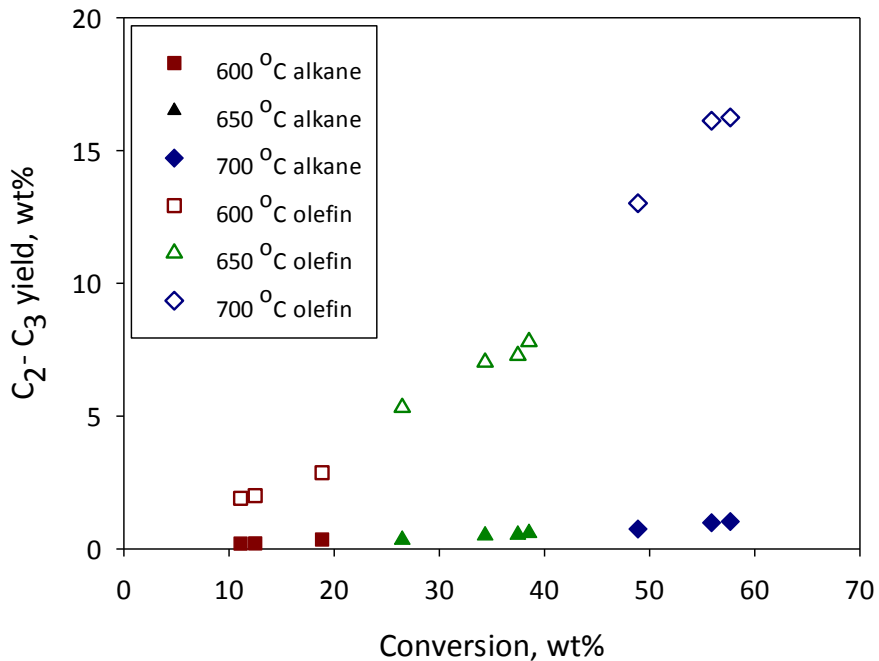


Figure 4-8. Comparison between C<sub>2</sub>-C<sub>3</sub> olefin and alkane yields at different conversions

The results show that the yield of ethane + propane was very low, ranging from 0.2 to 1.0 % at conversions of 10 - 60 %, which suggests weak correlation between alkane yield and conversion. In comparison, the yield of ethylene + propylene was significantly higher than that of ethane + propane at any condition. Moreover, the difference of yield increased with increase of conversion. The yield of olefin was around 2 wt% higher than that of alkane at low conversion of 10 % while 15 wt% more olefin was produced at conversion close to 60 %. The product distribution and pattern shows a strong consistency with vapor phase cracking behavior. The concentration of reacting species in our reactor was very low since reactant vapor was highly diluted by helium sweep gas at atmospheric pressure. Thermal cracking of HGO feed likely followed the free radical mechanism in which  $\beta$ -scission, radical addition and H-abstraction are important propagation steps. In vapor phase cracking with reactant highly diluted by helium sweep gas, chances of bimolecular reactions were reduced to be minimum. As a consequence, unimolecular reactions such as  $\beta$ -scission would be predominant over addition and H-abstraction in the vapor phase environment. Free radicals would decompose to form olefins and smaller radicals and so on. Clearly,  $C_2$ - $C_3$  olefin production was preferable at high temperature and short residence time operation. The total yield of ethylene and propylene was from 2-16 % corresponding with 3-23 % of total gas yield, which proved that  $C_2$ - $C_3$  olefin was the primary gas product. In order to further investigate the efficiency of olefin production, the olefin selectivity was defined as

$$S = \frac{m_{\text{ethylene+propylene}}}{m_{\text{feed converted}}} \quad (4.15)$$

The mass of feed converted was the difference between mass of HGO fraction in feed and in liquid product, which was determined by simulated distillation. The relationship between olefin selectivity and conversion is shown in Figure 4-9.

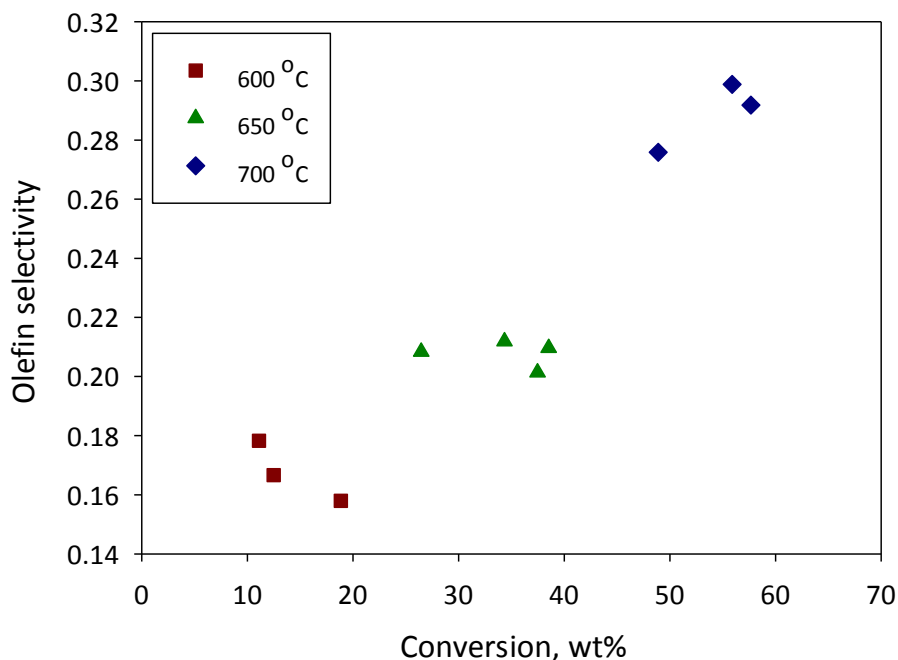


Figure 4-9. Olefin selectivity as a function of conversion

The data indicates that olefin selectivity increased dramatically with increase of conversion. The temperature was still the dominant effect whereas no correlation showed between selectivity and conversion at each of the three temperatures. When temperature was as high as 700 °C, approximately 30 % of converted feed ended up with ethylene and propylene at conversion approaching 60 %. This further substantiates that high temperature favored C<sub>2</sub>-C<sub>3</sub> olefin production in vapor phase cracking.

Methane was another important gas product besides C<sub>2</sub>-C<sub>3</sub> olefins and alkanes. It was unwanted product since it has no high value as C<sub>2</sub>-C<sub>3</sub> olefins while captures hydrogen by

removing hydrogen rich fragments from liquid product. The yield of methane at different conversions is illustrated in Figure 4-10.

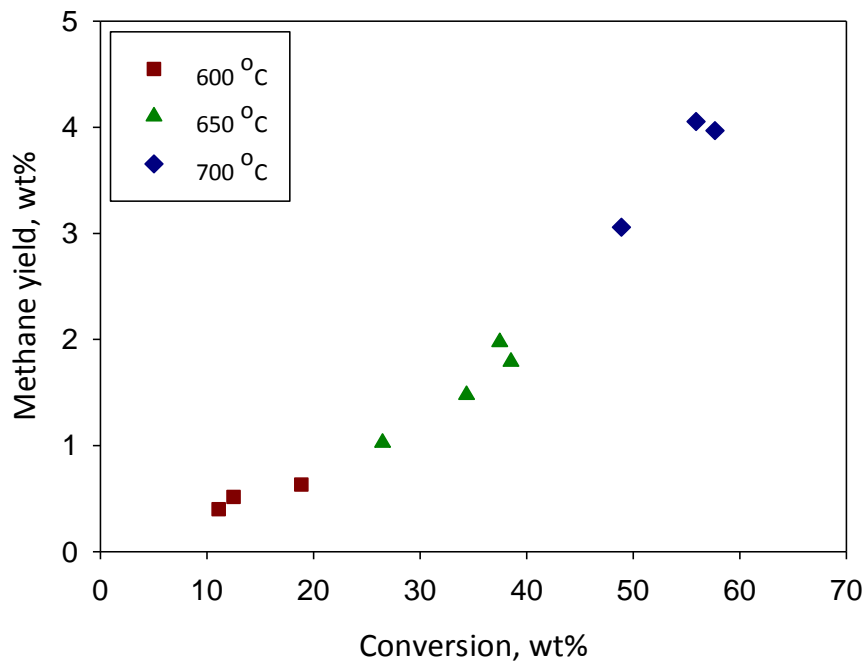


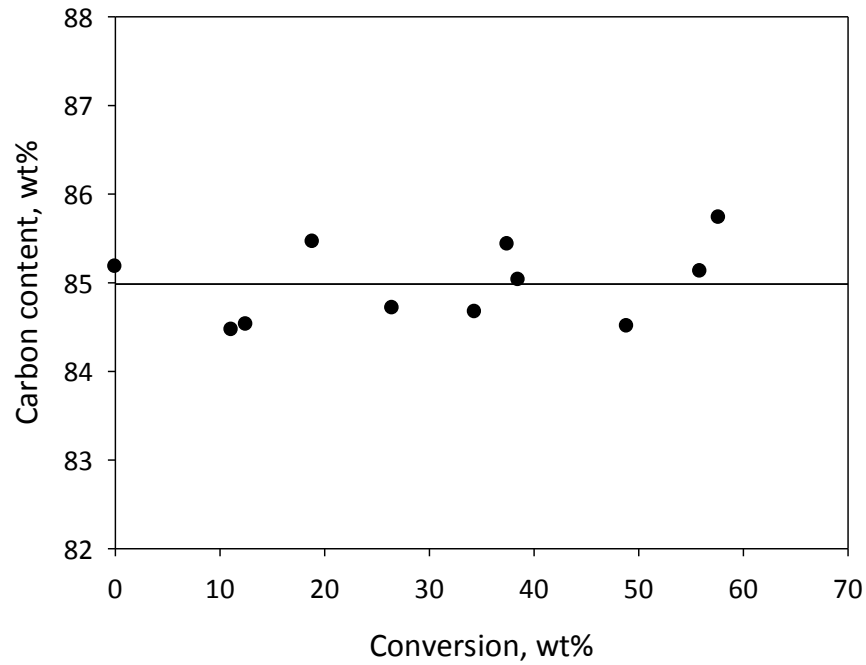
Figure 4-10. Methane yield as a function of conversion

The yield of methane as conversion exhibited the same trend as total gas yield and C<sub>2</sub>-C<sub>3</sub> olefin yield. It increased slowly at low temperature and rapidly at high temperature with increase of conversion, which also exhibited higher stoichiometric yield ratio of methane over conversion at higher temperature. Methane is a stable product in vapor phase cracking of hydrocarbons. Consequently, it was expected to increase continuously with conversion.

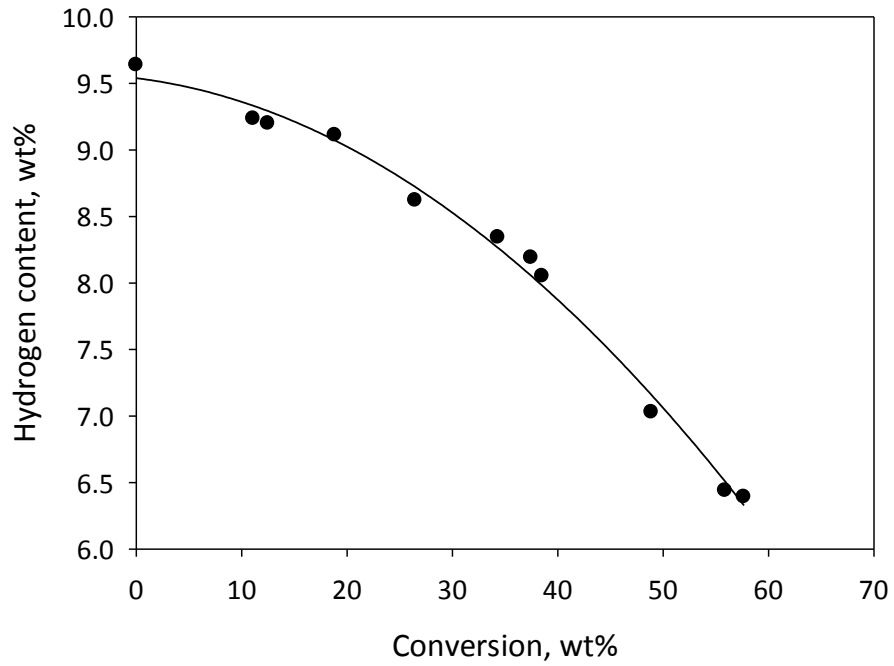
## 4.4 Liquid Product Quality

### 4.4.1 Elemental Composition

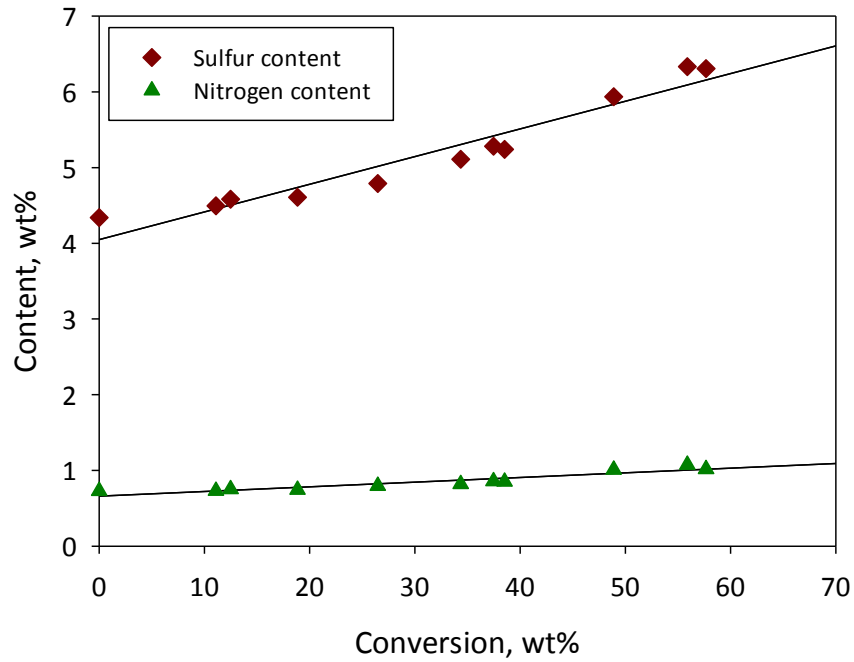
Elemental analysis on HGO feed and liquid product gave an insight into how the vapor phase cracking changed the elemental composition of the liquid product. The correlations of carbon, hydrogen, sulfur and nitrogen contents with variation of conversion are illustrated in Figure 4-11. Zero conversion indicates the feed composition.



(a)



(b)



(c)

Figure 4-11. Relationship between carbon content (a), hydrogen content (b), sulfur and nitrogen content (c) and changing conversion for liquid product. The lines show the linear regression results for the data, except for hydrogen which shows a second order regression curve.

Despite the scatter of the data points in the Figure 4-11 (a), carbon content was statistically constant with the mean value of 85 wt % at conversions from 0 to 60 %. This result implies that carbon content was not instructive to reflect the quality change of the liquid product with conversion.

Hydrogen content had a broad variation from above 9.6 wt % in feed to below 6.4 wt % in liquid product when the conversion was close to 60 %. The parabolic trend line shows significant loss of hydrogen from the liquid products with increase of conversion. This result was consistent with the trend of increasing gas yield at higher conversion, which suggests that vapour phase cracking tended to remove hydrogen from liquid product to the gases. Hydrogen content is a key quality parameter of liquid product. Higher hydrogen content corresponds to lower density or higher API<sup>o</sup>. Liquid product with low hydrogen content was also expected to be rich in unsaturated aromatics. If we targeted liquid product, vapour phase cracking was unfavourable since it reduced both yield and quality by forming a high yield of light ends, leaving liquid product with low hydrogen and high aromatic content. As shown in Figure 4-11 (b), data points followed a quadratic profile with R square equal to 0.993. When they were fitted by linear curve, the R square value was reduced to 0.943. The preference of quadratic model over linear model was further substantiated by F-test, in which the F statistic can be calculated as

$$F = \frac{(RSS_1 - RSS_2) / (DF_1 - DF_2)}{RSS_2 / DF_2} \quad (4.16)$$

Where *RSS* represents the residual sum of square of the model; *DF* is the degree of freedom of the model, calculated as the difference of number between total data points and variables ; suffix 1 and 2 represent simple and complicated models.

The F ratio quantifies the relationship between the relative decrease in sum of squares and the relative decrease in degrees of freedom. The F statistic and P value for quadratic and linear models were calculated to be 53.5 (greater than 1) and 0.000083 (less than 0.05). This result suggests that the quadratic model fitted the data much better. The profile shows a slow decrease of hydrogen content at low temperature range followed by a sharp reduction at high temperature with increase of conversion. The residence time used was in the same range (between 0.337 s and 0.484 s) at each temperature. Consequently, the change of hydrogen content was more sensitive to residence time at higher temperature operation.

As illustrated in Figure 4-11 (c), nitrogen content did not systematically increase with higher conversion. This result supports the conclusion that all nitrogen compounds are highly resistant to removal by thermal cracking due to their aromatic structure.

Remarkably, the sulphur content of the liquids increased steadily with an increase of conversion. The HGO feed in our study was produced from bitumen by fluid coking, in which most organic sulfides have been already reacted. The left material was only enriched in unreactive aromatic sulfur compounds. As a result, the absolute amount of sulfur was almost fixed as thermal cracking proceeded. However, based on mass balance, higher sulfur content in liquid product must compensate for lower hydrogen content with increase of conversion given that carbon and nitrogen contents were nearly constant.

#### **4.4.2 Chemical Structure**

The change of chemical structure of the liquid products was investigated by  $^{13}\text{C}$  NMR analysis. The aromatic carbon content was the key structural information. HGO feed

representing conversion of 0 % and liquid product at conversions of 11 %, 19 %, 39 %, 49 %, 58 % was selected and analyzed. These representative samples covered the full conversion range from this study. The molar fraction of aromatic carbons is plotted in Figure 4-12 as a function a conversion.

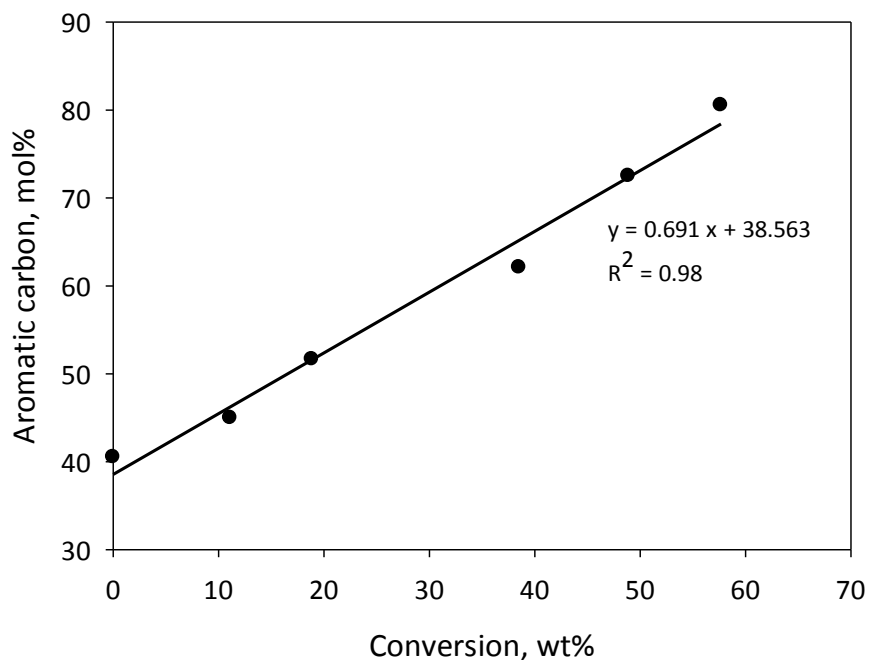


Figure 4-12. Aromatic carbon content of heavy liquid product fraction as a function of conversion

As illustrated in Figure 4-12, the data points present a good linear trend with correlation coefficient 0.98. The regression equation allowed us to predict aromatic carbon content at any given conversion in the range. The feed contained about 40 mol % aromatic carbon, which was consistent with highly aromatic coker gas oil. Increase of aromatic carbon content with increase of conversion suggests that liquid product became more and more aromatic with vapor phase cracking, consistent with loss of hydrogen content at higher conversion. The easily reacted side chains attached to aromatics and sulfides would be cracked and evolved as gases which reduced hydrogen content. In contrast,

the aromatic compounds were intact and preserved in the course of thermal cracking, except for the insignificant yield of coke. The loss of aromatics in coke was negligible; therefore, the net concentration of aromatics in liquid product kept going higher with removal of aliphatics as fragments in the gas fraction. This is further substantiated in Figure 4-13 which correlates aromatic carbon content with hydrogen content for feed and liquid products over the conversion range.

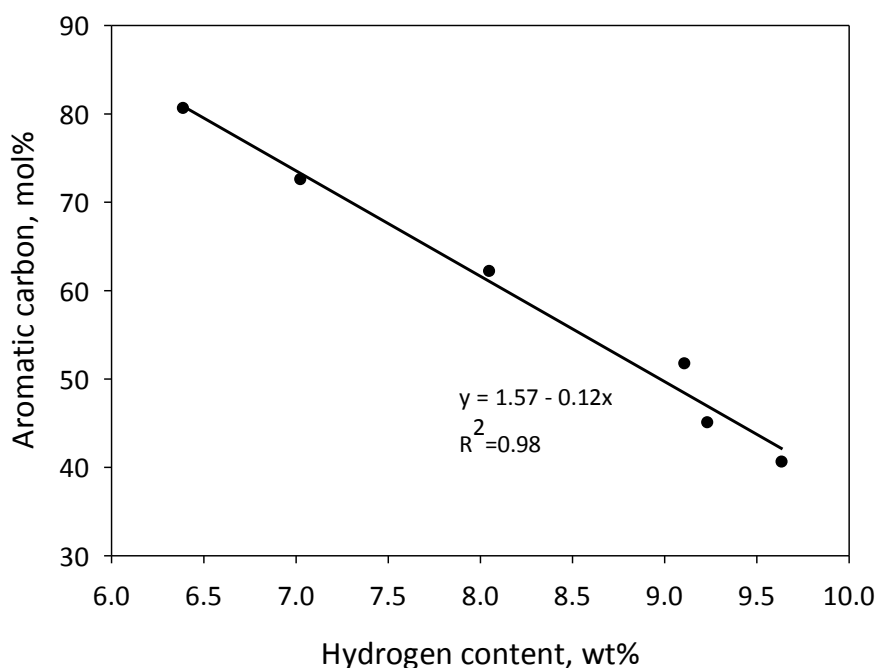


Figure 4-13. Correlation between aromaticity and hydrogen content of the liquid product, only data measured directly by  $^{13}\text{C}$  NMR and elemental analyzer are included

The yield ratio for aromatic carbon was very instructive to determine how aromatic carbon in feed changed during thermal cracking in vapor phase. It was calculated as

$$y_{\text{aromatic C}} = \frac{m_{\text{aromatic C in liquid product}}}{m_{\text{aromatic C in feed}}} \quad (4.17)$$

This ratio reflects how much aromatics in liquid product were created or lost relative to those in feed. It is correlated with conversion in Figure 4-14 to investigate the impact of reaction depth on the variation of aromatic carbon.

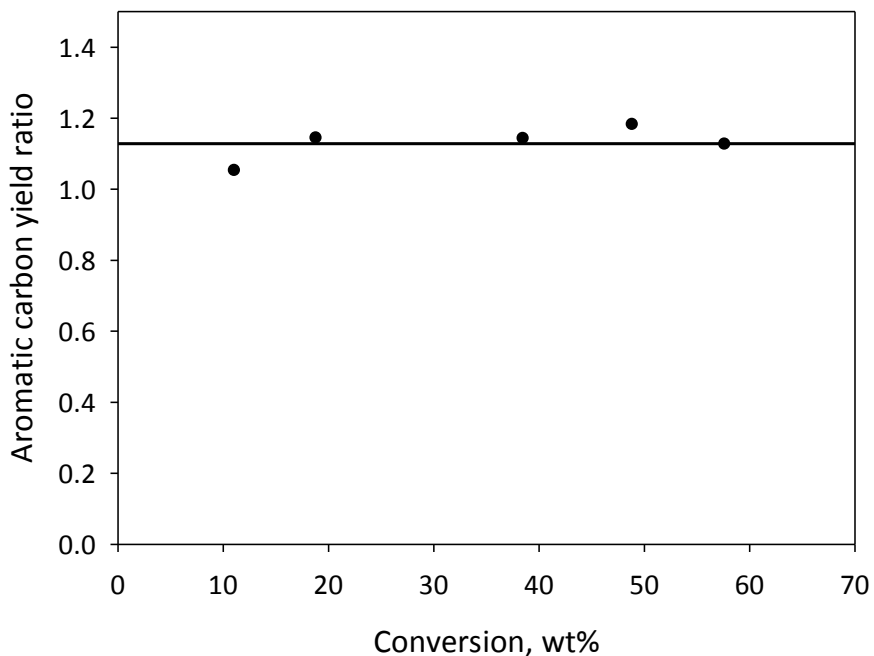


Figure 4-14. Change of aromatic carbon content with conversion, only data measured directly by  $^{13}\text{C}$  NMR are included.

The data show no systematic variation of total aromatic carbon in the liquid product with increase of conversion. The measured data gave an average ratio about 1.13, which pointed out that more aromatics were created in liquid product during reaction. If interpolated data points obtained by the linear regression above in Figure 4-12 were included, the ratio was estimated to be 1.20. Both measured and interpolated data gave the same trend and close ratio value. The constant ratio in the conversion range suggests that all new aromatics were formed at low conversion and stayed invariant with further reaction, which implies a fast reaction step to generate aromatics.

Aromatics in liquid product can be created either from naphthenes or side chains in aromatic HGO. The olefins from cracked side chains can build aromatics by free-radical additions followed by rearrangements, however, vapor phase cracking did not favor this mechanism. As a result, dehydrogenation of naphthenes via hydrogen transfer was likely the dominant reaction to produce aromatics. Furthermore, the bitumen derived aromatic HGO was rich in naphthenic groups (Ng et al., 2002; Woods et al., 2004), providing high chance for dehydrogenation. Consequently, the vapor phase cracking of aromatic HGO can be described as a two-step reaction in which fast dehydrogenation of naphthenic groups was followed by slower cracking of side chains and surviving cycloalkyl rings. With increased conversion, the reactants would be more and more aromatic component, giving even lower reactivity than the starting material. This mechanism was strongly corroborated by the link between change of chemical structure and type of reaction from interpretation of the  $^{13}\text{C}$  NMR analysis data. The schematic of the mechanism is illustrated in Figure 4-15.

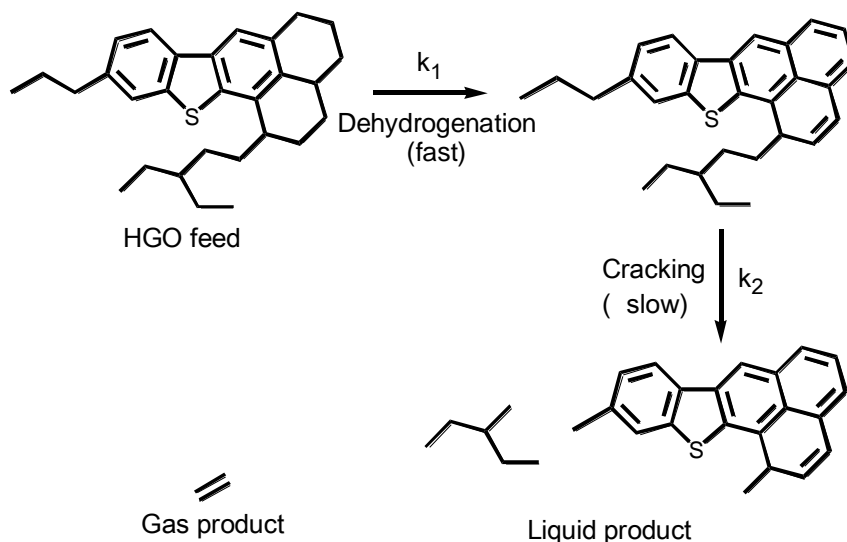


Figure 4-15. Two-step mechanism for vapor phase cracking of aromatic-naphthenic HGO

#### 4.5 Kinetics of Vapor Phase Cracking of Bitumen Derived Heavy Gas Oil

Thermal cracking of bitumen derived HGO follows apparent first-order kinetics (Gray, 1994). It was developed on mass basis due to lack of molecular weight of the complex mixture. Thereby, the rate expression was:

$$-r_{HGO} = k_{HGO}W_{HGO} \quad (4.18)$$

The mass concentration of HGO was defined as:

$$W_{HGO} = \frac{m_{HGO}}{V_{HGO}} \quad (4.19)$$

The temperature dependence of the rate constant was described by the Arrhenius expression:

$$k_{HGO} = A \exp\left(\frac{-E_a}{RT}\right) \quad (4.20)$$

The design equation of tubular reactor was developed based on mass balance of reactant. For each differential segment of the reactor, the mass balance equation was reduced to:

$$\frac{dF_{HGO}}{dV} = r_{HGO} \quad (4.21)$$

For each differential volume, the reactor was isothermal with temperature corresponding to the position. Since the reactant was highly diluted by helium sweep gas, the mass concentration of HGO can also be expressed as:

$$W_{HGO} = \frac{F_{HGO}}{v} \quad (4.22)$$

Substituting volume with length, the final equation linking mass balance and rate expression was:

$$\frac{dF_{HGO}}{dx} = -A \exp\left(\frac{-E_a}{RT_m}\right) \times \frac{T_0 F_{HGO}}{T_m v_0} \times A_R \quad (4.23)$$

where  $F_{HGO}$  the mass flow rate of HGO is,  $x$  is the length of the reactor,  $A_R$  is the cross sectional area,  $T_0$  is the room temperature and  $v_0$  is the volume flow rate of helium at room temperature.

Temperature was a function of reactor length, approximated from the equations for constant wall temperature:

$$T_m = T_s - (T_s - T_{m,i}) \exp\left(-\frac{\pi D \bar{h}}{m C_p} x\right) \quad (4.24)$$

As discussed in section 4.1.1, this derivation underestimated the length of the non-isothermal section of the reactor by circa 5-10 cm. Based on equation 4.23 and 4.24, mass flow rate of the reactant  $F_{HGO}$  is a function of reactor axial position  $x$ .

For the first estimation, the kinetics was analyzed assuming the reactor was isothermal.

Then, the final equation was reduced to:

$$\ln(1 - X) = -k_w \tau \quad (4.25)$$

The furnace set point temperatures were used to predict the apparent first-order rate constants for HGO fraction (defined as 343 °C +) conversion in ten groups of experiments. At each operating temperature, the actual rate constant would be lower

within the non-isothermal part at the entry of the reactor, and then remain constant. Consequently, the estimated rate constants were the average values.

The estimated rate constants at different conversions are shown in Figure 4-16. Within the low conversion range at 600 °C operation, the rate constants were invariable with conversion as anticipated. A systematic change in rate constants was noticed when conversion was higher, in that they became dependent on conversion, particularly within the high conversion range at 700 °C operation. The overall trend suggests that the higher the conversion, the more the rate constants were dependent on conversion. The aliphatic groups in the reactant, such as side chains and sulfides, featured high reactivity while the aromatic groups were inert during thermal cracking. The recovered liquid products which contain all unconverted HGO fraction possessed higher aromatic carbon content and lower hydrogen content as increase of conversion. The easily reacted materials were continuously removed and aromatics were accumulated in the HGO boiling range in the course of thermal cracking. As a consequence, further conversion on this unconverted HGO material became more difficult. This clearly indicates that the decrease of the rate constants with conversion was attributed to loss of reactivity of reactant with increase of conversion. In other words, simple first-order kinetics failed because the reactants in the vapor phase were not the same at high conversion as at low conversion.

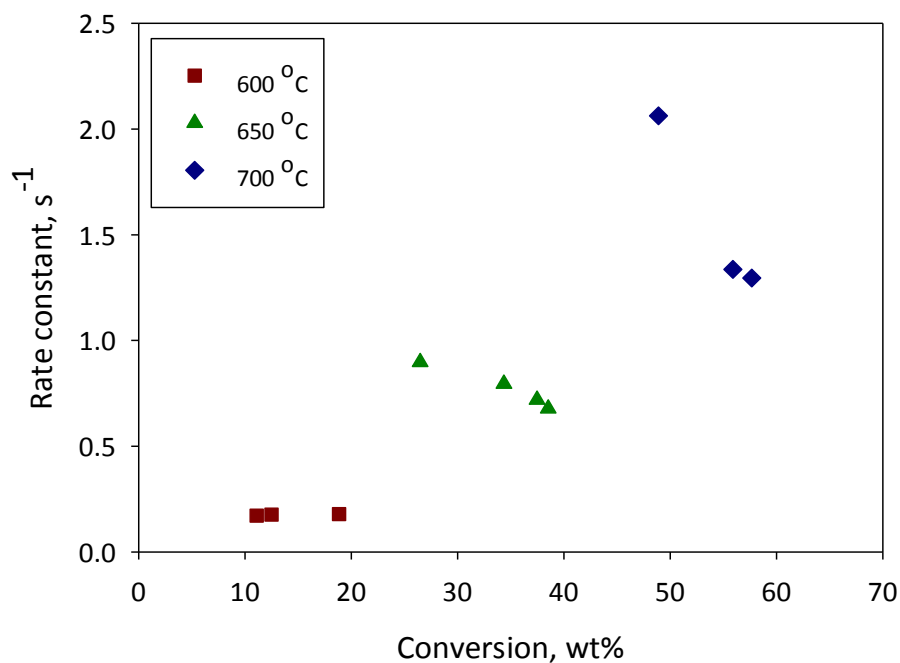


Figure 4-16. Variation of rate constant with conversion at different temperature

The rate constant is only dependent on temperature in a simple first-order kinetic model, which may fail to describe thermal cracking of highly aromatic HGO in our case. In order to test the hypothesis, the apparent activation energy for conversion of HGO fraction was predicted assuming isothermal reactor conditions. The Arrhenius plot correlating rate constant and temperature is illustrated in Figure 4-17. The data points were not satisfactorily fitted by linear regression with low correlation coefficient. The slope of the data gave activation energy only 154 kJ/mol, which was far below reported literature values (Zou et al., 1993; Su et al., 1997). This outcome substantiated the hypothesis that a simple first-order kinetic model was unable to correlate the kinetics of cracking of bitumen-derived HGO.

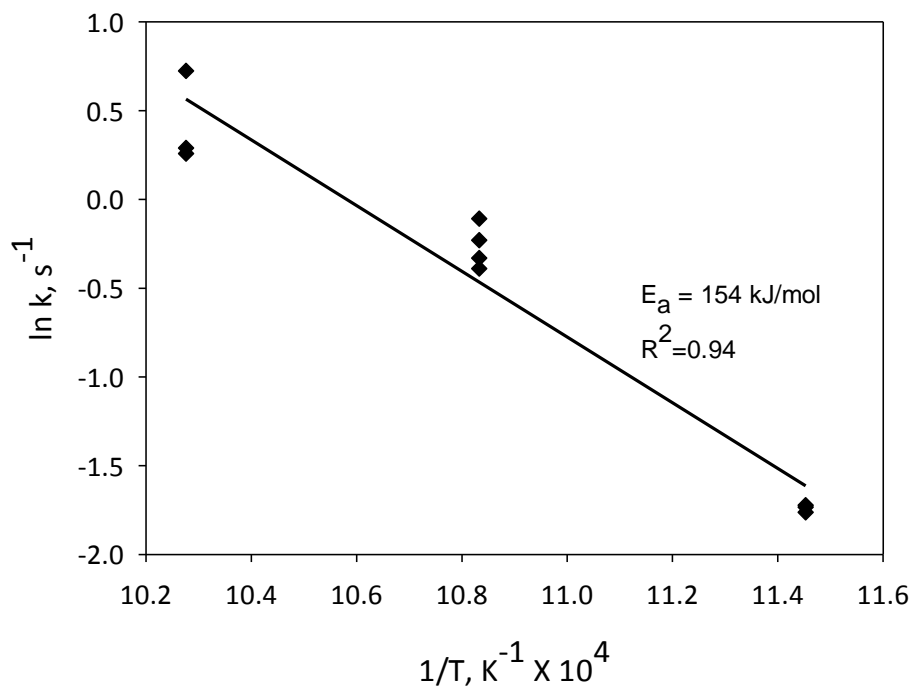


Figure 4-17. Arrhenius plot for conversion of heavy gas oil fraction (343 °C+), reaction was assumed to be isothermal at furnace set point temperatures

The assumption of isothermal conditions was used in the calculation. If only the length of the reactor where fluid temperature was within 5 °C of the average surface temperature was considered, the residence time would be reduced at most 8 % as discussed in section 4.1.1. Conversion was almost unchanged by ignoring the heating entry length due to the large temperature gradient. The change of residence time was not able to affect the decreasing trend of rate constants especially at 700 °C. Therefore, our assumptions regarding the heating profile did not have strong effect on the values of rate constants and apparent activation energy.

Two possible factors contributed to the lower rate constants than expected: either conversion was underestimated or residence time was overestimated. Measurement on residence time was very reliable given high repeatability of various experiments. The

conversion data were also believed to be of high accuracy due to high reproducibility on two different GCs. The conversion calculated from simulated distillation was on the basis of entire 343 °C + fraction in feed. If only the reactive species were used as basis, the conversion was expected to be much higher. Therefore, the presence of unreactive aromatics in the feed resulted in lower estimated conversion. Only the conversion of reactive species in HGO was of interest in our study while the mass of aromatic rings played the role of an inert. According to the proposed model in Figure 4-14, a two-step reaction occurred on reactive species: dehydrogenation of naphthenic groups and cracking of the remaining non-aromatic groups. The former reaction converted naphthenes to aromatics, which would shift boiling point slightly higher. The latter reaction contributed to the boiling point reduction. As a result, cracking of non-aromatics after dehydrogenation was the only key reaction in conversion of HGO (343 °C + fraction). The corresponding conversion can be calculated as:

$$X_{NA} = \frac{m_{343\text{ }^{\circ}\text{C}+ \text{NA in feed}} - m_{343\text{ }^{\circ}\text{C}+ \text{NA in liquid product}}}{m_{343\text{ }^{\circ}\text{C}+ \text{NA in feed}}} \quad (4.26)$$

where  $m_{343\text{ }^{\circ}\text{C}+ \text{NA in feed}}$  is the mass of non-aromatics in 343 °C + of feed after dehydrogenation, and  $m_{343\text{ }^{\circ}\text{C}+ \text{NA in liquid product}}$  is the mass of non-aromatics in 343 °C + of liquid product.

The mass of non-aromatics in feed after dehydrogenation and in the liquid product can be determined by elemental composition and aromatic carbon content based on the following assumptions:

1. Feed and liquid product were considered as a mixtures of aromatics and non-aromatics.
2. The amount of non-aromatics dehydrogenated was equivalent to the new aromatics formed.
3. Boiling point of the whole feed was above 343 °C (96 wt% based on simulated distillation).
4. Only 343 °C+ fraction contained aromatics.
5. Overall mass of aromatic or non-aromatic compounds was the sum of mass of carbon, hydrogen, sulfur and nitrogen
6. Remaining non-aromatics in liquid products were all paraffins with H/C atomic ratio of two
7. All nitrogen compounds were contained in aromatics and unreacted.
8. All sulfides in non-aromatics were converted to H<sub>2</sub>S after reaction.

The calculation details are in Appendix A and the results for conversion of non-aromatics after dehydrogenation are shown in Table 4-7.

Table 4-7. Conversion of reactive species versus overall species

| <b>Operation</b> | <b>Non-aromatics in feed after dehydrogenation, g</b> | <b>Non-aromatics in liquid product, g</b> | <b>Conversion of reactive species in HGO in cracking step</b> | <b>Overall mass conversion of whole HGO</b> |
|------------------|---|---|---|---|
| 600 Run1         | 4.163   | 3.355                                     | 0.194   | 0.111                                       |
| 600 Run2         | 3.719   | 2.905                                     | 0.219   | 0.125                                       |
| 600 Run3         | 3.659   | 2.422                                     | 0.338   | 0.188                                       |
| 650 Run1         | 3.493   | 1.757                                     | 0.497   | 0.265                                       |
| 650 Run2         | 3.930   | 1.356                                     | 0.655   | 0.343                                       |
| 650 Run3         | 3.435   | 1.033                                     | 0.699   | 0.375                                       |
| 650 Run4         | 3.457   | 0.945                                     | 0.727   | 0.385                                       |
| 700 Run1         | 3.796   | 0.325                                     | 0.914   | 0.489                                       |
| 700 Run2         | 4.286   | 0.176                                     | 0.959   | 0.559                                       |
| 700 Run3         | 3.867   | 0.016                                     | 0.996   | 0.577                                       |

As compared in Table 4-7, the conversions of reactive species in HGO were much higher than the conversions of the overall mass of HGO measured by simulated distillations. Although the conversions of reactive species were calculated based on the listed assumptions from the data from NMR spectroscopy and simulated distillation, they showed the same trend as conversions of overall HGO and were consistent with operating conditions. At 700 °C and 0.663 s, nearly all the reactive species of HGO were converted, leaving behind unreactive aromatics.

Under the isothermal assumption, the apparent first-order rate constants for conversion of reactive species in HGO were calculated and shown to be statistically constant at a given furnace set temperature. This result is further illustrated in the Arrhenius plot in Figure 4-18.

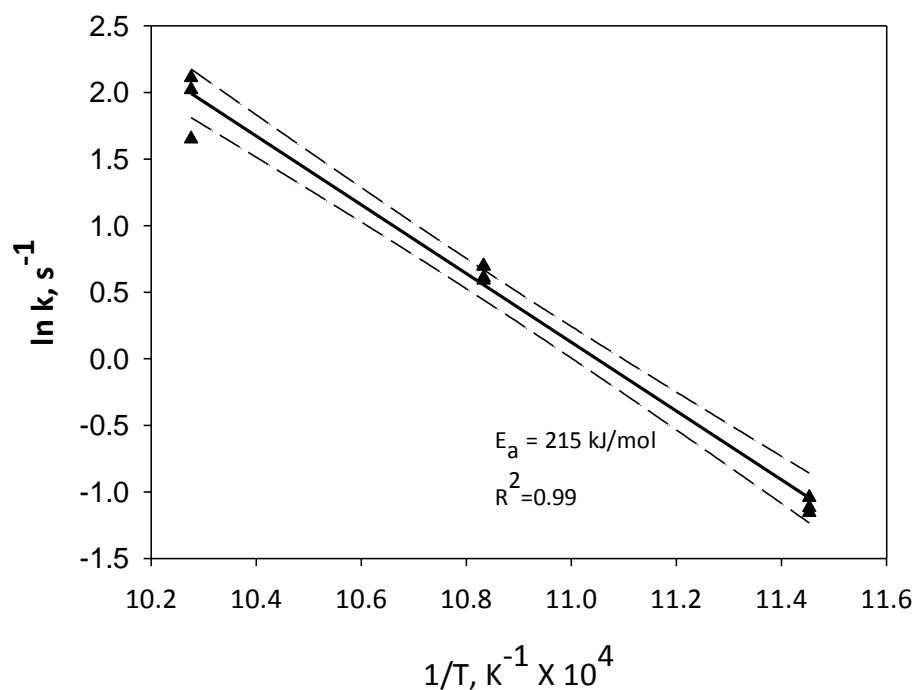


Figure 4-18. Arrhenius plot for conversion of reactive species in heavy gas oil

The data points were fitted well by least-square line with correlation coefficient close to one. The regression equation gave the intercept value of 28.53 with 95 % confidence interval of 25.84 to 31.22 and slope value of -2.58 with 95 % confidence interval of -2.83 to -2.33. The intercept and slope of the linear regression line gave predicted apparent activation energy of  $215 \pm 20 \text{ kJ/mol}$  and pre-exponential factor of  $\exp(28.53 \pm 2.69)$ . These values predicted by isothermal assumption were in agreement with the range for gas oils reported in the literature (Zou et al., 1993; Su et al., 1997). The predicted activation energy was comparable with the value (238 kJ/mol) from thermal steam cracking of pure n-hexadecane (Depeyre et al., 1985) and the value (223 kJ/mol) from thermal deposition of dodecylbenzene (Behar et al., 2002).

The non-isothermal part of the reactor had an effect on the calculated activation energy. For the best estimates of the kinetics, the reactor was analyzed at non-isothermal conditions. The relationship between mass flow rate of reactive species in HGO and reactor position was:

$$\frac{dF_{\text{reactive species}}}{dx} = -A \exp\left(\frac{-E_a}{RT_m}\right) \times \frac{T_0 F_{\text{reactive species}}}{T_m v_0} \times A_R \quad (4.27)$$

$$T_m = T_s - (T_s - T_{m,i}) \exp\left(-\frac{\pi D \bar{h}}{m C_p} x\right) \quad (4.28)$$

where  $F_{\text{reactive species}}$  is the mass flow rate of reactive species in HGO after dehydrogenation.

This differential equation was solved by Runge-Kutta method using ODE 45 in MATLAB, from the nozzle tip inlet (0.027 or 0.034 m) to reactor outlet (0.915 m). The initial value was the mass flow rate of reactive species at nozzle tip position, which was calculated as the mass of reactive species after dehydrogenation in feed over total operation time (28.208 min). The mass flow rate as a function of position can be obtained by plotting and fitting various data points. For instance, the solution of reaction at 600 °C and 0.682 s is illustrated in Figure 4-19, given the estimated pre-exponential factor and activation energy under isothermal assumption

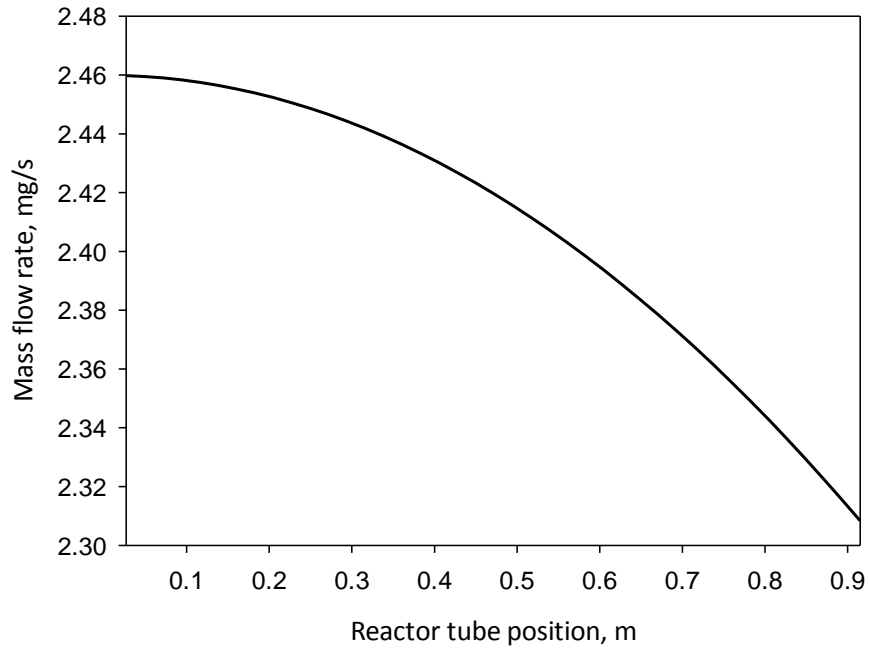


Figure 4-19. Mass flow rate of reactive species versus reactor position at operating condition of 600 °C and 0.682 s

With this relationship, the mass flow rates of reactive species at reactor outlet at different operating conditions can be predicted given 2 adjustable parameters in the model: activation energy and pre-exponential factor. The conversions of reactive species after dehydrogenation were subsequently predicted as follows:

$$X_{\text{pred}} = \frac{F_{\text{reactive species in}} - F_{\text{reactive species out}}}{F_{\text{reactive species in}}} \quad (4.29)$$

where  $F_{\text{reactive species in}}$  is the mass flow rate of reactive species in HGO after dehydrogenation at inlet, and  $F_{\text{reactive species out}}$  is the mass flow rate of reactive species in HGO at outlet.

The residual sum of squares was introduced as a measure of the discrepancy between the real data and values predicted by the non-isothermal kinetic model. The conversions of reactive species for all 10 groups of experiments were included in the calculation. The objective function was minimized to estimate the best results of activation energy and pre-exponential factor under non-isothermal condition:

$$RSS = \sum_{i=1}^n (X_{i,\text{pred}} - X_i)^2 \quad (4.30)$$

where  $X_{i,\text{pred}}$  is the predicted conversion by model and  $X_i$  is the conversion from experiments.

Both optimization tools `fminsearch` and `fminsearchbnd` in MATLAB was used to perform the calculation. The estimated activation energy,  $E_a$ , and pre-exponential factor  $A$  from isothermal calculation were input as the starting point. In `fminsearch` without constrains, the minimum value of RSS was 0.0459 corresponding to activation energy of 208 kJ/mol and pre-exponential factor of  $2.48 \times 10^{12}$ . In `fminsearchbnd`, the bounds for  $A$  and  $E_a$  were set as  $10^4$ - $10^{16}$  and 30-350 kJ/mol, respectively. With this constraint, the RSS was minimized to be 0.0561, giving activation energy of 229 kJ/mol and pre-exponential factor of  $3.40 \times 10^{13}$ .

The corrected non-isothermal apparent activation energy was in the same range as the initial value calculated based on isothermal assumption. Consequently, the non-isothermal part of the reactor was not significant in the kinetic study of vapour phase cracking of HGO. The furnace set temperatures can be regarded as reaction temperatures to study kinetics, within the error of the conversion measurements presented in this study.

The Arrhenius plot of our study was compared with cracking of Arab Heavy and Cold Lake bitumen extrapolated over the same temperature range (Figure 4-20).

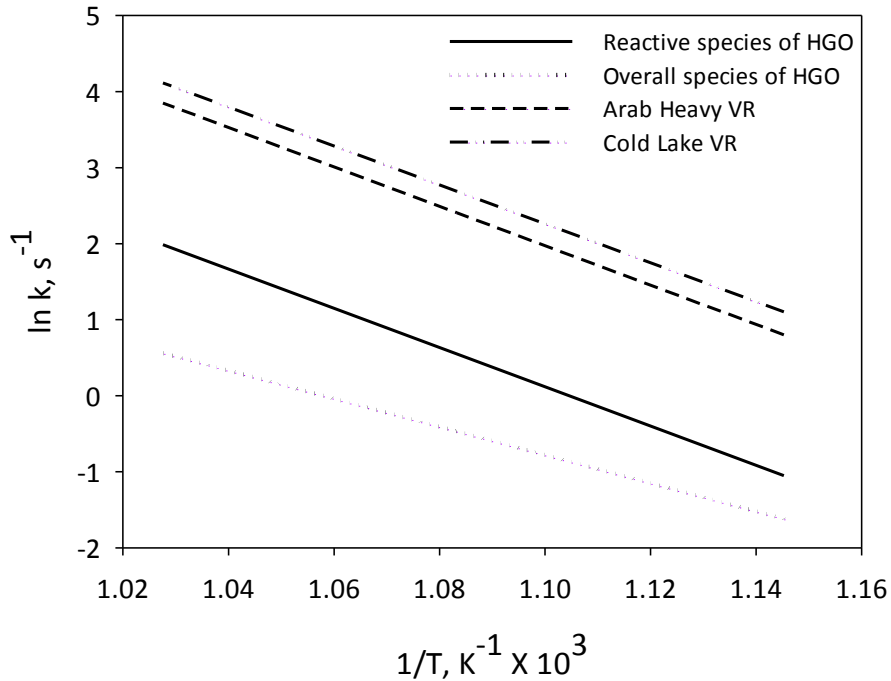


Figure 4-20. Comparison of Arrhenius plot for bitumen-derived heavy gas oil and vacuum residue fractions of bitumens

As illustrated in Figure 4-20, Arab Heavy and Cold Lake vacuum residues show very similar cracking kinetics with  $E_a$  of 212.8-215.5 kJ/mol and  $\log A$  of 13.21-13.24  $s^{-1}$  (Olmstead et al., 1998). Cracking of reactive species in bitumen-derived HGO also gave very similar activation energy. The predicted rate constants are lower than those of vacuum residues. Cracking of overall species of HGO exhibited lower activation energy and the estimated rate constants were also much lower in the same temperature range. The discrepancy can be attributed to the processing history of these oils. Arab Heavy and Cold Lake vacuum residues are the unprocessed virgin mixtures which contain rich amounts of side chains. These reactive materials provided large capacity for cracking

and were able to give full conversion of vacuum residue fraction. Hence, the cracking kinetics of Arab Heavy and Cold Lake VR was literally based on their reactive species. In comparison, bitumen-derived HGO has gone through severe thermal cracking, losing most of the side chains. This explains why the aromatic carbon content of our feed (40 %) was higher than that of vacuum residues (35 %). Moreover, the rest of reactive species were rich in naphthenic groups (Ng et al., 2002) which tended to lose hydrogen to form aromatics very quickly. As a result, the actual content of aromatics in the reaction was even higher, causing a very limited cracking capacity for the overall species of HGO. Research (Gray, 1994; Stangeland et al., 1974; Takeuchi et al., 1983) also shows that crackability tends to increase with molecular weight or boiling range since larger molecules have more bonds which can rupture and increase the probability of breakage. The reactive species of HGO after dehydrogenation were the side chains in vacuum residues that survived in the previous processing. Accordingly, they featured the similar kinetics as unprocessed vacuum residues.

# CHAPTER 5

## Implications and Conclusions

### 5.1 Implications

This study investigates the vapor-phase cracking of aromatic gas oil, which is relevant to both commercial fluid cokers and steam cracking. These data clearly indicate that vapor-phase cracking gives high selectivity for olefins, at the expense of the quality of the liquid product. The activation energies for reactive material in this study were similar to cracking on both the liquid phase and the gas phase in previous studies of vacuum residues and gas oils. The crucial difference is that the high conversions in this study required partitioning of the HGO into reactive species and non-reactive aromatics. This approach follows well established practice in lumped kinetic modeling, since first proposed by Gross et al. in 1974. The results suggest that modeling of cracking at high conversion should allow for the decline in reactivity as aromatics build up in the unconverted feed fraction, and that the difference in selectivity between vapor phase cracking and liquid phase cracking should be taken into account.

The established link between operating conditions and liquid product quality suggests that reducing residence time of vapor in the reactor bed limits the conversion of vapor phase component, and hence increases the hydrogen content of the final liquid product. Higher temperature in the liquid phase would be expected to result in more cracking of volatiles from the coke, which increases the yield of liquid product. However, high temperature accelerates the conversion of vapor phase component to light ends and

the remaining liquid features very high concentration of aromatics and low hydrogen content, as measured by elemental and  $^{13}\text{C}$  NMR analysis. The data from this study allow more systematic analysis of different reactor designs, to determine the best combination of temperature and residence time to obtain the optimal tradeoff between liquid product yield and quality. Temperature is easily adjusted during operation. Residence time can be reduced by either increasing fluidization steam velocity or building a reactor with minimum freeboard volume and with controlled retention of vapor in the fluidized bed. However, these changes may lead to fouling problems due to the liquid feed inside of the reactor, which necessitates further research.

Development of new coking technologies is very promising. One approach is to decouple the liquid phase and vapor phase cracking in coking processes. Vapor phase should be under low temperature and short residence time to minimize the conversion of the evolved components. In contrast, liquid phase favors high temperature and relatively long residence time to give high yield and quality of the liquid product.

Steam cracking of bitumen-derived heavy aromatic gas oil is one of the alternative technologies to increase olefin production. High olefin yield and selectivity was obtained at the highest operating temperature of 700 °C in our experiments. Around 30 % of converted feed was ethylene and propylene. The operating temperature in conventional steam crackers is even higher, which may give higher olefin yield using the same feed. The data show, however, that the liquid at these conditions is highly aromatic, which significantly reduces the reactivity for further cracking and which would limit the incremental yield of olefins from higher conversion. Furthermore, the coke yield in our operating range was below 2 %, which is favorable for steam crackers. Despite these

advantages, some problems still exist. The coke deposition is expected to be severe after a certain period of running and the produced liquid product would be mostly polycyclic aromatics that are of low value. As a result, further comprehensive researches needed to be done to investigate the feasibility of highly aromatic-naphthenic gas oil to feed steam crackers.

## **5.2 Conclusions**

Complete vaporization of bitumen-derived HGO was approached at the reactor inlet by optimizing nozzle tip position and flow rates of helium carrier gas. The reactor temperature profiles within the entire operating range show a rapid temperature increase at the beginning. Nearly isothermal operation was achieved after a very short heating time, by selecting operation with low helium flow rate.

Thermal cracking in vapor phase was shown to give negligible coke yield and high yield of olefins. The discrepancy increased with increase of conversion and was more obvious at higher operating temperature. Most gas products were ethylene, propylene and methane.

The liquid product featured lower hydrogen content and higher aromatic carbon content at higher conversion, which was consistent with formation of hydrogen-rich light ends. Aromatic carbon content exhibited a linear relationship with the conversion.

The apparent first-order rate constants for overall HGO conversion were found to decrease remarkably at high conversion operation, which implies loss of reactivity. The most reactive species such as side chains were reacted initially, leaving unreactive aromatic compounds behind. The yield ratio of aromatic carbon in liquid product was constant at 1.2 even at low conversion, which suggests that formation of new aromatics

by dehydrogenation of naphthenes was very fast in our thermal cracking regime. Based on this observation, a two-step reaction mechanism was proposed in which fast dehydrogenation was followed by slower cracking. Dehydrogenation of naphthenes did not change conversion except leaving a more aromatic starting material for cracking. Thermal cracking of reactive species in HGO fraction after dehydrogenation contributed to all conversion and the apparent first-order activation energy was predicted to be 208 kJ/mol based on full non-isothermal analysis of the reactor.

# BIBLIOGRAPHY

Gray, M. R. Upgrading of Oil Sands Bitumen and Heavy Oil. 2010.

Gray, M. R. Upgrading Petroleum Residues and Heavy Oils. 1994.

Gray, M. R.; Le, T.; McCaffrey, W. C. Coupling of Mass Transfer and Reaction in Coking of Thin Films of an Athabasca Vacuum Residue. *Ind. Eng. Chem. Res.* 2001, 40, 3317-3324.

Rana, M. S.; Samano, V.; Ancheyta, J.; Diaz, J. A. I. A review of recent advances on process technologies for upgrading of heavy oils and residua. *Fuel* 2007, 86, 1216-1231.

Brown, W.; Pinchuk R.; Monaghan G. Benefits from coking of heavy feedstocks.

Wiehe, I. A. *Process Chemistry of Petroleum Macromolecules*. 2008.

Silverman, M. A.; Pavel, S. K.; Hillerman, M. D. HTL Heavy Oil Upgrading-A key solution for heavy oil upstream and midstream operations. *World Heavy Oil Congress*, Edmonton, Alberta, 2011.

Kuhach, J. D.; Koshka, E.; Lin, L.; Pavel, S. K. Maximizing Heavy-Oil Value While Minimizing Environmental Impact with HTL Upgrading of Heavy-to-Light Oil. *World Heavy Oil Congress*, Puerto La Cruz, Venezuela, 2009.

Veith, Edwin J. Performance of a Heavy to Light Crude Oil Upgrading Process. *International Oil Conference and Exhibition*, Veracruz, Mexico, 2007.

Freel, B. and Graham, R. G. Internal Reports, Ensyn Group Ltd, 2002-2005.

Vogitzis, A. L.; Briens, C. L.; M. A. B. Selected Applications of Ultra-Rapid Fluidized Reactors. In *Ultrapyrolysis of Heavy Oils and Ultra-Rapid Catalytic Cracking*. AIChE, New York, 1989.

Gray, M. R. Fundamentals of Bitumen Coking Processes Analogous to Granulations: A Critical Review. *Can. J. Chem. Eng.* 2002, 80, 393-401.

Gray, M. R.; Le, T.; Wu, X. A. Role of Pressure in Coking of Thin Films of Bitumen. *Can. J. Chem. Eng.* 2007, 85, 773-780.

Chaudhuri, U. R. *Fundamentals of Petroleum and Petrochemical Engineering*. 2011.

Greene R. B. Vacuum Gas Oil Cracking. *Manufacture of Ethylene and Higher Olefins*. 1969, 19 (1), 121-128.

- Kanda, W.; Siu, I.; Adjaye, J.; Nelson, A. E.; Gray, M. R. Inhibition and Deactivation of Hydrodenitrogenation (HDN) Catalysts by Narrow-Boiling Fractions of Athabasca Coker Gas Oil. *Energy Fuels*, 2004, 18, 539-546.
- Yui, S. M. Hydrotreating of a Bitumen-Derived Coker HGO and Evaluation of Hydrotreated HGOs as Potential FCC Feeds Using Microactivity Test Unit. *Energy Fuels*, 1995, 9, 665-672.
- Strausz, O. P.; Lown, E. M. *The Chemistry of Alberta Oil Sands Bitumens and Heavy Oils*. 2003.
- Wiehe, I. A. The Pendant-Core Building Block Model of Petroleum Residua. *Energy Fuels*, 1994, 8, 536-544.
- Dickie, J. P.; Yen, T. F. Macrostructures of Asphaltic Fractions by Various Instrumental Methods. *Anal. Chem.* 1967, 39, 1847-1852.
- Sheremata, J. M.; Gray, M. R.; Dettman, H. D.; McCaffrey, W. C. Quantitative Molecular Representation and Sequential Optimization of Athabasca Asphaltenes. *Energy Fuels*, 2004, 18, 1377-1384.
- Gray, M. R. Consistency of Asphaltene Chemical Structures with Pyrolysis and Coking Behavior. *Energy Fuels*, 2003, 17, 1566-1569.
- Strausz, O. P.; Mojelsky, T. W.; Lown, E. M. The Molecular Structure of Asphaltene: An Unfolding Story. *Fuel*, 1992, 71 (12), 1355-1363.
- Rice, F. O.; Herzfeld, K. F. *J. Chem. Soc.* 1934, 56 (1), 284-289.
- Kossiakoff, A.; Rice, F. O. *J. Am. Chem. Soc.* 1943, 65, 590-595.
- Lamarca, C.; Libanatic, C.; Klein, M. T.; Cronauer, D. C. *Energy Fuels* 1993, 7, 473-478.
- Gray, M. R.; McCaffrey, W. C. Role of Chain Reactions and Olefins Formation in Cracking, Hydroconversion, and Coking of Petroleum and Bitumen Fractions. *Energy Fuels*, 2002, 16, 756-766.
- Wu, G.; Katsumura, Y.; Matsuura, C.; Ishigure, K. Comparison of Liquid-Phase and Gas-Phase Pure Thermal Cracking of n-Hexadecane. *Ind. Eng. Chem. Res.* 1996, 35, 4747-4754.
- Ford, T. J. Liquid-Phase Thermal Decomposition of Hexadecane: Reaction Mechanisms. *Ind. Eng. Chem. Fundam.* 1996, 25, 240-243.
- Fabuss, B. M.; Smith, J. O.; Lait, S. R.; Borsanyi, A. S. Rapid Thermal Cracking of n-Hexadecane At Elevated Pressures. *Ind. Eng. Chem. Process Des. Dev.* 1962, 1 (4), 293-299.

Watanabe, M.; Tsukagoshi, M.; Hirakoso, H.; Adschiri, T.; Arai, K. Kinetics and Product Distribution of n-Hexadecane Pyrolysis. *AIChE J.* 2000, 46 (4), 843-856.

Khorasheh F.; Gray, M. R. High-Pressure Thermal Cracking of n-Hexadecane. *Ind. Eng. Chem. Res.* 1993, 32, 1853-1863.

Khorasheh F.; Gray, M. R. High-Pressure Thermal Cracking of n-Hexadecane in Tetralin. *Ind. Eng. Chem. Res.* 1993, 7, 960-967.

Khorasheh, F.; Gray, M. R. High-Pressure Thermal Cracking of n-Hexadecane in Aromatic Solvents. *Ind. Eng. Chem. Res.* 1993, 32, 1864-1876.

Jackson, K. J.; Buranham, A. K.; Braun, R. L.; Kanauss, K. G. Temperature and Pressure Dependence of n-Hexadecane Cracking. *Orf. Geochem.* 1995, 23 (10), 941-953.

Fairburn, J. A.; Behie, L. A.; Svrcek, W. Y. Ultrapyrolysis of n-Hexadecane in a Novel Micro-Reactor. *Fuel* 1990, 69, 1537-1545.

Depeyre, D.; Flicoteaux, C.; Chardaire, C.; Pure n-Hexadecane Thermal Steam Cracking. *Ind. Eng. Process Des. Dev.* 1985, 24, 1251-1258.

Zhou, P.; Hollis, O. L.; Crynes, B. L. Thermolysis of Higher Molecular Weight Straight-Chain Alkanes (C9-C22). *Ind. Eng. Chem. Res.* 1987, 26 (4), 846-852.

Doue, F.; Guiochon, G. The Formation of Alkanes in the Pyrolysis of n-Hexadecane: Effect of an Inert Gas on the Decomposition of Alkyl Radicals. *Can. J. Chem.* 1969, 47 (18), 3477-3480.

Rebick, C. H<sub>2</sub>S Catalysis of n-Hexadecane Pyrolysis. *Ind. Eng. Chem. Fundam.* 1981, 20, 54-59.

Zhorov, Yu. M.; Volokhova, G. S. Influence of Aromatic Hydrocarbons on Pyrolysis. I. M. Gubkin Moscow Institute of the Petrochemical and Gas Industry. 1980, 8, 11-13.

Billaud, F.; Berthelin, M.; Freund, E. Thermal Cracking of Vacuum Distillates. *J. Anal. App. Pyro.* 1986, 139-151.

Depeyre, D.; Flicoteaux, C.; Arbabzadeh, F.; Zabaniotou, A. Modeling of Thermal Steam Cracking of an Atmospheric Gas Oil. *Ind. Eng. Chem. Res.* 1989, 28, 967-976.

Hirato, M.; Yoshioka, S.; Tanaka, M. Gas-Oil Pyrolysis by Tubular Reactor and its Simulation Model of Reaction. *Hitachi Rev.* 1971, 20 (8), 326-334.

Su, J.; Yang, J.; Wang, H. Kinetic Investigation of Pyrolysis for Daqing Light Gas Oil. *Petr. Sci. Tech.* 1997, 15 (9&10), 823-837.

Zou, R.; Lou, Q.; Mo, S.; Feng, S. Study on a Kinetic Model of Atmospheric Gas Oil Pyrolysis and Coke Deposition. *Ind. Eng. Chem. Res.* 1993, 32, 843-847.

Meng, X.; Xu, C.; Gao, J. Li, L. Studies on Catalytic Pyrolysis of Heavy Oils: Reaction Behaviors and Mechanistic Pathways. *App. Cat. A: General*, 2005, 294, 168-176.

Wang, G.; Liu, Y.; Wang, X.; Xu, C.; Gao, J. Studies on the Catalytic Cracking Performance of Coker Gas Oil. *Energy Fuels* 2009, 23, 1942-1949.

Weekman, VM. A Model of Catalytic Cracking Conversion in Fixed, Moving and Fluid-Bed Reactors. *Ind. Engng. Chem. Prod. Res. Dev.* 1968, 7: 90-5.

Mohammad, A. A. Kinetic Modeling of High-Severity Fluidized Catalytic Cracking. *Fuel* 2003, 82, 1113-1118.

Katica, S.; Zoran, G.; Marko, M. Modeling of Gas Oil Catalytic Cracking in a Fixed Bed Reactor Using a Five-Lump Kinetic Model. *Chem. Eng. Comm.* 2010, 197, 275-288.

Jorge, A.; Felipe, L.; Enrique, A.; 5-Lump Kinetic Model for Gas Oil Catalytic Cracking. *App. Cat. A: General* 1999, 177, 227-235.

Li, L.; Wang, G.; Meng, X.; Xu, C.; Gao, J. Catalytic Pyrolysis of Gas Oil Derived from Canadian Oil Sands Bitumen. *Ind. Eng. Chem. Res.* 2008, 47, 710-716.

Meng, X.; Xu, C.; Li, L.; Gao, J. Studies on the Kinetics of Heavy Oil Catalytic Pyrolysis. *Ind. Eng. Chem. Res.* 2003, 42, 6012-6019.

Meng, X.; Xu, C.; Li, L.; Gao, J. Kinetics of Catalytic Pyrolysis of Heavy Gas Oil Derived from Canadian Synthetic Crude Oil. *Energy Fuels* 2011, 25, 3400-3407.

Rahmani, S.; McCaffrey, W. C.; Dettman, H. D.; Gray, M. R. Coking Kinetics of Asphaltenes as a Function of Chemical Structure. *Energy Fuels* 2003, 17, 1048-1056.

Gray, M. R.; Jokuty, P.; Yeniova, H.; Nazarewycz, L.; Wanke, S. E.; Achia, U.; Krzywicky, A.; Sanford, E. C; Sy, O. K. Y. The Relationship between Chemical Structure and Reactivity of Alberta Bitumens. *Can. J. Chem. Eng.* 1991, 69, 833-843.

Nagaishi, H.; Chan, E. W.; Sanford, E. C.; Gray, M. R. Kinetics of High-Conversion Hydrocracking of Bitumen. *Energy Fuels* 1997, 11, 402-410.

Dupain, X.; Gamas, E. D.; Madon, R.; Kelkar, C. P.; Makkee, M. Moulijn, J. A. Aromatic Gas Oil Cracking under Realistic FCC Conditions in a Microriser Reactor. *Fuel* 2003, 82, 1559-1569.

Danial-Fortain, P.; Gauthier, T.; Merdrignac, I.; Budzinski, H. Reactivity Study of Athabasca Vacuum Residue in Hydroconversion Conditions. *Catalysis Today* 2010, 150, 255-263.

Ho, T. C.; Aris, R. On Apparent Second-order Kinetics. *AIChE J.* 1987, 33, 1050.

Gauthier, T.; Heraud, J. P.; Kressmann, S.; Verstraete, J. *Chem. Eng. Sci.* 2007, 62, 5409.

Weekman, Vern W. *Lumps, Models, and Kinetics in Practice.* 1979.

Isabelle, P.; David, N.; Michel, F.; Jean, R. B. Kinetic Model Based on a Molecular Description for Catalytic Cracking of Vacuum Gas Oil. *Chem. Eng. Sci.* 1994, 49 (24A), 4249-4246.

Gross; Benjamin, Jacob; Solomon, M.; Nace; Donald, M.; Voltz; Sterling, E. Simulation of Catalytic Cracking Process. US Patent 4,187,548, Filed May, 1974; granted February 5, 1980.

Vafi, K. High Temperature Thermal Cracking of Bitumen. Dissertation. 2012

Reyniers, G. C.; Froment, G. F. Coke Formation in the Thermal Cracking of Hydrocarbons. 4. Modeling of Coke Formation in Naphtha Cracking. *Ind. Eng. Chem. Res.* 1994, 33, 2584-2590.

Albright, L. F.; Marek, J. C. Mechanistic Model for Formation of Coke in Pyrolysis Units Producing Ethylene. *Ind. Eng. Chem. Res.* 1988, 27, 755-759.

Ng, S.; Zhu, Y.; Humphries, A.; Zheng, L.; Ding, F.; Gentzis, T.; Charland, J.; Yui, S. FCC Study of Canadian Oil-Sands Derived Vacuum Gas Oils. 1. Feed and Catalyst Effects on Yield Structure. *Energy Fuels* 2002, 16, 1196-1208.

Woods, J. R.; Pleizier, G. P.; Kotlyar, L. S.; Sparks, B. D.; Adjaye, J.; Chung, K. H. Characterization of a Coker Gas Oil Fraction from Athabasca Oil Sands Bitumen. *Fuel* 2004, 83, 1907-1914.

Zou, R.; Lou, Q.; Mo, S.; Feng, S. Study on a Kinetic Model of Atmospheric Gas Oil Pyrolysis and Coke Deposition. *Ind. Eng. Chem. Res.* 1993, 32, 843-847.

Su, J.; Yang, J.; Wang, H. Kinetic Investigation of Pyrolysis for Daqing Light Gas Oil. *Petr. Sci. Tech.* 1997, 15 (9&10), 823-837.

Behar, F.; Lorant, F.; Budzinski, H.; Desavis, E. Thermal Stability of Alkylaromatics in Natural Systems: Kinetics of Thermal Decomposition of Dodecylbenzene. *Energy Fuels.* 2002, 16, 831-841.

Olmstead, W.; Freund, H. Thermal Conversion Kinetics of Petroleum Residua. In *AIChE Spring Meeting, New Orleans, LA, 1998.*

Stangeland, B. E. A Kinetic Model for the Prediction of Hydrocracker Yields. *Ind. Eng. Chem. Process Des. Dev.* 1974, 13, 71-76.

Takeuchi, C.; Fukui, Y.; Nakamura, M.; Shiroto, Y. Asphaltene Cracking in Catalytic Hydrotreating of Heavy Oils. 1. Processing of Heavy Oils by Catalytic Processing and Solvent Deasphalting. *Ind. Eng. Chem. Process. Dev.* 1983, 22, 236-242.

# APPENDIX A

## Calculation Details on Conversion of Reactive Species

For the conversion of reactive non-aromatics after dehydrogenation step:

$$X_{\text{NA}} = \frac{m_{343\text{ }^{\circ}\text{C}+\text{ NA in feed}} - m_{343\text{ }^{\circ}\text{C}+\text{ NA in liquid product}}}{m_{343\text{ }^{\circ}\text{C}+\text{ NA in feed}} \quad (\text{A.1})$$

The amount of HGO fraction converted on the numerator is contributed by the amount of non-aromatics converted in the cracking step.

$$\Delta m_{343\text{ }^{\circ}\text{C}+\text{ NA}} = m_{343\text{ }^{\circ}\text{C}+\text{ NA in feed}} - m_{343\text{ }^{\circ}\text{C}+\text{ NA in liquid product}} \quad (\text{A.2})$$

$$\Delta m_{343\text{ }^{\circ}\text{C}+} = m_{343\text{ }^{\circ}\text{C}+\text{ in feed}} - m_{343\text{ }^{\circ}\text{C}+\text{ in liquid product}} \quad (\text{A.3})$$

$$\Delta m_{343\text{ }^{\circ}\text{C}+\text{ NA}} = \Delta m_{343\text{ }^{\circ}\text{C}+} \quad (\text{A.4})$$

The amount of non-aromatics in 343 °C+ fraction of the feed after dehydrogenation can be calculated given elemental composition and aromatic carbon content information.

$$m_{343\text{ }^{\circ}\text{C}+\text{ NA in feed after -H}} = m_{343\text{ }^{\circ}\text{C}+\text{ NA in feed}} - m_{343\text{ }^{\circ}\text{C}+\text{ NA -H}} \quad (\text{A.5})$$

$m_{343\text{ }^{\circ}\text{C}+\text{ NA in feed}}$  is the original amount of non-aromatics in 343 °C + fraction of the feed;

$m_{343\text{ }^{\circ}\text{C}+\text{ NA -H}}$  is the amount of non-aromatics that is dehydrogenated, which is equal to

the amount of new aromatics that is created.

$$m_{343\text{ }^{\circ}\text{C}+\text{NA}-\text{H}} = m_{\text{A in liquid product}} - m_{\text{A in feed}} \quad (\text{A.6})$$

$m_{\text{A in liquid product}}$  is the amount of aromatics in liquid product;  $m_{\text{A in feed}}$  is the amount of aromatics in feed. Aromatics are primarily in 343 °C + fraction of feed. Therefore,

$$m_{\text{A in feed}} = m_{343\text{ }^{\circ}\text{C}+\text{A in feed}} \quad (\text{A.7})$$

$$m_{343\text{ }^{\circ}\text{C}+\text{NA in feed}} + m_{343\text{ }^{\circ}\text{C}+\text{A in feed}} = m_{343\text{ }^{\circ}\text{C}+\text{in feed}} \quad (\text{A.8})$$

Over 96 wt % of feed is in the 343 °C + fraction:  $m_{343\text{ }^{\circ}\text{C}+\text{in feed}} \approx m_{\text{feed}}$ , therefore,

$$m_{343\text{ }^{\circ}\text{C}+\text{NA in feed after -H}} = m_{\text{feed}} - m_{\text{A in liquid product}} \quad (\text{A.9})$$

$m_{\text{A in liquid product}}$  is the amount of aromatics in liquid product, which is not easy to be calculated. The mixture consists of aromatics and non-aromatics.

$$m_{\text{A in liquid product}} = m_{\text{liquid product}} - m_{\text{NA in liquid product}} \quad (\text{A.10})$$

The amount of non-aromatics in liquid product can be predicted by elemental composition.

$$m_{\text{NA in liquid product}} = m_{\text{NA carbon}} + m_{\text{NA hydrogen}} + m_{\text{NA sulfur}} + m_{\text{NA nitrogen}} \quad (\text{A.11})$$

All easily reacted sulfides are exhausted during the reaction and non-aromatics do not contain nitrogen compounds. The non-aromatics feature CH<sub>2</sub> structure, giving H/C atomic ratio of 2.

$$m_{\text{NA in liquid product}} = \frac{14}{12} m_{\text{NA carbon in liquid product}} \quad (\text{A.12})$$

The amount of non-aromatic carbon in liquid product can be decided by total carbon content and aromatic carbon content measured by elemental analysis and  $^{13}\text{C}$  NMR, respectively.

$$m_{\text{NA carbon in liquid product}} = m_{\text{liquid product}} \times \text{carbon wt\%} \times (1 - \text{aromaticity}) \quad (\text{A.13})$$

Therefore,

$$m_{343\text{ }^{\circ}\text{C}+\text{NA in feed after -H}} = m_{\text{feed}} - m_{\text{Liquid product}} + \frac{14}{12} m_{\text{Liquid product}} \times \text{carbon wt\%} \times (1 - \text{aromaticity}) \quad (\text{A.14})$$

Given by simulated distillation,

$$m_{343\text{ }^{\circ}\text{C}+\text{NA in feed}} - m_{343\text{ }^{\circ}\text{C}+\text{NA in liquid product}} = m_{\text{feed}} \times w_{\text{HGO in feed}} - m_{\text{Liquid product}} \times w_{\text{HGO in liquid product}} \quad (\text{A.15})$$

Recovered liquid product yield was defined as

$$Y = \frac{m_{\text{liquid product}}}{m_{\text{feed}}} \quad (\text{A.16})$$

Accordingly, conversion can be expressed by measurable experimental data as

$$X_{\text{NA}} = \frac{w_{\text{HGO in feed}} - w_{\text{HGO in liquid product}}}{(1 - Y) + \frac{14}{12} \times Y \times C\% \times (1 - \text{aromaticity})} \quad (\text{A.17})$$

# APPENDIX B

## GC Calculations and Chromatographs

### 1. Non-Condensed Gas Products

Methane, ethane and ethylene are the possible non-condensed gas products. They were identified by comparing the unknown peaks with those known peaks in calibration table. If the retention times are close, the unknown peaks were identified as those components. The mass concentration of methane was calculated based on two points external standard method. The response factor was calculated from the concentrations of two methane standards with 10.4 ppm and 100 ppm and their corresponding peak areas. The mass concentrations of ethane and ethylene were calculated based on single point external standard method. The response factors were calculated by the same way.

$$f_i = \frac{A_i^R}{m_i^R} \quad (\text{B.1})$$

where  $f_i$  is the response factor of the certain component;  $A_i^R$  is the peak area of the standard;  $m_i^R$  is the mass concentration of the standard (mg/L). With the response factor for each component, the mass concentration of each gas sample can be calculated as

$$m_i = \frac{A_i}{f_i} \quad (\text{B.2})$$

where  $A_i$  is the peak area of the unknown sample;  $m_i$  is the mass concentration of the sample (mg/L). The non-condensed gases were analyzed approximately every 5 minutes during the reaction, giving averaged mass concentration values. The absolute amount of each component was calculated as

$$M_i = m_i \times F \times t \quad (\text{B.3})$$

where  $M_i$  is the absolute amount of component  $i$ ;  $m_i$  is the corresponding mass concentration;  $F$  is the volume flow rate of helium sweep gas at room temperature;  $t$  is the total reaction time (28.2 min). The following chromatograph shows one of the analysis results at 600 Run1.

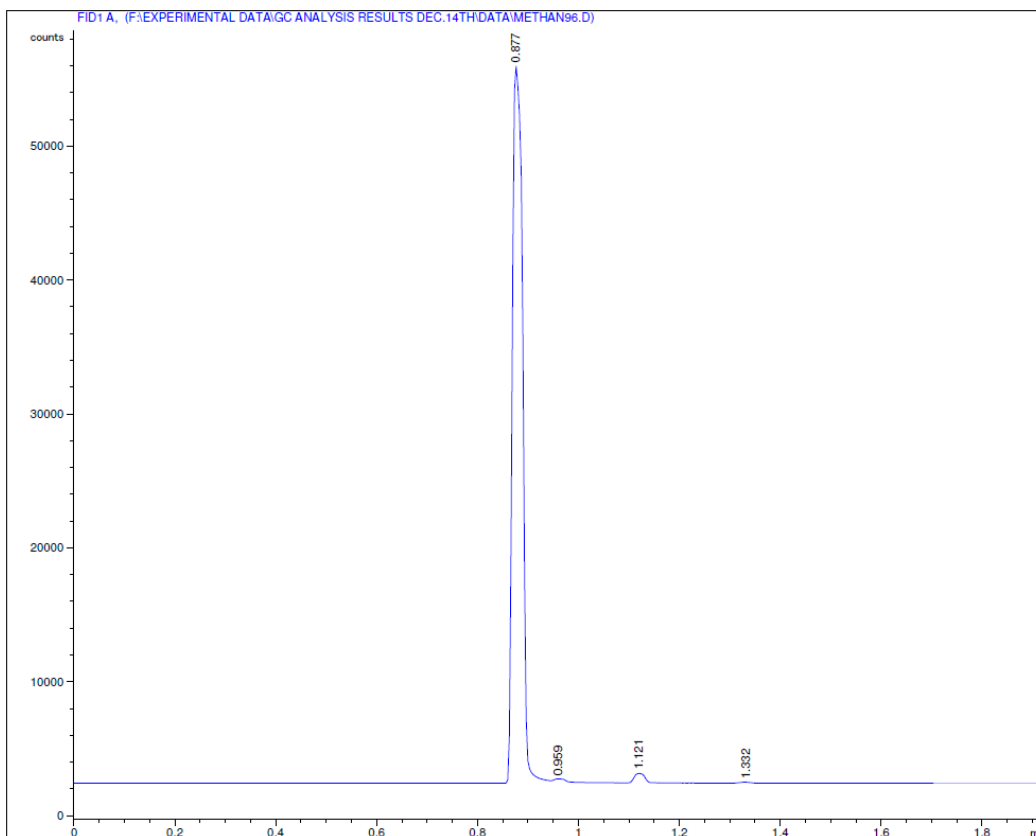


Figure B-1. GC chromatograph for non-condensed gases

## 2. Condensed Gas Products

Condensed gas products contain gases with carbon number from 1 to 6. They were also identified in the same way as non-condensed gas products. However, those peaks representing higher carbon number components cannot be identified very precisely due to their low concentrations. The mass concentrations of all components were determined by single point external standard method based on their response factors and peak areas. The absolute amount of each component was calculated as

$$M_{i,n} = m_{i,n} \times V_n \quad (\text{B.4})$$

where subscript  $n$  represents the number of gas bag;  $M_{i,n}$  is the absolute amount of component  $i$  in gas bag  $n$ ;  $m_{i,n}$  is the corresponding mass concentration;  $V_n$  is the volume of gas bag  $n$ . The gas bag was connected to the condensers to collect the gas products, which brought the inside pressure down. The initial pressure of the enclosed condensers was  $p_i$  and the final pressure of the entire system of condensers connecting with gas bag was  $p_f$ . The system temperature was unchanged and the total of gases was fixed before and after connecting gas bag. Therefore, according to ideal gas law

$$\frac{p_i}{p_f} = \frac{V_{\text{total}}}{V_{\text{cond}}} \quad (\text{B.5})$$

where  $V_{\text{cond}}$  is the total volume of all condensers (1.614 L);  $V_{\text{total}}$  is the total volume of condensers and gas bag. The volume of each gas bag can be calculated as

$$V_n = \frac{p_i}{p_f} V_{\text{cond}} - V_{\text{cond}} \quad (\text{B.6})$$

The total amount of each gas component is the sum of them in different gas bags.

$$M_i = \sum M_{i,n} \quad (\text{B.7})$$

The following chromatographs show the analysis results of gas samples collected in four gas bags at 600 Run1.

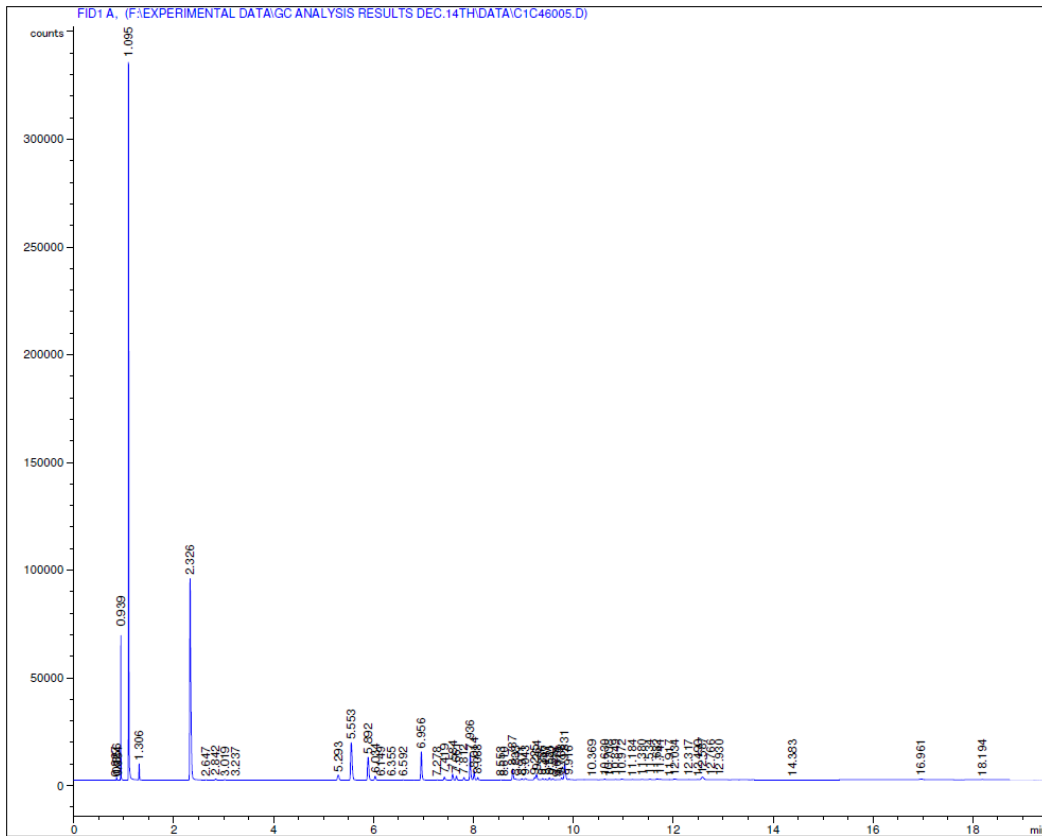


Figure B-2.GC chromatograph for condensed gases collected in gas bag 1 at 600 Run1

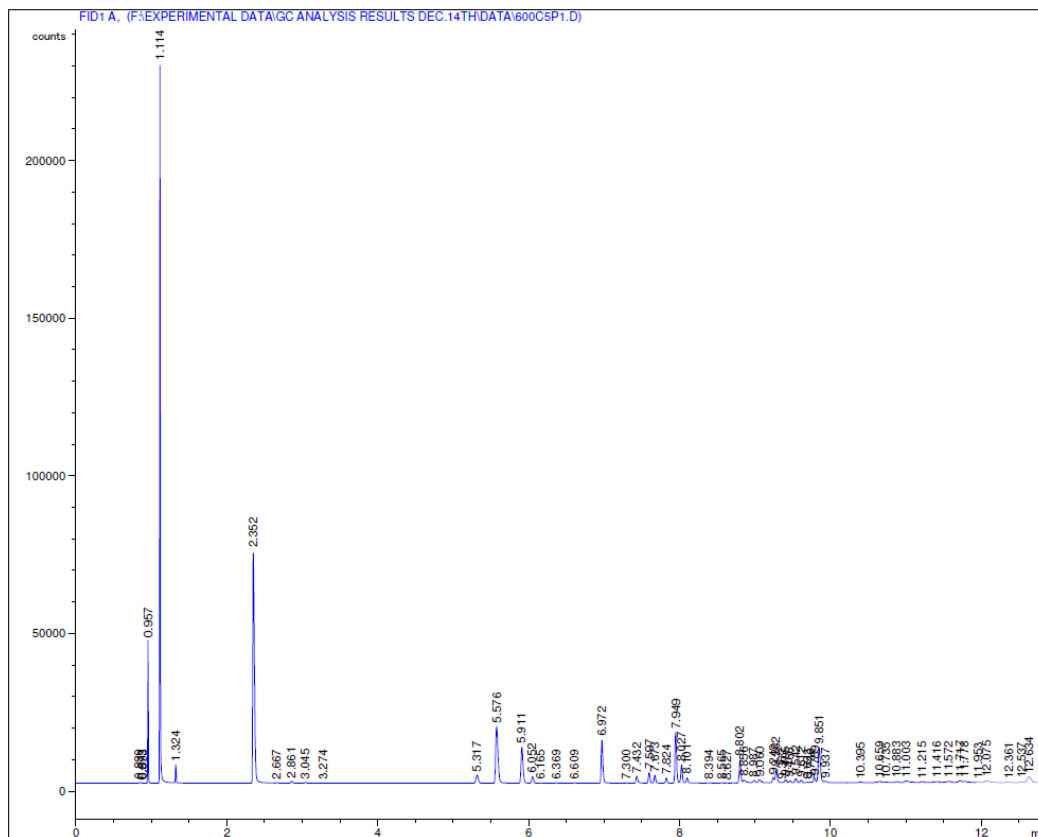


Figure B-3. GC chromatogram for condensed gases collected in gas bag 2 at 600 Run1

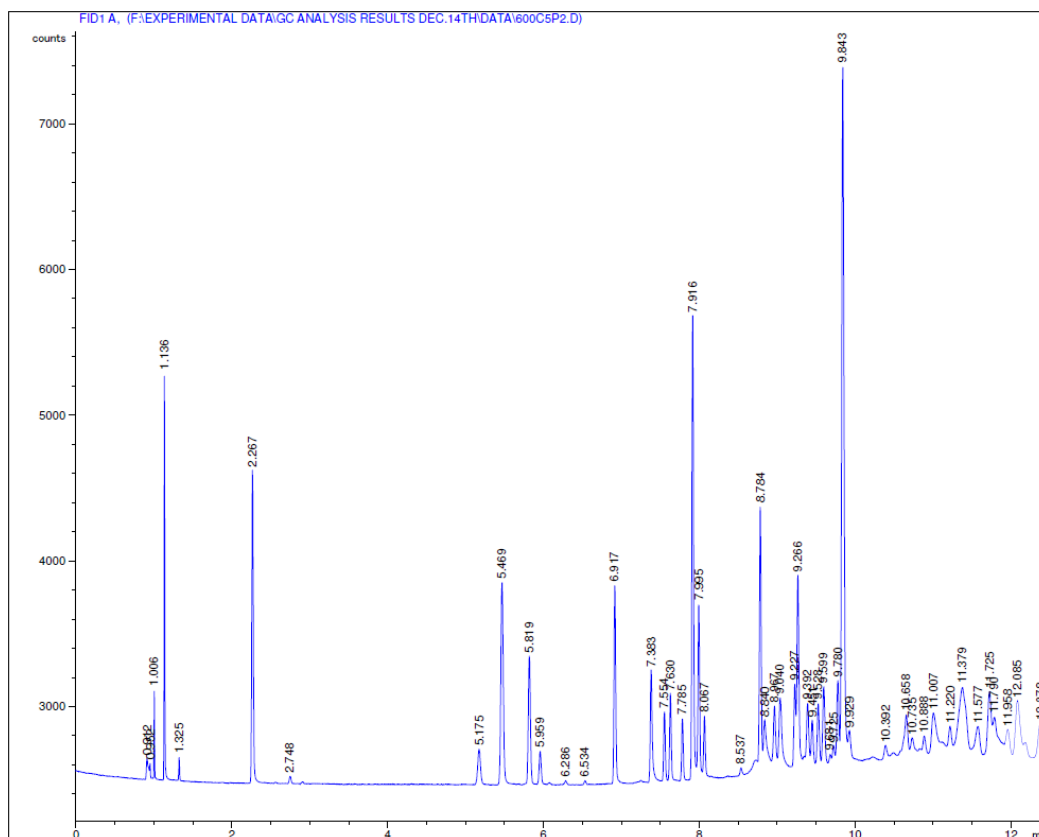


Figure B-4. GC chromatograph for condensed gases collected in gas bag 3 at 600 Run1

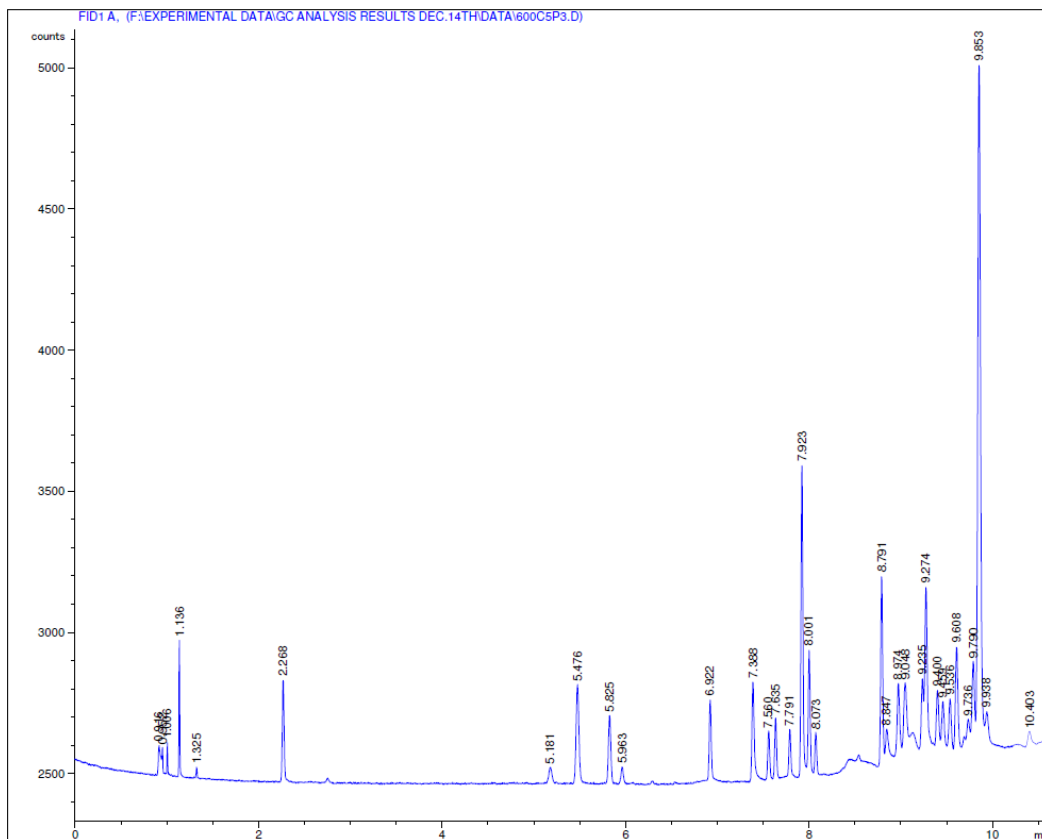


Figure B-5. GC chromatograph for condensed gases collected in gas bag 4 at 600 Run1

# APPENDIX C

## Simulated Distillation Results

### 1. ASTM D2887 Results

Table C-1. Summary of ASTM D2887 simulated distillation results

| Sample   | Boiling fractions, wt% |             |         |
|----------|------------------------|-------------|---------|
|          | 343 °C-                | 343-524 °C+ | 524 °C+ |
| Feed     | 4                      | 79          | 17      |
| 600 Run1 | 10                     | 77          | 13      |
| 600 Run2 | 10                     | 77          | 13      |
| 600 Run3 | 12                     | 77          | 11      |
| 650 Run1 | 16                     | 74          | 10      |
| 650 Run2 | 20                     | 71          | 9       |
| 650 Run3 | 19                     | 72          | 9       |
| 650 Run4 | 21                     | 70          | 9       |
| 700 Run1 | 26                     | 67          | 7       |
| 700 Run2 | 25                     | 67          | 8       |
| 700 Run3 | 28                     | 64          | 8       |

ASTM D2886  
600 °C set point

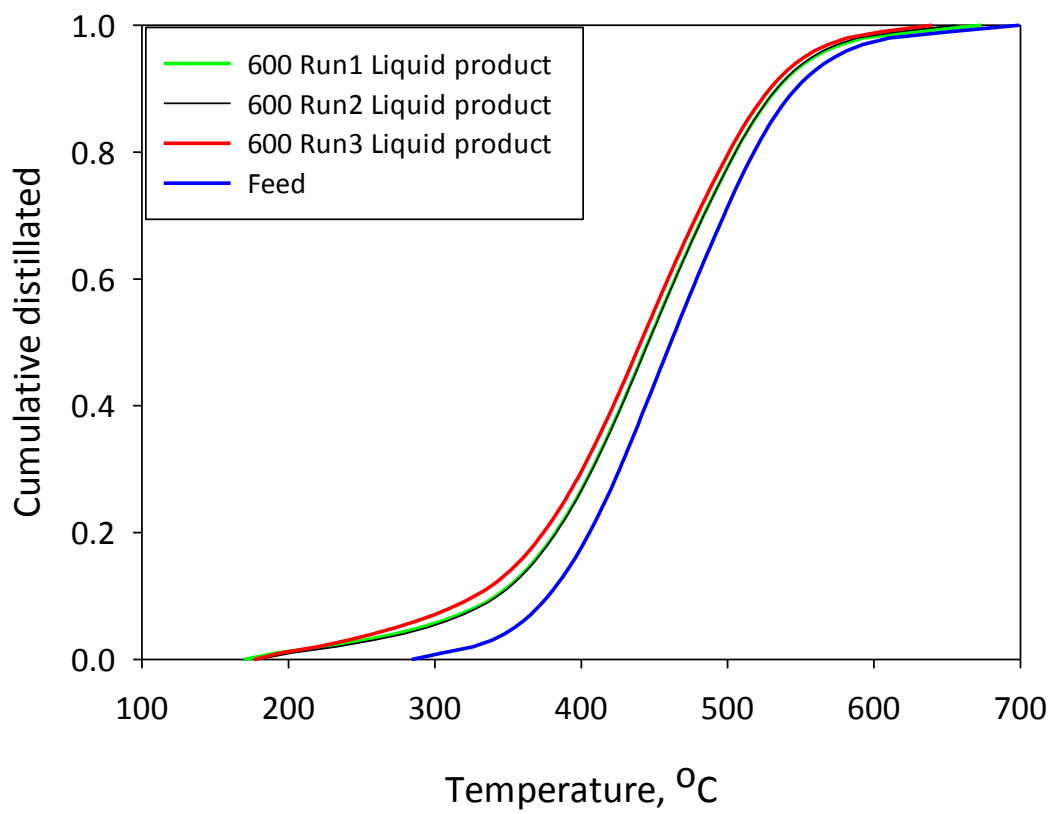


Figure C-1. Boiling curves for bitumen derived heavy gas oil feed and liquid products at 600 °C furnace set point by ASTM D 2886 method

ASTM D2886  
650 °C set point

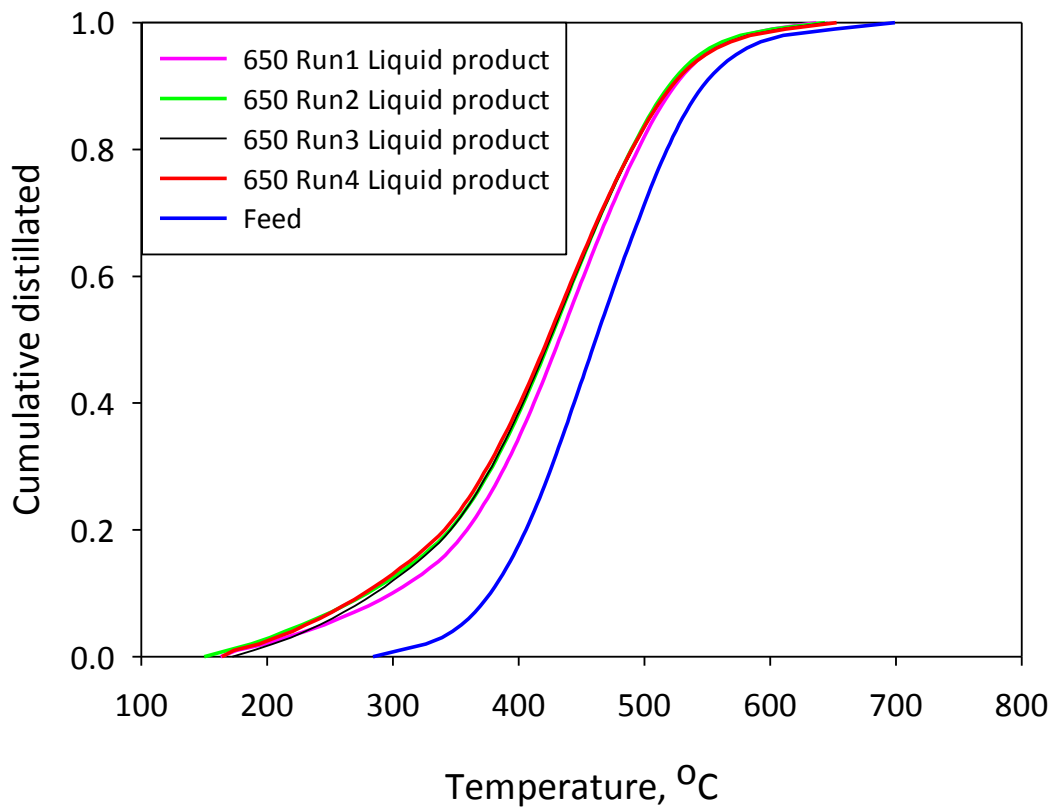


Figure C-2. Boiling curves for bitumen derived heavy gas oil feed and liquid products at 650 °C furnace set point by ASTM D 2886 method

ASTM D2886  
700 °C set point

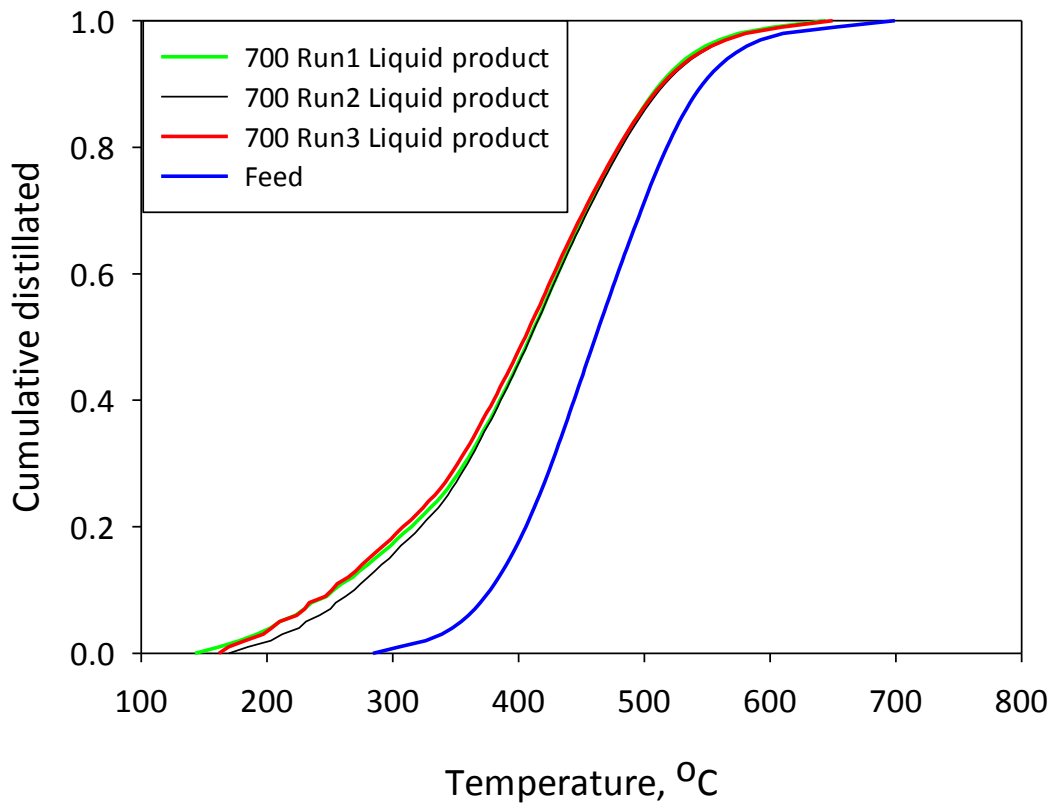


Figure C-3. Boiling curves for bitumen derived heavy gas oil feed and liquid products at 700 °C furnace set point by ASTM D 2886 method

## 2. ASTM D6352 Results

Table C-2. Summary of ASTM D6352 simulated distillation results

| Sample   | Boiling fractions, wt% |             |         |
|----------|------------------------|-------------|---------|
|          | 343 °C-                | 343-524 °C+ | 524 °C+ |
| Feed     | 5                      | 79          | 16      |
| 600 Run1 | 11                     | 78          | 11      |
| 600 Run2 | 11                     | 78          | 11      |
| 600 Run3 | 12                     | 70          | 18      |
| 650 Run1 | 21                     | 70          | 9       |
| 650 Run2 | 19                     | 67          | 14      |
| 650 Run3 | 18                     | 64          | 8       |
| 650 Run4 | 16                     | 69          | 15      |
| 700 Run1 | 24                     | 61          | 15      |
| 700 Run2 | 23                     | 59          | 18      |
| 700 Run3 | 25                     | 57          | 18      |

ASTM D6352  
600 °C set point

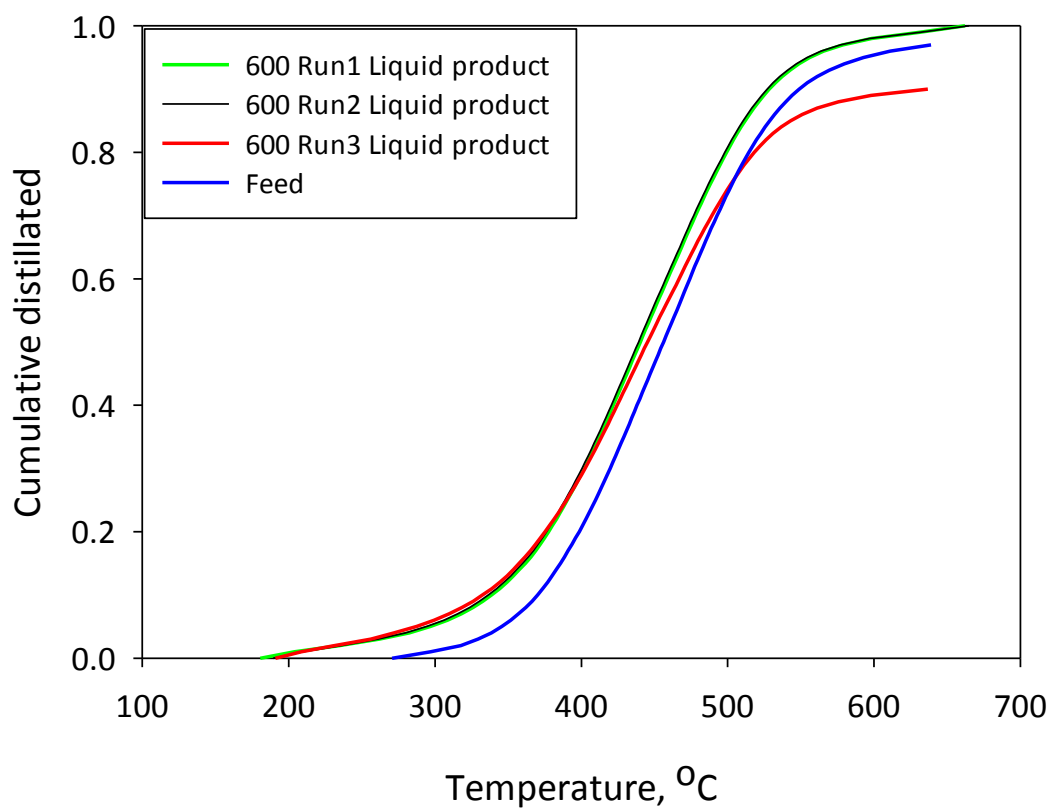


Figure C-4. Boiling curves for bitumen derived heavy gas oil feed and liquid products at 600 °C furnace set point by ASTM D 6352 method

ASTM D6352  
650 °C set point

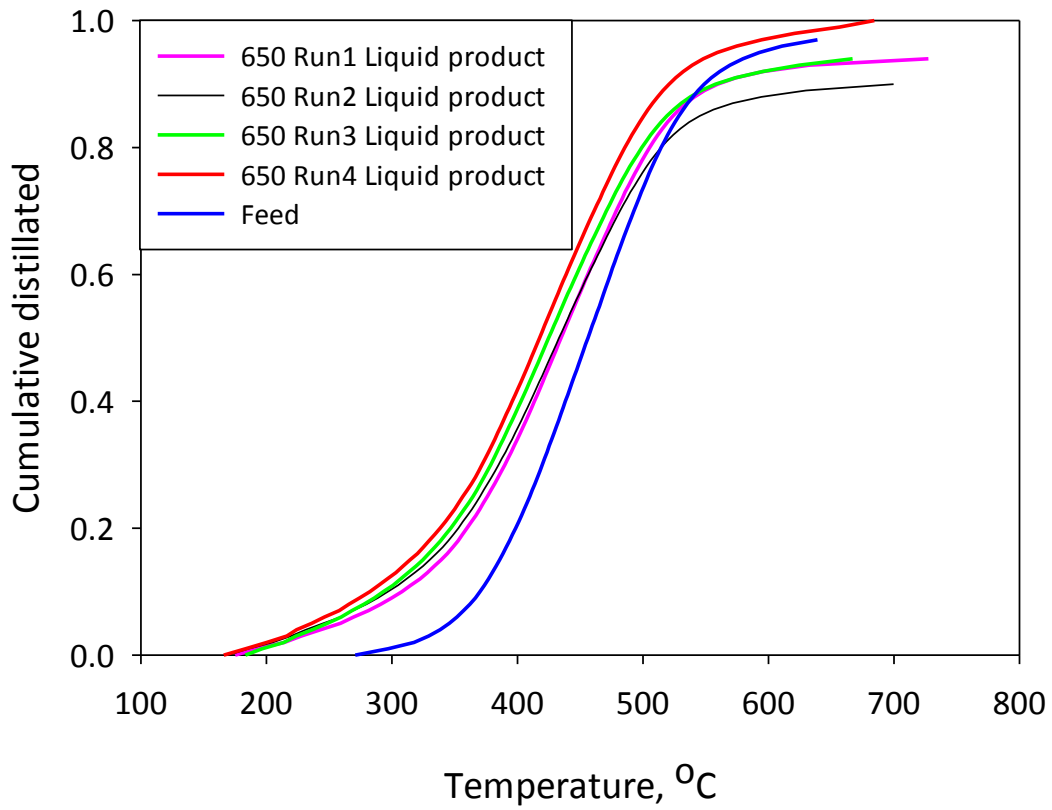


Figure C-5. Boiling curves for bitumen derived heavy gas oil feed and liquid products at 650 °C furnace set point by ASTM D 6352 method

ASTM D6352  
700 °C set point

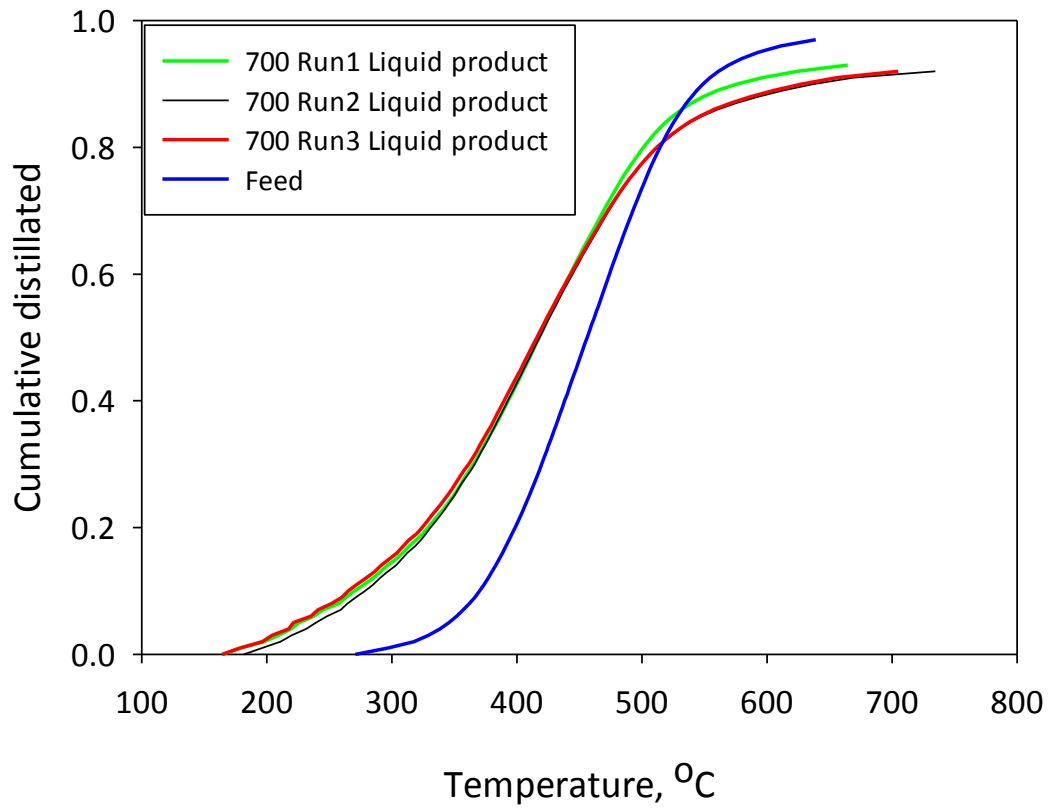


Figure C-6. Boiling curves for bitumen derived heavy gas oil feed and liquid products at 700 °C furnace set point by ASTM D 6352 method

# APPENDIX D

## MATLAB Code for the Kinetic Model

### 1. Residence Time

```
RT(1)=quad(@ft1,0.027,0.915); %600 Run1

function t=ft1(x) %600 Run1
    A=8.32807E-05; %cross sectional area of reactor tube, m2
    T0=24+273.15; %Room temperature
    v0=3.65444E-05; %volume flow rate of helium at room
    temperature
    T=T1(x);
    t=(A*T0)/(v0*T);

    function T=T1(x)
        Ts=881.93; %Reactor surface tepearture
        Tmi=313.15; %Helium initial temperature
        D=0.0103; %inner diameter
        h=85.05686688; %average heat coffecient
        m=6.00E-06; %mass flow rate of helium
        Cp=5193.686816; %heat capacity of helium
        T=Ts-(Ts-Tmi)*exp((-3.14*D*h*x)/(m*Cp));
    end
end
```

### 2. Mass Flow Rate of Reactive Species

```
[x,F]=ode45('Fx',[0.027,0.915],2.459816); %600 Run1
plot(x,F);
x,F

function dF=Fx(F,x) %600 Run1
    S=8.32807E-05; %cross sectional area of reactor tube, m2
    T0=24+273.15; %Room temperature
    v0=3.65444E-05; %volume flow rate of helium at room
    temperature
    R=8.314;
    A=2.471338E+12; %isothermal
    Ea=214744.503191; %isothermal
    T=Tx(x);
    dF=-A.*exp((-Ea/(R.*T))).*(F.*T0)/(v0.*T).*S;

    function T=Tx(x) %600 Run1
```

```

Ts=881.93; %Reactor surface temperature,K
Tmi=313.15; %Helium initial temperature,K
D=0.0103; %inner diameter
h=85.05686688; %average heat coefficient
m=6.00E-06; %mass flow rate of helium
Cp=5193.686816; %heat capacity of helium
T=Ts-(Ts-Tmi)*exp((-3.14*D*h*x)/(m*Cp));

```

```
end
```

```
end
```

### 3. Kinetic Parameters

```

x0=[2.471338E+12,214744.503191]; %Under isothermal assumption
options=optimset('Display','iter');
[x,f,exitflag,output]=fminsearch(@kinetics,x0,options) %fminsearch

[x,f,exitflag,output]=fminsearchbnd(@kinetics,x0,[10E4,30000],[10E
16,350000],options) %fminsearchbnd

```

```
function y=kinetics(x)
```

```
global X;
```

```
X=x(1);
```

```
global Y;
```

```
Y=x(2);
```

```

I=[2.459816;
2.197376;
2.161773;
2.063545;
2.321838;
2.029588;
2.042495;
2.242713;
2.532454;
2.284800];

```

```

C=[0.194185;
0.218827;
0.338080;
0.497024;
0.654925;
0.699412;
0.726681;
0.914483;
0.959043;
0.995848];

```

```

[L1,F1]=ode45(@kinetics1,[0.027,0.915],I(1));
F(1)=F1(41);
[L2,F2]=ode45(@kinetics2,[0.027,0.915],I(2));
F(2)=F2(41);
[L3,F3]=ode45(@kinetics3,[0.027,0.915],I(3));

```

```

F(3)=F3(41);
[L4,F4]=ode45(@kinetics4,[0.034,0.915],I(4));
F(4)=F4(41);
[L5,F5]=ode45(@kinetics5,[0.027,0.915],I(5));
F(5)=F5(41);
[L6,F6]=ode45(@kinetics6,[0.027,0.915],I(6));
F(6)=F6(41);
[L7,F7]=ode45(@kinetics7,[0.027,0.915],I(7));
F(7)=F7(41);
[L8,F8]=ode45(@kinetics8,[0.027,0.915],I(8));
F(8)=F8(41);
[L9,F9]=ode45(@kinetics9,[0.027,0.915],I(9));
F(9)=F9(41);
[L10,F10]=ode45(@kinetics10,[0.027,0.915],I(10));
F(10)=F10(41);

y=0;
for i=1:10
    y=y+((I(i)-F(i))/I(i)-C(i))^2;
end
end

function dF=kinetics1(F,L) %600 Run1
    S=8.32807E-05; %cross sectional area of reactor tube, m2
    T0=24+273.15; %Room temperature
    v0=3.65444E-05; %volume flow rate of helium at room
    temperature
    R=8.314;
    T=TL(L);

    global X;
    global Y;
    dF=-X.*exp((-Y/(R.*T))).*((F.*T0)/(v0.*T)).*S;

    function T=TL(L) %600 Run1
        Ts=881.93; %Reactor surface teperature,K
        Tmi=313.15; %Helium initial temperature,K
        D=0.0103; %inner diameter
        h=85.05686688; %average heat coffecient
        m=6.00E-06; %mass flow rate of helium
        Cp=5193.686816; %heat capacity of helium
        T=Ts-(Ts-Tmi)*exp((-3.14*D*h*L)/(m*Cp));

    end

end
end

```

# APPENDIX E

## Piping and Instrumentation Diagram

